NASA Technical Memorandum 106190

Experimental Study of Void Formation During Aluminum Solidification in Reduced Gravity

Francis Paul Chiaramonte III
Lewis Research Center
Cleveland, Ohio

October 1993

NASA

EXPERIMENTAL STUDY OF VOID FORMATION DURING ALUMINUM SOLIDIFICATION IN REDUCED GRAVITY

Francis Paul Chiaramonte III
National Aeronautics and Space Administration
Lewis Research Center
Cleveland, Ohio 44135

SUMMARY

Void formation due to volumetric shrinkage and liquid/vapor reorientation during aluminum solidification was observed in real time by using a radiographic viewing system in normal and reduced gravity. An end-chill directional solidification furnace with water quench was designed and constructed to solidify aluminum samples during the approximately 16 sec of reduced gravity (±0.02g) achieved by flying an aircraft through a parabolic trajectory. In the first series of tests the aluminum was contained in a vacuum-sealed, pyrolytic boron nitride crucible. An ullage space was present during each test. Void formation was recorded for two cases: a nonwetting system, and a wetting system where wetting occurred between the aluminum and the crucible lid. The void formation in the nonwetting case was similar in normal and reduced gravity, with a single vapor cavity forming at the top of the crucible. In the wetting case during reduced gravity surface tension caused two voids to form in the top corners of the crucible, but during normal gravity only one large void formed across the top.

In the second series of tests the aluminum was contained in a pyrolytic boron nitride crucible that was placed in a stainless steel container and sealed in an environment of argon plus 4 percent hydrogen. An ullage space was present during each test. Void formation was recorded for two cases: a nonwetting system, and a wetting system where wetting occurred between the aluminum and one side wall and the lid. The void formation in the nonwetting case was similar in normal and reduced gravity, with a single vapor cavity forming at the top of the crucible, although the meniscus became more convex in reduced gravity. In the wetting case the aluminum did not climb up the corners in 1g, and one large symmetric void resulted at the top when the aluminum had solidified. In the wetting case during reduced gravity the molten aluminum was drawn up the wetted wall and partially across the lid by a capillary underpressure; however, on the nonwetting wall the aluminum moved down. One void resulted along the nonwetting side of the container continuing to the top on the same side.

1.0 INTRODUCTION

1.1 Background

The general problem of void formation in reduced gravity has direct application to thermal energy storage for space power systems and to materials-processing operations, such as casting and crystal growth. Several planned space power systems require melting and solidification of a thermal energy storage material that undergoes a significant volume decrease when cooling from liquid to solid, which can cause voids to form. Specific examples of such phase-change materials (PCM) are lithium fluoride–20 percent calcium fluoride (LiF-20CaF_2), proposed for the solar dynamic power module of Space Station *Freedom* (ref. 1), and lithium (ref. 2), proposed for a space nuclear power system. LiF-20CaF_2 has a 20-percent volume decrease when solidified, and the liquid lithium volume will decrease by 25 percent when solidified. Also, from liquid/vapor studies in reduced gravity (refs. 3 and 4) the ullage in the molten state (which eventually becomes a void when the PCM solidifies) may be in a variety of locations. Specifically, reducing the buoyancy by diminishing the body forces will allow surface tension forces to be more influential in determining the void migration and final position. The effect of voids in the solidified PCM, particularly their uncontrolled or unknown locations due to reduced gravity effects, raises two major concerns. First, if voids form in the solidified PCM adjacent to a heat transfer surface, hot

spots may result on these surfaces (e.g., container walls) during the heat input portion of the cycle. Second, if voids are present in the solidified PCM at a location distant from the heat input area, undesirable container stresses may result because there are no neighboring voids for the melting PCM to expand into.

1.2 Review of Previous Work and Current Programs

1.2.1 Experimental work.—Several phase-change experiments were conducted in normal gravity (1g) as precursor studies of void formation in reduced gravity. Namkoong (ref. 5) tested three receiver tubes as part of the development of a full solar heat receiver that would serve as an energy source for a space power system. The receiver tubes were designed to provide a nearly constant thermal input to the power system while it is in low Earth orbit (LEO) by using the latent heat from a PCM, lithium fluoride (LiF) in this case. The excess solar energy acquired by the liquid LiF during the Sun period would be used during eclipse as the LiF solidified. The receiver design used coaxial tubes, with the outer tube being convoluted and containing the PCM as shown in figure 1. The convoluted tube design allowed the entire tube to be filled with LiF. Also, this tube design was expected to seal the LiF in each convolution at the onset of solidification, assuming that the PCM began to first solidify at the region of minimum clearance. Using three receiver tubes, tests were conducted in normal gravity to simulate LEO conditions, except gravity, by testing in a vacuum and using electric heaters that were axially distributed to simulate the solar heat flux. The receiver tubes were positioned 21½° off vertical. The receiver tubes were tested for 1251 cycles, with each cycle consisting of a 60-min simulated Sun period and a 36-min eclipse. After testing was completed, radiographs of the tubes revealed a nonuniform distribution of LiF in each tube, resulting in a high concentration of PCM in the lower convolutions and very little in the upper convolutions. Some distortion of the tubes was observed, but this had little effect on their performance. This scenario was assumed to be more severe than what would be expected in reduced gravity.

Kerslake (ref. 1) studied freeze-thaw characteristics of the salt LiF-20CaF_2 in an annular metal canister. This PCM was selected because it had been proposed for Space Station *Freedom* in the growth configuration. The sample was cycled hundreds of times in a LEO simulated mode by using an insulated test chamber, a quartz lamp array radiant heater, and cooling air. Each cycle lasted 91.1 min with 54.7 min of equivalent insolation period and 36.4 min of simulated eclipse period. Radiographs of the canister were taken before and after selected tests. The tests revealed that the 1g test orientation had a generally small effect on the canister wall temperature but that void position was strongly dependent on test orientation and canister cooling. Consequently, voids were located near the top of the canister volume.

A full receiver test was conducted by Boeing Aerospace (ref. 6) in which a nickel-felt metal matrix was inserted into heat storage tubes and then LiF-20CaF_2 was added. The felt would enhance the heat transfer because the thermal conductivity of the matrix was higher than that of the salt. It would also control the void distribution within the salt because its small pore radius would allow capillary forces to distribute the PCM within the felt. The receiver was cycled 58 times and each cycle lasted approximately 94 min, with 58 min of simulated Sun period and 36 min of eclipse. The receiver was insulated, heated with linear quartz lamps, and thermal vacuum tested with a cold wall to simulate a space environment. Testing revealed that both void distribution and the heat transfer through the PCM were improved. However, a small amount (5 percent) of the felt matrix became compacted, negating the desired heat transfer and void distribution improvements in that area. These tests demonstrate that the felt metal matrix is a viable concept; however, the long-term mechanical stability of the felt must be verified. This can be achieved by tens of thousands of cyclic temperature tests.

Sulfredge et al. (ref. 7) studied void formation by using two test materials, cyclohexane and butanediol, encapsulated in 1-cm-diameter Pyrex tubes. Cyclohexane has a volume change of 7.8 percent and butanediol has a volume change of 14.5 percent. The tubes were placed in a horizontal position for testing. Solidification was initiated from the tube wall and progressed radially inward. When a pure liquid (degassed) was used, the initial shrinkage

voids occurred in the upper half of the tube's cross section, resulting in the final distribution of voids to be found there. However, a nearly uniform distribution of voids resulted when tests were conducted using atmospheric air as a dissolved gas in the hydrocarbon test fluids. Reference 7 predicts that the voids will be axisymmetric in reduced gravity owing to thermocapillary forces. A similar solidification experiment (ref. 8) was conducted in a right-circular cylinder by using degassed cyclohexane with cooling from above in one case and from below in another. Cooling from below simply produced a void cavity at the top. Cooling from above produced randomly distributed elongated voids. Bubbles initially present at the top were pushed along the slowly moving solid/liquid interface until the bubbles ceased to move and became entrapped in the solid. Reference 8 predicts that zero-gravity behavior for this geometry will combine these two cases.

Takahashi et al. (ref. 9) conducted phase-change studies in 1g by using LiF in molybdenum cylindrical canisters. Mounted with the axial direction parallel to the gravity vector, the sample was heated radially from an electric heater and cooled by decreasing the heater input power. The molybdenum was wetted by the molten salt. X-ray computerized tomography photographs of both the axial and radial cross sections were taken after the sample was solidified. Both slow and rapid solidification tests were conducted. In the slow solidification test one large "V"-shaped void formed at the top, owing to meniscus shrinkage. At the higher solidification rate a number of uniformly distributed voids formed in the solid.

Tanaka et al. (ref. 10) have suggested two other designs to control void distribution. The first is encapsulation of the LiF within a porous silicon carbide (SiC) structure. The advantages are that the void distribution can be controlled and the heat transfer enhanced because SiC has a comparatively high thermal conductivity. The second concept uses a fin design made of carbon that does not wet the LiF. It is expected that melting will occur preferentially along the fins, creating channels from the liquid up into the void (or voids). This design should reduce the mechanical stress on the canister and enhance the heat transfer rate.

Several reduced-gravity experiments have investigated void formation during melting and solidification. A low-gravity solidification experiment was conducted by Papazain and Wilcox (ref. 11) in 1976 on a sounding rocket flight. The behavior of bubbles at a dendritic interface was observed by directionally solidifying carbon tetrabromide (CBr_4) saturated with argon, hydrogen, and nitrogen gases. These gases were rejected during solidification and formed bubbles at the growth interface. The transparency of the liquid phase allowed photographs of the freezing process, which revealed nucleation and growth of the bubbles. Bubbles trapped in the mushy zone were observed to coalesce abruptly. The dendritic growth front was able to go around the bubbles, thus forming a void. Bubbles situated in the melt well ahead of the interface did not migrate to the hot end of the sample tube; this is contrary to the predictions of thermal migration of bubbles in the absence of gravity. Also, the large bubbles near the top of the specimen tube were most likely generated by launch-induced fluid motion instead of the discontinuous change in the solubility of gas in the melt relative to that in the solid.

Klein et al. (ref. 12) conducted a freeze-thaw multiphase dispersion experiment in 1983 aboard the Space Shuttle on the STS–7 mission. Cesium chloride (CsCl), with lead (Pb) particles and air enclosures, was melted and directionally solidified at about 10^{-5}g. During melting and solidification, photographic recordings were taken of the optically transparent metal-like model system. Bubbles were formed partly by the gas originally dissolved in the sample, partly by the 10-percent volume decrease of the CsCl during freezing, and partly by the surplus volume provided between the windows and the solid specimen to prevent its thermal expansion from rupturing the windows. At the onset of solidification the Pb particles were uniformly distributed in the melt. During solidification, bubbles formed at the solidification front, grew, and were enclosed like channels in the crystal. As solidification continued and bubble size increased, interfacial convection at the bubble surface increased; however, no bubble transport induced by interfacial (Marangoni) convection was observed. The Pb particles moved in a clockwise flow direction in the liquid CsCl. This particle movement is interpreted as convective fluid flow due to residual gravity.

A reduced-gravity, phase-change experiment using LiF in a graphite cylindrical canister was conducted by Stähle and Lindner using a sounding rocket (ref. 13). The container design was unique because small rectangular channels were machined on the inside of the outer wall for the melting PCM to expand into, as shown in figure 2. Also, the graphite was not wetted by the LiF and therefore was not subject to corrosion. The canister was positioned so that the axial direction was parallel to the gravity vector. A furnace heated the sample to 890 °C (T_{mp} = 848 °C). Helium gas cooled the canister from the bottom. In both normal and microgravity the sample, initially liquid, solidified, remelted, and solidified again. After the test was completed, the samples were cut open for inspection. In 1g the melt penetrated the channels because of a 3-percent overfilling of the capsule but was drawn out of the channels during solidification by capillary pressure. A symmetric "V"-shaped void formed at the top of the canister. In microgravity one large ellipsoidal void formed that opened to one side of the capsule. It is assumed that uneven cooling caused the asymmetric void to form on the warmer side. The solid PCM was not found in the channels.

Three future Space Shuttle experiments are being built or planned to study void behavior for specific space systems. Proposed future solar dynamic power systems incorporate a relatively lightweight, high-efficiency receiver by using a thermal energy storage material that changes phase, such as LiF (ref. 2). A flight experiment entitled "Thermal Energy Storage (TES) Technology Experiment" is being built using LiF (a high-temperature, high-heat-of-fusion PCM that will undergo four freeze-thaw cycles in LEO (ref. 14)). LiF has a 29-percent volume reduction upon solidification, which causes voids to form. This space experiment will investigate the void behavior in LiF during melting and solidification in microgravity. The void positions will be determined through computerized tomography during postflight inspection. From the test data the void formation will be characterized and its effect on advanced heat receiver design performance predicted.

Future NASA and Department of Defense missions will require batteries capable of storing and delivering higher power at high rates. A Sodium-Sulfur Battery Flight Experiment has been proposed because these batteries offer two to three times the power of the presently used nickel-hydrogen batteries (ref. 2). The sodium-sulfur battery, operating between 300 and 400 °C, uses liquid sodium and sulfur polysulfide electrodes and a solid ceramic electrolyte. The electrode materials are transported to the surface of the electrolyte through wicking or capillary forces, which are well understood. However, the cell's ability to accommodate melting and solidification cycles in space may cause unique design considerations because sodium has a 5-percent volume decrease and sulfur has a 12-percent volume decrease upon solidification. The voids would be inspected during the postflight analysis.

Developing a space nuclear power system with a targeted output capacity of 100 kW is the goal of the SP–100 program. The power system would be particularly useful for missions beyond Earth orbit, such as establishing a lunar outpost and transporting humans to Mars. The generic flight system design has been completed by the contractor, General Electric (ref. 2). This proposed nuclear space power system uses lithium as its working fluid. Restart in space after the lithium becomes solidified is the major problem because lithium's volume will expand by 25 percent when melted. Difficulty arises in accommodating this expansion in a very complicated flow loop geometry while maintaining structural integrity. Dissolved helium gas has been proposed to create numerous small pores in the solid lithium. The pores would then accommodate the expanding lithium during melting.

1.2.2 Numerical work.—Analytical solutions of the solidification process with void formation have only been done for a few simplified one-dimensional cases. Furthermore, most computer models of the freeze-thaw process rely on making significant assumptions in order to investigate only a part of this phenomenon rather than modeling this system in three dimensions from first principles with all of the true boundary conditions. A useful but limited numerical simulation by Yang and El-Genk (ref. 15) configures the void as a single cell in a finite one-dimensional system. The void is positioned next to a wall with a given heat flux or next to an adiabatic boundary. Both LiF and Li are modeled as the PCM. The program solves the heat transfer equations with

two moving boundaries: the solid/liquid interface and the PCM/void interface. The problem is modeled as a one-dimensional slab filled with the PCM (initially at its melting point) in a container. One wall is radiatively cooled into space or radiatively heated from an isothermal heat source. The other side of the slab is insulated. The results of this numerical scheme are in reasonable agreement (less than 10-percent error) with an analytical solution for a PCM adjacent to a constant-temperature wall. The predicted results from this numerical simulation reveal that a void at the heat transfer wall reduces the solid/liquid interface velocity but that voids forming at the adiabatic wall do not influence the freeze-thaw process. Also, a void next to the heat transfer wall substantially raises the wall temperature during melting.

An application-specific numerical simulation code, NORVEX (NASA–Oak Ridge Void Experiment), is being developed to predict transient, solid-liquid, phase-change behavior with void formation and motion in a three-dimensional cylindrical geometry (ref. 2). Code development began at Oak Ridge National Laboratory (ORNL) for NASA Lewis Research Center, but this effort has been transferred to Lewis, where additional code development is in progress. The goal of this program is to model phase change, void formation and migration, and buoyancy and surface tension so that any gravity environment from 1g to 0g can be tested (ref. 16). Currently, the NORVEX program can accurately predict temperature and velocity distributions during phase change when no voids are present and the solid density is equal to the liquid density. As a first step toward modeling true void motion, the user must currently predetermine the initial void position. The fluid flow and related void motion, as well as an accurate energy and continuity balance, can then be computed. NORVEX presently cannot model void growth and motion in microgravity because buoyancy and surface tension equations have not yet been coupled with void movement. When successfully developed, the NORVEX code will be used to compare numerical predictions with microgravity data acquired from the TES experiment to be flown on the Space Shuttle in the mid-1990's. To the author's knowledge, this is the only computer code being developed to accurately predict phase-change behavior with void formation, subsequent migration, and fluid motion in reduced gravity.

1.3 Objective

The present experiment was conducted to experimentally investigate the phenomena of void formation, growth, and migration due to volumetric shrinkage and liquid/vapor reorientation of the ullage during solidification of aluminum under reduced-gravity conditions.

1.4 Plan of Investigation

Reduced gravity is achieved by flying an aircraft through a parabolic trajectory, which produces a gravity level of ±0.02g for approximately 16 sec. Aluminum was selected for this experiment because it has high thermal diffusivity and large volume change during solidification (7 percent) relative to other conductive materials. This experiment differed from Papazain's and also Klein's reduced-gravity work because no dissolved gas was present in the molten aluminum, thus avoiding the difficulty of distinguishing evolved gas from shrinkage-caused voids (ref. 17). This experiment differs from Stähle's reduced-gravity tests because the container in the present system was purposely wetted by the molten aluminum in order to observe ullage reorientation. Also, this experiment included real-time observation of the solidification process, a feature not provided for on experiments being built for near-term Space Shuttle missions.

2.0 ANALYSIS OF VOID FORMATION AND MIGRATION MECHANISMS

2.1 Voids from Liquid/Vapor Reorientation in Reduced Gravity

In the first void formation mechanism a bubble is generated in a liquid and then the liquid is solidified. In typical solar dynamic power system applications, even when the PCM is entirely liquid, a vapor volume usually exists. Because the PCM container is typically of a rigid shape, the vapor volume ensures that, should the liquid thermally expand, the container will not rupture. Because of this vapor volume the resulting free surface can change shape dramatically in a reduced-gravity environment. This shape change depends on the contact angle between the liquid and the container and on the container geometry. An experiment was conducted in reduced gravity to investigate how container geometry affects the shape of the free surface (section 3.3). The following discussion deals with the influence of the contact angle.

In any gravity environment the meniscus shape is stable under isothermal conditions when the potential energy is minimized (ref. 18), as shown in figure 3. From a macroscopic perspective a pressure discontinuity exists across the interface. This difference between the liquid pressure P_l and the gas pressure P_g is represented by the Young-Laplace equation

$$P_l - P_g = C\sigma \tag{1}$$

where C is the mean curvature of the liquid free surface and σ is the surface tension. Now the pressure in the liquid at the interface is proportional to the height h due to the hydrostatic pressure $\rho_l gh$, so that

$$P_l = P_{l,0} - \rho_l gh \tag{2}$$

where $P_{l,0}$ is the liquid pressure at the zero point in figure 3, ρ_l is the density of the liquid, and g is the gravitational constant. The liquid height is a function of the radial distance r:

$$h = h(r) \tag{3}$$

After combining equations (2) and (3), equation (1) becomes

$$P_{l,0} - \rho_l gh(r) - P_g = C\sigma \tag{4}$$

This reveals the influence of g on the free surface shape. In reduced gravity the hydrostatic pressure is significantly diminished and, neglecting this term, equation (4) becomes

$$P_{l,0} - P_g = C\sigma \tag{5}$$

resulting in

$$C = \frac{P_{l,0} - P_g}{\sigma} \tag{6}$$

Because $P_{l,0}$, P_g, and σ are constant, for isothermal conditions the mean curvature of the liquid C is also constant and maximum when g goes to zero. It is well known from experimental investigations of liquid/vapor interfaces in low gravity (ref. 3) that the contact angle of the liquid at the solid/liquid/vapor interface in normal gravity is preserved in low gravity. The liquid/vapor interface tends toward a configuration of constant surface curvature that intersects the container wall at the contact angle in reduced gravity. For example, the changes in interface shapes for a fluid at the 90-percent fill level in a cylinder at normal and reduced gravity are shown schematically in figure 4 for contact angles of $\theta_1 > 90°$ (nonwetting) and $\theta_2 < 90°$ (wetting) (ref. 3).

2.2 Voids From a Dissolved Gas or Shrinkage

In the second void formation mechanism bubbles are generated or material shrinks during solidification. Bubbles can be nucleated from several mechanisms; a few are cited here. In heterogeneous nucleation, bubbles will form because of impurities or crevices in the container wall. It is possible but less likely that pores will form without the influence of impurities or external surfaces. This is known as homogeneous nucleation and would require a very high pressure to initiate a small bubble (ref. 19). A favorable bubble nucleation site is the advancing solid/liquid interface when a dissolved gas is present. During solidification a dissolved gas is rejected into the liquid because of the difference in solubility. As the concentration of the gas builds up, so does its partial pressure, increasing the possibility of gas bubbles forming. When a bubble forms, the pressure of the gas inside the bubble equals the local hydrostatic pressure plus the pressure from surface forces (ref. 17):

$$P_g = P_0 + \rho_l g h + \frac{2\sigma_{g,l}}{r} \tag{7}$$

Bubble growth is influenced by the solidification rate (ref. 20). For a slow solidification rate the bubble may move with the interface, enlarge, and become trapped, retaining a spherical shape. For an intermediate solidification rate the bubble may become elongated before being trapped in the solid. For solidification at high growth rates the bubble may be rapidly overtaken by the interface, leaving small spherical bubbles dispersed through the solid.

Voids will also form when the solidifying material shrinks, assuming that the solid density ρ_s is greater than the liquid density ρ_l. Voids can form if solidification shrinkage is not fed by fluid flow (ref. 17) as in dendritic growth or the presence of an obstruction. Given continuity and $\rho_s > \rho_l$ there is a liquid velocity v_l toward the solid/liquid interface that is proportional to the rate of interfacial movement between the volumes of the two phases, as illustrated in figure 5 (ref. 21). If the fluid flow is not geometrically symmetric, a void will form.

2.3 Void Migration

Creating one large bubble in reduced gravity, as illustrated in figure 4(b), allows void migration to occur in several ways. The bubble will detach if the liquid momentum due to the downward liquid velocity v_l (fig. 5) is greater than the surface tension and residual buoyancy forces (ref. 22), assuming the bulk liquid is at the melting temperature. If detached, however, the bubble may migrate to a warmer region in the liquid (if a temperature gradient exists) because of thermocapillary flow (the Marangoni effect), assuming the surface tension σ decreases with an increase in temperature T, $d\sigma/dT < 0$. However, an opposing drag force will also be encountered. As solidification continues, the bubble may grow to accommodate the resulting smaller solid volume, assuming $\rho_s > \rho_l$.

3.0 MATERIAL SELECTION AND PRECURSOR EXPERIMENTS

3.1 Selection of a Test Material

Because the reduced-gravity time on the Learjet aircraft is limited to 16 sec, the test material was selected from the metal elements, since their thermal conductivity is typically higher than that of metallic salts or hydrocarbons. Several criteria were followed in selecting a metal. First, a melting point of 1500 K (1227 °C) or less was chosen so that typical resistive heating elements could be used in the experiment. Second, a liquid-to-solid volume reduction of 5 percent or more was selected for easy observation of voids. Third, a solidification distance $X(t)$ was chosen to be 4 cm or more in a time t of 16 sec. The quantity $X(t)$ was computed from the one-dimensional analytical solution provided here (ref. 23). As shown in figure 6, the liquid is initially at the melting point T_{mp} and solidification is caused by a step change in the wall temperature T_w. The step change used was 100 deg C in this case:

$$X(t) = 2\lambda(a_s t)^{1/2} \tag{8}$$

where

$$\lambda e^{\lambda^2} \operatorname{erf} \lambda = \frac{C_{p,s}(T_{mp} - T_w)}{L\pi^{1/2}} \tag{9}$$

Fourth, the element had to be safe to handle (i.e., nontoxic and nonhazardous).

Of the 64 metallic elements, 32 met the first criterion, 5 met the first and second criteria, 4 met the first, second, and third criteria, and only 2 met all four criteria. These two elements are aluminum and gold. Because molten aluminum forms a tenacious oxide layer on its surface when exposed to air, whereas gold does not, gold is the best choice. However, because of the enormous cost of gold, aluminum was chosen with the intention of solving the oxide film problem.

3.2 Wettability of Pyrolytic Boron Nitride by Aluminum Experiment

Because the change in the liquid/vapor interface in reduced gravity is potentially dramatic, an experiment was conducted to determine the contact angle between molten aluminum and the container material, pyrolytic boron nitride (PBN). Knowledge of this angle will assist in explaining the reduced-gravity behavior. The sessile drop technique was used to measure the equilibrium contact angle by allowing a drop of liquid aluminum to rest on a PBN substrate as shown in figure 7.

The purpose of this test was to determine the equilibrium contact angle between molten aluminum and pyrolytic boron nitride as a function of temperature in a vacuum of approximately 660 μPa (ref. 24). A literature search revealed that no equilibrium contact angle tests had been performed at the time of this experiment for the aluminum/PBN system (refs. 25 and 26).

3.2.1 Experimental procedure.—High-purity aluminum (99.9999 percent) was cut into small cylinders with a diameter of 3 mm and a height of 4 mm. The aluminum samples were cleaned in a beaker of acetone solution and placed in an ultrasonic cleaner for 30 min, washed in distilled water, pickled with a 10 percent sodium hydroxide solution for 120 min, etched in a 2 percent hydrofluoric acid solution for 5 min, and then washed in distilled water and ethanol. The aluminum samples were kept in an ethanol solution before testing.

Pyrolytic boron nitride, the substrate material, was produced by the supplier (Union Carbide of Cleveland, Ohio) using chemical vapor deposition. Each piece was disk shaped with dimensions of 1.9 cm in diameter and 0.09 cm thick. The PBN was cleaned in an acetone solution and placed in the ultrasonic cleaner for 15 min.

The sessile drop apparatus consisted of a vacuum chamber, a heater, and a video system shown schematically in figure 8. The stainless steel vacuum chamber operated at approximately 660 μPa and was evacuated by a mechanical pump and then by a turbomolecular pump. The heater was fabricated from an iron-chromium alloy heater wire, mounted on the inside of a quartz tube measuring 3.2 cm in diameter and 15.25 cm in length and surrounded by five molybdenum radiation shields. Two 200-W power supply units provided power to the heater. The temperature of the aluminum drop was measured by a Chromel-Alumel thermocouple (type k) placed in an alumina tube just beneath the substrate material. Titanium wire was inserted near the test specimen to act as an oxygen getter. The aluminum sample was placed on the PBN substrate material and positioned inside the heater tube. Light passed through two quartz windows and the open ends of the tube from a uniform light source lamp. The aluminum drop was filmed by a video camera with a microscope lens attachment. A computer with frame grabber and image analysis package was used to acquire a live digitized image and to measure the contact angle. The temperature was increased at an approximate rate of 15 deg C/min. Once the desired temperature was reached, the images of the drop were recorded at 5, 15, and 30 min and every 30 min thereafter for each experiment; the contact angles are plotted for these times in figure 9.

3.2.2 Results and discussion.—The time dependence of the contact angle at different temperatures is shown in figure 9. Each point of the curve represents an average of three experiments. The equilibrium contact angle for a specified temperature agreed within ±5°. The contact angle remained virtually unchanged with time for the 700 and 800 °C experiments and decreased slightly at 900 °C. A nonwetting condition existed for each of these three cases because the droplet surface was covered with an oxide film, which prevented an actual Al/PBN interface from occurring. Similar results were reported by John and Hausner (ref. 27) and Brennan and Pask (ref. 28) for the Al/Al_2O_3 system and by Laurent et al. (ref. 29) for the Al/SiC system.

The contact angle for experiments at 1000 °C changed rapidly between 5 and 60 min, changed gradually between 60 and 150 min, and then remained constant. The PBN was wetted by the molten aluminum at 1000 °C, implying that the effect of the oxide film had become insignificant and that subsequently a nonwetting-to-wetting transition had occurred (ref. 29). As shown in the digitized images of figure 10, the equilibrium contact angle decreased slightly with an increase in temperature up to 900 °C but decreased dramatically when wetting occurred at 1000 °C. These results are summarized in table I. During cooling after each run the contact angle did not increase but remained constant; this phenomenon has been reported by Brennan and Pask (ref. 28) for an aluminum/sapphire system.

TABLE I.—EQUILIBRIUM CONTACT ANGLE FOR Al/PBN SYSTEM AS FUNCTION OF TEMPERATURE IN VACUUM OF APPROXIMATELY 660 μPa

Temperature, °C	Equilibrium contact angle, deg
700	159
800	151
900	139
1000	49

3.2.3 Conclusions.—The wetting of pyrolytic boron nitride by molten aluminum was achieved at 1000 °C in a vacuum of 660 μPa; the contact angle stabilized at 49° within 2.5 hr. At or below 900 °C the equilibrium contact angle was greater than 90° and stabilized within 30 min in a similar vacuum environment. Since this experiment was completed (ref. 24), Xue et al. (refs. 25 and 26) have conducted a wettability experiment involving liquid aluminum on pyrolytic boron nitride under similar conditions. Results of the two experiments are similar but not the same. Similar to the results just presented, Xue et al. predict wetting, $\theta \leq 90°$, to occur at approximately 1000 °C; however, in their case the contact angle stabilized at about $\theta = 75°$ in 1 hr instead of at 49°. It is not until 1070 °C that Xue reports a contact angle $\theta = 50°$ (refs. 25 and 26). The larger contact angle reported by Xue may have occurred if a thicker oxide film remained on the aluminum sample thereby influencing the Al/PBN reaction. Xue used a vacuum pressure of 1100 μPa rather than the 660 μPa used in this experiment and cleaned the aluminum samples by using ultrasonic vibration in acetone for 20 min rather than the rigorous procedure used in this study. Both of these factors may have resulted in a thicker oxide layer on the molten aluminum.

3.3 Capillary Surfaces in Corners During Reduced-Gravity Experiment

The purpose of this experiment was to study liquid/vapor reorientation, during the change from normal to reduced gravity, due to the following two criteria: (1) a liquid penetrating a solid edge (wedge) and (2) the change in the Bond number starting from a 1g Bond number of $Bo \cong 1$. The results of this experiment were used to select the appropriate container geometry and Bond number for the aluminum solidification experiment.

It can be shown mathematically that a liquid will flow (wets) into a solid crevice under zero-gravity conditions if the sum of the contact angle θ and half the dihedral angle $\alpha/2$ of the edge is less than 90° (refs. 30 and 31) as illustrated in figure 11(a):

$$\theta + \frac{\alpha}{2} < 90° \tag{10}$$

If the fluid surface is concave (fig. 11(a)), a capillary underpressure exists in the liquid (the radii of curvature of the interface are on the higher pressure side (ref. 32)); this underpressure attempts to draw the fluid along the edge. This effect is further accelerated because the body force holding the liquid to the bottom is drastically diminished under reduced-gravity conditions, such as in drop tower tests. In the case of figure 11(b) a capillary overpressure exists in the liquid and the fluid will not flow in the corners (ref. 31).

Liquid/vapor reorientation depends not only on wetting of the corners but also on the Bond number

$$Bo = \frac{\rho_l g w^2}{\sigma} \tag{11}$$

which is a ratio of gravity to surface tension forces. The quantity ρ_l is the liquid density, g is the acceleration due to gravity, w is a characteristic length, and σ is the fluid surface tension. A large change in Bond number about the value $Bo = 1$ (i.e., $Bo >> 1$ to $Bo << 1$) can produce significant changes in the free-surface curvature. For example, an originally flat meniscus that is gravity dominated ($Bo >> 1$) can have a radius of constant curvature when surface tension dominated ($Bo << 1$) in reduced gravity (refs. 3 and 33).

3.3.1 Experimental procedure.—Acrylic plastic containers were cleaned in a beaker of ethanol, placed in an ultrasonic cleaner for 15 min, and rinsed with ethanol. Four different containers were fabricated with lids. Container 1 had a "bathtub" or rounded corner geometry (ref. 30) (where $\alpha \rightarrow \infty$) and a Bond number of 0.25 in 1g

as shown in figure 12(a). The other three containers (numbers 2, 3, and 4) had sharp 90° corners ($\alpha/2 = 45°$) and Bond numbers of 0.25, 4.0, and 1.0 in 1g as shown in figures 12(b), (c), and (d), respectively. Silicone oil (Dow Corning 200, 0.65 cSt) was injected with a syringe into each container at fill levels of 75 and 90 percent. The contact angle between the silicone oil and the container was $\theta = 0°$. Two containers were tested simultaneously in the experimental apparatus shown in figure 13 (ref. 33). The experimental hardware consisted of the Plexiglas containers, Styrofoam pads used for leveling, top and back lighting, and a motion picture camera. The camera recorded the free-surface shape at a rate of 128 frames per second. This experimental study was conducted in the NASA Lewis drop tower. In this facility the apparatus is allowed to free fall a distance of 27 m while enclosed in a protective drag shield. This drop tower provides 2.2 sec of reduced gravity at a level of 10^{-5}g (ref. 34).

3.3.2 Results and discussion.—The free surface for the rounded container varied only slightly from normal to reduced gravity as shown in figure 14. Because the Bond number was 0.25 in 1g, the capillary forces already dominated the body force; this produced only a minimal change in the liquid/vapor interface shape. The meniscus has a radius of constant curvature in reduced gravity. Also, because the vessel was rounded and did not have corners, the fluid would not be drawn farther up the container walls. This agreed with the work of Concus and Finn (ref. 30), who derived this through a rigorous mathematical proof.

For all three containers with sharp 90° corners the free surface went from a curved meniscus in 1g to a spherical or ellipsoidal bubble in reduced gravity at both fill levels. In reduced gravity the free surface required a longer time to establish its equilibrium configuration in the narrow rectangular container (fig. 12(b)) as compared with the square container (fig. 12(c)). This was due to a greater influence of the viscous drag force along the narrow container walls and was more noticeable at the lower fill levels. Figures 15 to 17 show the free surface for the three containers in normal and reduced gravity. In normal gravity, container 2 had a Bo = 0.25, container 3 had a Bo = 4.0, and container 4 had a Bo = 1.0. At the 90-percent fill level a free-floating bubble formed in each container in reduced gravity because liquid momentum pushed the bubble off the container lid. Because of the relatively low Bond numbers in normal gravity, the initial liquid/vapor interface approached a radius of constant curvature. Thus, the influence of Bond number in these cases was relatively small. However, because of a capillary underpressure the liquid penetrated up the corners in reduced gravity, since equation (10) applies.

3.3.3 Conclusions.—These tests have demonstrated that a liquid will flow into a corner in reduced gravity if the sum of the contact angle θ plus half of the dihedral angle $\alpha/2$ is less than 90° (refs. 30 and 31) for systems with a 1g Bond number of Bo $\cong$ 1. As the container cross-sectional area was decreased (i.e., from a square shown in fig. 12(c) to a rectangle shown in 12(b)), the time required for the interfacial surface to reorient in reduced gravity increased. This was due to a greater influence of the viscous drag force. In the case of the rounded or "bathtub" shaped container the free surface became a radius of constant curvature and did not flow along the container walls, as predicted by Concus and Finn (ref. 30). At the 90-percent fill level in the rectangular containers free-floating bubbles were observed in reduced gravity. This is a desirable initial condition for studying void formation during the present aluminum solidification experiment (ASE). These drop tower tests, using silicone oil in Plexiglas vessels, were used to model the ASE fluid-container system and have resulted in the design of two container shapes. First, the rounded container was selected for nonwetting studies, and second, a rectangular container with 90° corners was selected for the wetting studies. Because $\theta > 90°$ for the nonwetting experiments, the fluid will not flow along a solid edge, and thus a rounded container at a Bo = 0.25 is adequate. Because it is desirable to have the fastest reorientation possible and produce a bubble, a Bo = 4.0 was chosen for the wetting case.

4.0 EXPERIMENTAL HARDWARE, PROCEDURE, AND CONDITIONS

An end-chill directional solidification furnace with water quench has been developed and tested for solidifying aluminum samples during approximately 16 sec of reduced-gravity time (ref. 35). Solidification is recorded with a real-time x-ray unit and video system. The liquid/vapor interface can be seen on the recorded image, and the solid/liquid interface can be observed with the aid of image processing. A schematic of the apparatus is shown in figure 18(a), and a photograph of the experiment hardware is provided in figure 18(b).

The reduced-gravity experimental data were obtained on the NASA Lewis Learjet aircraft. The aircraft, with the experiment onboard, was flown through a parabolic (Keplerian) trajectory, which is a free-fall path as shown in figure 19. Reduced gravity is produced by following this trajectory as the aircraft's acceleration is kept to a minimum. Acceleration was measured on the aircraft in the x or longitudinal (back and forth) axis, the y or lateral (side to side) axis, and the z or pitch (up and down) axis by using three sensor heads. The output signals were recorded on a chart recorder as shown in figure 20. During each trajectory the acceleration range was maintained to within ±0.02 of normal gravity in all three directions for 15 to 20 sec (refs. 36 and 37).

4.1 Real-Time Radiographic Viewing System

The real-time radiographic viewing system includes the x-ray and image intensifier units, a high-resolution charge coupled device (CCD) camera, and a Super-VHS recorder, as illustrated in figure 21. The x-ray unit generates x rays by accelerating electrons from a filament onto an anode at up to 80 kV and 2 mA; the excitation of the anode by the electron beam generates the x-radiation (ref. 38). The focal spot size on the anode is 0.05 mm. In this study an x-ray intensity of 40 kV was used to penetrate the Al/PBN system, 60 kV for the Al/titanium diboride (TiB_2) system, and 80 kV for the Al/PBN/stainless steel system. Although the aluminum sample should be as close to the image intensifier as possible, thermal limitations resulted in placing the furnace about midway between the x-ray unit and the intensifier.

The image intensifier serves as a wavelength converter, accepting x rays and producing visible light. Within the image intensifier the x rays strike a photoelectric coated screen that emits electrons when struck by x-ray photons. The electrons are accelerated and focused by electrostatic lenses onto a second, smaller but brighter fluoroscopic screen. This screen's output light intensity is suitable for pickup by a video system (ref. 38). It is optically coupled to a high-performance video camera that converts the visible images to an electronic signal. The black-and-white CCD camera has horizontal and vertical resolutions of 570 and 485 lines, respectively. The video images are stored on the S–VHS recorder or viewed directly from the monitor. Knowing the crucible dimensions, the smallest recognizable void measured from a radiographic image is approximately 1 mm.

4.2 Furnace Quench System

The furnace quench system includes a three-zone furnace, a crucible, an aluminum sample, and a water quench. The furnace, shown in figure 22, uses nickel-chromium alloy resistive heating elements with a maximum power of 200 W per zone and is capable of heating samples to 725 °C. One thermocouple per zone is required for control purposes and to establish initial temperature conditions. Temperature data from a maximum of seven thermocouples can be recorded. In this experiment the temperature was recorded at four locations along the crucible wall by type k thermocouples. The thermocouples were positioned vertically at approximately 0.01, 1.0, 1.7, and 2.4 cm from the container bottom. Horizontally, each thermocouple was placed in the crucible wall about 0.25 cm from the aluminum-crucible boundary. Interchangeable crucibles having a volume as large as 2.5 × 2.5 × 2.5 cm for the samples were mounted in a fixed position. The samples were directionally solidified by spray quenching the crucible bottom with water. The quench time was 20 sec for the Al/PBN and Al/TiB_2

systems and 60 sec for the Al/PBN/stainless steel system. The water was collected in a reservoir tank and pumped back to the crucible at a flow rate of 10 liters/min. The typical solidification rates of an aluminum sample were approximately 0.13 cm/sec using a PBN crucible and 0.03 cm/sec using the double-walled PBN and stainless steel container.

4.3 Furnace Control System

The computer, the data acquisition and control system (DACS), and the power control unit (PCU) are used to retrieve temperature data and to provide regulated power to the furnace. A block diagram is given in figure 23. The crucible temperatures are computer controlled by regulating the current from the aircraft 28-V-dc power supply to each of the heaters by means of voltage-to-current dc amplifiers in the PCU. The thermocouple millivolt output signals are acquired by the data acquisition unit and stored as temperatures in the computer. The voltage values from the amplifier outputs are determined by the DACS and sent to the computer through the IEEE–488 interface bus. These temperature and voltage values are used to determine the required input power for the furnace and are stored once per minute while heating the furnace and about once per 0.6 sec during the quench. The control software calculates and sends an updated voltage signal to the amplifiers in the PCU. The amplifiers, which are directly connected to the appropriate heating coil, adjust their outputs in proportion to this input signal. The entire system forms a feedback loop allowing control of the furnace temperature. At the appropriate time the quench is initiated by closing a relay that energizes the pump. This relay is controlled by the computer through an actuator in the data acquisition unit.

4.4 Control Software

The computer software will control the temperature at two or three points in the furnace as a function of time. A flow chart of the control program is provided in figure 24. After the program has initialized several variables (e.g., time t, resistance R, and maximum voltage V_{max}), the operator is prompted for certain parameters: ramp-up rate $\Delta T/\Delta t$, soak temperature T_{sk}, soak time t_{sk}, and temperature gradient $\Delta T/\Delta x$. The program then advances through four stages. The temperatures will first be ramped up at a constant heat-up rate (ramp stage) to a prescribed soak temperature. When the soak temperature is reached, it will be held constant for a prescribed time (soak stage). After the soak time has elapsed, the program will enter the ready stage. In both the soak and ready stages a proportional-plus-integral control law is used to calculate the required heater power for each of the furnace heaters to bring the control thermocouples to their specified temperature values. During the ready stage a keyboard input will initiate the fourth and final stage (quench). The quench stage is started as the aircraft flies a parabolic trajectory producing about 16 sec of reduced-gravity time. During the first three stages time, temperature, and power data are stored once per minute; during the quench stage data are stored about once per 0.6 sec. This complete experiment sequence can be repeated three times. At any time the operator can abort the run.

4.5 Sample Preparation

Several 99.9999-percent-pure aluminum samples were cleaned in a beaker of acetone solution and placed in an ultrasonic cleaner for 10 min, washed in distilled water, pickled in 10 percent sodium hydroxide solution for 120 min, and then washed in distilled water and ethanol (ref. 24).

4.5.1 Pyrolytic boron nitride crucible preparation.—The typical aluminum sample size was 2.4 × 2.4 × 0.6 cm (height times width times thickness). The PBN crucibles had rounded corners (bathtub shape), as shown in figure 25 and discussed in section 3.3. The crucibles were cleaned in a beaker of acetone solution and placed in

the ultrasonic cleaner for 15 min. The samples were vacuum sealed in the crucibles by using a silver-based vacuum braze material (68.8% Ag, 26.7% Cu, 4.5% Ti). The vacuum chamber pressure was approximately 660 μPa and the braze temperature was 885 °C (ref. 39). This Al/PBN system was placed in the crucible holder for testing as shown in figure 26.

4.5.2 Titanium diboride crucible preparation.—Typical aluminum sample size was 2.4 × 2.4 × 0.6 cm (height times width times thickness). The titanium diboride (TiB_2) crucible also had rounded corners (bathtub cross section), as shown in figure 27 and discussed in section 3.3. The crucibles were cleaned in a beaker of acetone solution and placed in the ultrasonic cleaner for 15 min. The sample was vacuum sealed in a TiB_2 crucible by using a gold-based vacuum braze material (50% Au, 25% Ni, 25% Pd). The vacuum chamber pressure was approximately 660 μPa and the braze temperature was 1132 °C (ref. 39). An assembly drawing of the Al/TiB_2 system is shown in figure 28.

4.5.3 Stainless steel container preparation.—The typical aluminum sample size was 1.5 × 2.4 × 2.4 cm (height times width times thickness). This sample was shorter than those used in the PBN or TiB_2 containers because of the longer quench time required. The sample was thicker to increase the Bond number, which should cause the change in the liquid/vapor interface shape from 1g to ±0.02g to be more dramatic. All crucibles were cleaned in a beaker of acetone solution and placed in the ultrasonic cleaner for 15 min. The sample was placed in the inner rectangular PBN crucible shown in figure 29(a). The inner crucible was then inverted and placed into the outer PBN crucible shown in figure 29(b). The PBN lid, shown in figure 29(c), was placed on top. This Al/PBN system was inserted into the rectangular stainless steel container shown in figure 30. A PBN leaf spring was used to exert a force on the PBN lid and to keep the PBN crucible in contact with the bottom of the stainless steel container. An assembly drawing is shown in figure 31. This system was welded shut and then the stainless steel tube was connected to a vacuum pump (providing 660 μPa) and furnace as shown in figure 32. The stainless steel container was placed upside down in the furnace and heated to 1050 °C for 3 hr to allow the upper portion of the PBN container to be wetted by the aluminum (refs. 24 to 26). In order to minimize the oxide layer that forms on the aluminum surface, the container was backfilled six times with Ar-4H_2. Hydrogen will join with O_2 to form H_2O, which is then removed by the vacuum system. The Ar-4H_2 environment was preserved in the container by sealing off the tube through spot welding.

4.6 Experimental Sequence in Reduced Gravity

The aluminum crucible system is heated uniformly in the computer-controlled furnace to 670 °C. The typical heat-up rate is 12 deg C/min. The sample is held at 670 °C for several minutes to ensure that the aluminum has melted and thermal equilibrium has been reached. During the parabolic trajectory spray quenching is initiated by keyboard input and the real-time x-ray system is activated by depressing a "deadman" switch. This test sequence has been programmed to repeat three times in one flight. A detailed experimental checklist procedure used for each flight is given in appendix A.

4.7 Image Processing

Because the solid/liquid interface could only be observed in some of the recorded images during playback of the aluminum solidification, image processing was used to track the solid/liquid interface distance versus time. Figure 33 shows the typical transient progression of the solid/liquid interface in the aluminum/PBN system. This interfacial movement was essentially independent of the experimental gravity level. Determining the solid/liquid interface required a computer with a frame grabber and an image analysis package. The procedure is as follows: (1) Acquire two live digitized images of a test run, one when the sample is entirely liquid prior to quench, the other when the sample is part liquid and part solid; (2) apply a low-pass filter to each image to remove

high-frequency noise; (3) subtract the "all liquid" image from the "part liquid–part solid" image; and (4) stretch the gray scale to magnify the contrast between the light and dark areas. The dark region is solid and the light gray region is liquid. The dark vertical line on the left side of figures 33(a) to (c) is assumed to be due to a shift in the two images that are subtracted from each other and is not considered as part of the solid/liquid interface.

4.8 Effect of Bond Number

As discussed in section 3.3, the Bond number was considered in this experiment. The Bond number, given in equation (11), is a ratio of gravity to surface tension forces. The characteristic length w of the PBN and TiB_2 crucibles was 0.3 cm, one-half of the crucible width. The relatively narrow crucible was selected in order to freeze the aluminum in approximately 16 sec. However, this resulted in a Bond number of 0.25 in normal gravity, which should produce little or no change in the liquid/vapor interface shape in reduced gravity. In an attempt to observe the change of the free surface from normal to reduced gravity, the stainless steel containers were built to provide a Bond number of 4.0. Although this is still relatively small, heater power and furnace design prevented a larger container from being tested.

4.9 Test Matrix

The test parameters are summarized in table II. All aluminum samples were heated to 670 °C prior to quenching.

TABLE II.—TEST MATRIX

Test point	Container material	Cell size,[a] cm	Liquid fill level, percent	Quench time, sec	Container wetted by aluminum
1	PBN	2.5×2.5×0.6	70	20	None
2	PBN	2.5×2.5×0.6	95	20	Partial
3	TiB_2	2.5×2.5×0.6	50	20	Complete
4	PBN/SS	1.9×2.5×2.5	66	60	Partial
5	PBN/SS	1.9×2.5×2.5	66	60	None

[a]Height times width times thickness.

5.0 RESULTS AND DISCUSSION

5.1 Pyrolytic Boron Nitride Crucibles

For the Al/PBN system the curved solid/liquid interface illustrated in figure 33 indicates that a horizontal temperature gradient was present in the aluminum during the solidification process. This gradient causes natural convective flow in the melt (ref. 40).

The curved solid/liquid interface is a net result of several factors, some of which are cited here. A relatively large amount of latent heat is released during solidification as indicated by a small Stefan number, Ste = 0.027, where the Stefan number for the melt is defined as

$$\text{Ste} = \frac{\text{Sensible heat of liquid}}{\text{Latent heat of fusion}} = \frac{C_{p,l}(T_l - T_{mp})}{L} \tag{12}$$

The large amount of latent heat being rapidly released decreases the liquid vertical temperature gradient and increases the horizontal temperature gradient, thereby increasing the concave curvature of the solid/liquid interface with respect to the melt (ref. 41). The horizontal gradient was also evident from the crucible wall thermocouple data. The temperature was recorded at four vertical positions along the crucible wall by using thermocouples; these results are shown in figure 34. Each thermocouple was 0.23 cm from the Al/PBN boundary. The solid/liquid interface distance as a function of time was determined from figure 33 and is indicated by the triangles in figure 34. As the advancing solid/liquid interface passed each thermocouple, the wall temperature at this point was approximately 575 °C. Because the solid/liquid interface was at 660 °C, a horizontal temperature gradient existed. Because k_s (217 J/sec-m-K) and k_l (94 J/sec-m-K) are much greater than k_w (3 J/sec-m-K), the interface curvature would be expected to be minimal (ref. 42). However, because k_s is greater than k_l, the solid/liquid interface has a tendency to turn down at the wall, concave with respect to the solid (ref. 43).

The horizontal temperature gradient produces natural convective flow in the melt. On the basis of a characteristic length of 1.27 cm (the horizontal half-length) and a horizontal temperature gradient of 10 deg C (the bulk temperature of 670 °C minus the melting point of 660 °C), the Rayleigh number is Ra = 1088 under normal gravity and Ra = 22 under 0.02g. The Rayleigh number is defined as

$$\mathrm{Ra} = \frac{\text{Buoyancy force}}{\text{Change of momentum flux}} = \frac{g\beta\,\Delta T\,w^3}{va} \tag{13}$$

A numerical simulation performed by Arnold et al. (ref. 42) for gallium arsenide in a gradient freeze furnace showed that the isotherms varied only slightly from those dominated by conduction at Ra = 164. This suggests that natural convective flow was occurring in the present experiment.

In addition to natural convective flow surface-tension-driven convection must be investigated because a liquid temperature gradient exists and a free surface is present. Because surface tension σ decreases with increasing temperature, a temperature gradient at the free surface will cause an imbalance of surface tension forces. This drives the warmer fluid, a region of low surface tension, toward the colder fluid, a region of high surface tension. The Marangoni number quantifies this phenomenon and is defined as

$$\mathrm{Ma} = -\left(\frac{\partial\sigma}{\partial T}\right)\frac{\Delta T\,w}{\mu a} \tag{14}$$

Surface-tension-driven flow is induced at a Marangoni number Ma $\geq$ 0 if the temperature gradient is parallel to the free surface (thermocapillary convection) and at Ma $\geq$ 70 if the temperature gradient is perpendicular to the free surface (Benard-Marangoni instability; ref. 44).

In order to compute the Marangoni number for the Al/PBN system shown in figure 33, a horizontal temperature gradient of 10 deg C was chosen because the bulk fluid temperature is 670 °C. The characteristic length w was 1.27 cm, the half-width of the container. The Marangoni number was Ma = 876 for the thermocapillary flow case. In the case where the temperature gradient was perpendicular to the free surface, the vertical temperature gradient was also estimated to be 10 deg C, using the same rationale, and the characteristic length was chosen to be 1.2 cm; this represents an average vertical liquid height during solidification. The Marangoni number was Ma = 827 for the Benard-Marangoni instability condition. Both cases indicate that surface-tension-driven convection occurred in the molten aluminum during solidification.

The dynamic Bond number provides a comparison of the buoyancy forces with the surface tension gradients and is defined as (ref. 44)

$$Bo_{dyn} = \frac{\rho\beta g h^2}{\partial\sigma/\partial T} \tag{15}$$

For $Bo_{dyn} < 1$ surface-tension-driven convection dominates over natural convection, and for Bo > 1 the reverse is true. For the Al/PBN system shown in figure 33 the dynamic Bond numbers were $Bo_{dyn} = 1.11$ in normal gravity (1g) and $Bo_{dyn} = 0.22$ in reduced gravity (±0.02g). Natural convection and surface-tension-driven convection were of similar magnitude in normal gravity, but surface-tension-driven convection dominated in reduced gravity for this Al/PBN system.

Because there is a 7-percent density change from liquid to solid aluminum, where $\rho_s > \rho_l$, a liquid velocity will exist and move toward the solidification front. This fluid velocity due to phase change is given as (ref. 21)

$$v_l = \left(\frac{\rho_s}{\rho_l} - 1\right)\frac{dx}{dt} \tag{16}$$

and is illustrated in figure 5. For the Al/PBN system shown in figure 33 this phase-change velocity was approximately $v_l = 0.01$ cm/sec and was not gravity dependent. (Aluminum properties used in these calculations are given in appendix B).

The effect of the fluid motion from these three mechanisms, however, was not influential for the following two reasons: First, the rapid average solidification rate of 0.13 cm/sec showed no variation with gravitational conditions. Second, there were no dissolved gases to generate bubbles, which could become caught in the flow cells; rather the voids originated at the ullage space and did not detach as free-floating bubbles.

From figure 33 the solid/liquid interface distance was measured at the four time intervals and is provided in table III. The solidification rate for this test case was, for the most part, parabolic as a function of time as described in equation (8) and plotted in figure 35. However, because of the interface resistance between the PBN and the aluminum, solidification progressed at a linear rate with time for the first 3 or 4 sec. As the resistance of the advancing solid aluminum began to dominate the interface resistance, the solidification rate $X(t)$ became proportional to the square root of the time. This result is quite typical (ref. 17).

TABLE III.—DIRECTIONAL SOLIDIFICATION DISTANCE OF PURE ALUMINUM IN A PBN CONTAINER VERSUS TIME

Time, sec	Square root of time, $sec^{1/2}$	Solidification distance	
		in.	cm
4	2.0	0.2	0.5
8	2.8	.4	1.0
11	3.3	.6	1.5
14	3.7	.7	1.8

The Al/PBN system, illustrated in figure 26, was tested and these results are shown in figures 36 and 37. Figure 36 shows the aluminum at the 70-percent liquid fill level in the molten state before spray quenching and just after solidification for reduced- and normal-gravity conditions. This Al/PBN system is nonwetting (refs. 24 to 26). Because the Bond number was 0.25 in normal gravity, a similar convex liquid/vapor interface occurred for both gravity conditions as shown in figures 36(a) and (c). In normal and reduced gravity the shrinkage-

caused void was accommodated by the enlarged vapor volume, as shown in figures 36(b) and (d), and there was no real difference in the final void shape or location. This test was conducted twice in reduced gravity with the same result.

Figure 37 shows the aluminum at the 95-percent liquid fill level. In this Al/PBN system wetting occurred between the aluminum and the crucible lid. The liquid/vapor interface was curved at both gravity levels, as shown in figures 37(a) and (c), which is consistent with the Bond number predictions. Prior to quenching, the molten aluminum was in contact with the crucible lid at both gravity conditions. During solidification in reduced gravity the aluminum remained attached to the top surface as shown in figure 37(d). In normal gravity the aluminum remained attached to the top surface until the solid/liquid interface had advanced to about the middle of the crucible. The aluminum then pulled away, resulting in the image shown in figure 37(b). This particular Al/PBN system was intended to be nonwetting; however, it is assumed that there was some unintentional wetting of the PBN by aluminum on the underside of the lid. This may have occurred during the 885 °C vacuum preparation of this Al/PBN crucible system. However, it is not clear why wetting occurred as the Al/PBN system requires about 1000 °C in a vacuum for wetting to take place (refs. 24 to 26). Another possibility is that some of the braze alloy may have reached the inside of the container, providing a material to which the aluminum may have bonded. The results from this test indicate that surface tension forces caused the aluminum to adhere to the crucible lid, creating two voids in reduced gravity, whereas a single large void cavity formed near the lid in normal gravity. In the reduced-gravity test the ullage volume in the corners enlarged as the sample was solidified. The sample contracted as it solidified, but the aluminum adhered to the lid, resulting in two voids forming instead of one. This test was only conducted once in reduced gravity.

5.2 Titanium Diboride Crucible

One reduced-gravity test was conducted in a rounded TiB_2 crucible. This container, shown in figures 27 and 28, had a Bo = 0.25 in normal gravity and the same cross-sectional shape (bathtub), as the PBN crucibles. This crucible contained 50 percent molten aluminum in a vacuum environment. Because a brazing temperature of 1132 °C was required for the sealing process (ref. 39), the TiB_2 was wetted by the aluminum. A wetting test conducted by Rhee (ref. 45) revealed that the contact angle between molten aluminum and TiB_2 is $\theta = 37°$ at 900 °C and that θ decreases with increasing temperature.

In normal gravity the free surface shape was concave with a radius of constant curvature; this is consistent with Bond number predictions. The results in reduced gravity indicate that a bubble had forced its way into the molten aluminum from the crucible bottom just after quenching was initiated. The quench lasted 20 sec. A spherical vapor space remained in the center of the Al/TiB_2 system when solidification was completed. After the flight, cracks in the TiB_2 crucible bottom were clearly evident and probably allowed air to rush into the container. This crucible did not withstand the thermal shock from approximately 700 °C to 100 °C during quenching despite numerous preliminary tests. In these preliminary tests TiB_2 samples measuring 2.5 × 2.5 × 0.076 cm (length times width times thickness) having the same thickness as the crucible bottom, did not crack until they were plunged in water from an initial temperature of 1000 °C. Although the same thickness was used on the crucible bottom, the machined piece was "U" shaped as shown in figure 27(c), section A–A. The cracking may be due to a higher stress concentration in the curved region, which had a 0.05-cm (0.02-in.) radius.

5.3 Stainless Steel Container

The stainless steel container system, illustrated in figure 31, was built because it could be welded shut and maintain the desired Ar-4H_2 environment even after several thermal cycles. On the contrary, the brazing alloy (ref. 39) used to seal the Al/PBN system discussed in section 5.1 would eventually leak because of a mismatch

in the coefficients of thermal expansion between the brazing alloy and the PBN. Once a leak occurred, the oxygen in the air resulted in the formation of an oxide layer (Al_2O_3) on the molten aluminum. This layer caused the free surface to become rigid, rendering future tests useless. In the stainless steel containers the Ar-4H_2 environment minimized the oxide buildup because the H_2 joined with the O_2 to form water vapor.

After being carefully prepared and sealed as described in section 4.5.3, the aluminum was melted and solidified in normal gravity as shown in figures 38(a) and (b), respectively. Figure 38(a) shows that the inner PBN crucible was wetted by the molten aluminum because the contact angle was less than 90°. This desired result from the sealing process agrees with prior work conducted in 1g as shown in figure 4(b) (ref. 3) and with the results from section 3.3 in which silicone oil in a Plexiglas container was used (fig. 16(a)). In figure 38(a) the dark gray region indicates the position of the molten aluminum. The light gray region is assumed to be molten aluminum that is in the corners of the rectangular container. The white region is a void. The fill level was about 66 percent of the container. After the aluminum solidified, its volume had decreased because $\rho_s > \rho_l$; this can be observed in figure 38(b). One void was positioned symmetrically at the top of the PBN crucible. The time required to solidify the aluminum by using the water spray quench system was approximately 60 sec. Several factors were involved: Heat had to be extracted through two containers (PBN and stainless steel) instead of one, and this system had a larger mass than the Al/PBN system, requiring more time to cool (larger time constant). Consequently, reduced-gravity tests were conducted approximately 20 sec after the quench was initiated to capture the solidification in progress.

Figure 39 shows a time-elapsed sequence of the experiment with the same aluminum sample on the aircraft during a parabolic trajectory. Figure 39(a) shows the condition of the aluminum during the 2½g pullup 12 sec after the quench had started. Figures 39(b) and (c) reveal the sample during reduced gravity 17 sec and 34 sec, respectively, after the quench had started. Figure 39(d) shows the solidified aluminum sample during the 2g pullup at the end of the trajectory, 58 sec after the quench had started. Figure 39(a) reveals an asymmetrical liquid/vapor interface because the left wall was wetted by the aluminum and the right wall was not. Apparently between the 1g test conducted on Dec. 21, 1992, and the reduced-gravity tests conducted on Jan. 19, 1993, the wetting characteristics on the right side changed. It is possible that the molten aluminum reacted with the stainless steel outer container, producing an Al-Fe alloy. Montgomery (ref. 46) observed that a molten Al-Fe alloy wet and spread slightly on PBN; however, the PBN fractured upon cooling. This may have occurred in the present experiment.

As the sample transitioned from 2½g (fig. 39(a)) to ±0.02g (fig. 39(b)), the capillary underpressure in the liquid (ref. 31) drew the molten aluminum up the corner and across the top of the PBN crucible on the wetted side. This result was experimentally predicted from the reduced-gravity drop tower tests of silicone oil in Plexiglas containers (section 3.3) for a completely wetting scenario and is shown in figures 16(b) and (d).

As the fluid rose on the wetted side, it was pulled downward on the nonwetted side, and the liquid/vapor interface became somewhat "S" shaped. This result combined wetting and nonwetting systems and can be conceptualized from previous results by combining the left half of the reduced-gravity drawing in figure 4(b) with the right half of the reduced-gravity drawing in figure 4(a). As shown in figure 39(c) the fluid attached to the lid began to "neck down" as solidification drew more of the molten aluminum toward the bottom. This liquid velocity, illustrated in figure 5, accommodated the reduced volume of the solidified aluminum. Although the aluminum was not totally solid, the final reduced-gravity void location can be approximated by figure 39(c). The void position, indicated by the white and light gray areas, was at the top and right side owing to the asymmetric wetting conditions. Figure 39(d) shows the sample during the 2g pullup at the end of the trajectory. Most of the fluid in the upper left-hand corner had not solidified and was drawn downward. The curvature of the aluminum on the right side, however, retained its reduced-gravity form because it had solidified in reduced gravity. This test was conducted twice in reduced gravity and yielded the same result.

A similar asymmetric liquid/vapor interface shape was observed in reduced gravity by Weislogel (refs. 33 and 47) as shown in figure 40. In this experiment 5-cSt silicone oil was tested in a cube-shaped Plexiglas container. The left side of the container had a 0° contact angle with the oil, and the right side had a fluorocarbon barrier coating (FC 723), resulting in a 59° contact angle. The sample was tested in the NASA Lewis 2.2-sec drop tower (ref. 34). Figure 40(a) shows the fluid with a flat meniscus while in 1g. The meniscus of the oil was much flatter than that of the molten aluminum because its Bond number in 1g was 300 versus 4 in the aluminum solidification experiment. Figure 40(b) shows the fluid reorientation after 2 sec at 10^{-5}g. The fluid was drawn up the corner and across the lid on the left side but was drawn up only slightly on the right side. Comparing this orientation with figure 39(b) or (c) shows that a similar result was obtained. Because the contact angle on the right side was greater than 90° in the aluminum case, the liquid/vapor interface turned down on this side.

As the same stainless steel container was tested further, the Al/PBN system became nonwetting on all the side walls (i.e., $\theta > 90°$). Parabolic trajectories were conducted under these conditions, and the results are shown in the four time-elapsed images of figure 41. Figure 41(a) shows the molten aluminum during the 2½g pullup 4 sec after the quench had started. Figures 41(b) and (c) show the sample during reduced gravity 20 and 29 sec, respectively, after the quench had started. Figure 41(d) shows the solidified aluminum sample and is 58 sec after the quench had started. The dark gray region in figure 41 reveals the bulk of the aluminum. As the sample went from 2½g (fig. 41(a)) to ±0.02g (figs. 41(b) and (c)), the flattened meniscus tended toward a configuration of constant surface curvature intersecting the container wall at the contact angle. Earlier work (ref. 3) confirms this result and is shown schematically in figure 4(a). In this case a capillary overpressure exists, indicated by the convex meniscus shape, and the molten aluminum would not flow in the corners (ref. 31) while in reduced gravity. In figure 41(d) the aluminum had solidified and the solid/vapor interface remained partially curved; this implies that the sample was almost completely solidified while in reduced gravity.

The fill level of the aluminum changed considerably from figures 41(a) to (b). Two factors are cited here. First, 16 sec elapsed between these figures so that some solidification had occurred, causing the volume of the aluminum to decrease. Second, although the bulk of the molten aluminum did not wet the PBN, some of the aluminum did as indicated by the light gray region. In figure 41(b) the light gray region in the upper half of the container became slightly darker. This implies that some of the molten aluminum was drawn up along the corners of the side wall from the darker bulk fluid below while in reduced gravity. Returning to the 2g condition shown in figure 41(d), the light gray region in the upper half of the container became lighter again. This implies that some of the fluid had fallen down at this gravity level. This nonwetting test was conducted twice in reduced gravity: first without quenching and then with quenching. The same meniscus shape was observed in both tests, as shown in figure 41(b).

5.4 Real-Time Radiographic System Performance

The voids were clearly recognizable because the real-time radiographic viewing system provided a clear image of the liquid/vapor interface and, with the aid of image processing, the solid/liquid interface. Because large voids are of primary interest for space power systems, no posttest examinations were made of the samples. The present resolution of 1 mm is considered adequate. Furnace temperatures of 700 °C limited the proximity of the heated sample to the image intensifier. The sharpness and resolution of the radiographic images could be improved by cooling the intensifier, thus allowing the furnace and sample to be mounted closer to it. To the author's knowledge, this was the first use of a real-time radiographic viewing system to observe void formation during solidification in reduced gravity.

6.0 CONCLUSIONS AND RECOMMENDATIONS FOR FURTHER RESEARCH

6.1 Conclusions

Directional solidification of pure molten aluminum in a sealed pyrolytic boron nitride container has been observed in both normal and reduced gravity by using a real-time radiographic viewing system. Reduced gravity was achieved by flying a Learjet aircraft through a parabolic trajectory. The reduced gravity level, ±0.02g, lasted approximately 16 sec. The typical aluminum solidification rate was 0.13 cm/sec for the aluminum/pyrolytic boron nitride (Al/PBN) system and 0.03 cm/sec for the Al/PBN/stainless steel system in both normal and reduced gravity. A vapor volume was always present within the crucible. The Al/PBN and aluminum/titanium diboride (Al/TiB_2) systems were surface tension dominated in normal gravity, having Bond numbers of 0.25. The Al/PBN/stainless steel system had a Bond number of 4.0 in normal gravity. The PBN and TiB_2 crucibles were vacuum sealed, and the stainless steel container was sealed in an $Ar\text{-}4H_2$ environment. No dissolved gas was intentionally added to the molten aluminum.

The conclusions for the Al/PBN system are summarized as follows:

1. The concave solid/liquid interface indicates that a horizontal temperature gradient existed and that natural convective flow was present in the melt. The Marangoni numbers for this system (both parallel and perpendicular to the free surface) reveal that surface-tension-driven convection was also occurring in the liquid aluminum. The dynamic Bond number for this system indicates that natural convection and surface-tension-driven convection were of similar strength in normal gravity (1g) but that surface-tension-driven convection dominated in reduced gravity. Furthermore, fluid motion due to solid/liquid phase change also existed and this velocity moved toward the solidification front because $\rho_s > \rho_l$. However, the fluid flow by these three mechanisms did not appear to influence the void behavior because the rapid freezing rate showed no variation with gravitational conditions, and there were no bubbles in the melt that could become entrained in the flow.

2. Void formation in the nonwetting crucible was similar in normal and reduced gravity. Because of the material shrinkage (7 percent), a larger vapor volume formed at the top of the container. Because the system was dominated by surface tension forces in normal gravity and a rounded container (bathtub shape) was used, no liquid/vapor reorientation occurred in reduced gravity.

3. In the case where wetting existed between the molten aluminum and the crucible lid, dominant surface tension forces caused the aluminum to remain attached to the lid in reduced gravity. In normal gravity the aluminum detached from the lid during solidification. In both cases volumetric shrinkage was accommodated by the vapor cavity initially present; however, two smaller voids formed in the reduced-gravity case and only one large void formed during the normal-gravity test.

The conclusion for the Al/TiB_2 system is as follows: The one reduced-gravity test with the Al/TiB_2 system was unsuccessful. The vacuum seal had been broken just after quenching when cracks formed in the crucible bottom. These cracks most likely resulted from thermal shock.

The conclusions for the Al/PBN/stainless steel system are summarized here:

1. Void formation in the nonwetting crucible was similar in normal and reduced gravity. The flat meniscus in 1g changed to a constant surface curvature intersecting the container wall at the contact angle in ±0.02g. This transition was not dramatic because the 1g Bond number was 4. At either gravity level one large void formed symmetrically across the top of the container.

2. In the case where wetting existed between the molten aluminum and the left side wall and lid, the liquid aluminum flowed in the corners along this side during reduced gravity. On the nonwetting side the fluid moved down, while in reduced gravity, to accommodate the flow of liquid climbing the wetted side. This resulted in one large void forming along the right side of the container up to the top. A similar asymmetric result was reported by Weislogel (ref. 47) in which a barrier coating was used on one side of the container. This caused the liquid flow to be impeded on the coated side but readily drawn up the walls on the uncoated side. In the normal-gravity test the PBN was wetted by the molten aluminum on both the left and right sides. Upon solidification one large void formed symmetrically at the top of the container. The wetting conditions had changed from the 1g tests to the reduced-gravity tests.

General conclusions were drawn as follows: In all tests conducted no voids (>1 mm) were detected at the solid/liquid interface or in the solid aluminum for either gravity level. In two of the three prior reduced-gravity experiments that have investigated bubble motion and void formation (refs. 11 and 12) dissolved gases were rejected during solidification. The bubbles that were formed at the growth interface produced randomly distributed voids in reduced gravity because buoyancy-driven convection was minimized. The degassed aluminum in the present experiment appeared to produce fewer voids in reduced gravity, as shown in figures 36(d), 37(d), 39(c), and 41(c) because voids originated only from the initial ullage volume. This same general result was reported by Stähle and Lindner (ref. 13), who used a degassed, nonwetting LiF-graphite system. The present experiment demonstrated that a unique and different vapor cavity or void is formed during solidification in reduced gravity as compared with normal gravity. Figure 37 illustrates how surface tension produced a unique void formation, and figure 39 illustrates how reorientation of the liquid/vapor interface produced a different void position. These tests illustrate how the contact angle θ between the phase-change material (aluminum) and its container (pyrolytic boron nitride) and the container geometry can dictate void formation during solidification in reduced gravity.

To the author's knowledge this is the first use of a real-time radiographic viewing system to observe solidification in reduced gravity. This system produced images with 1-mm resolution, a clear liquid/vapor interface, and, with the assistance of image processing, the solid/liquid interface.

6.2 Recommendations for Further Research

Future work should focus on two types of fluids: degassed (pure) fluids and those containing a dissolved gas. Several parameters influence void behavior and should be studied, such as geometry (including fins, channels, and porous structures), wetting, solidification rate, melting rate, and thermal boundary conditions.

Several investigators (refs. 7 and 11) believe that a fluid containing a dissolved gas may cause a random distribution of voids in the solid in reduced gravity; this result is desirable and should be pursued further. Specifically, in a gas-saturated liquid bubbles are most likely to form in the liquid just ahead of the solid/liquid interface because the gas is much less soluble in the solid than in the liquid. At rapid solidification rates the bubbles may be engulfed by the solid, whereas slow growth rates tend to push the bubbles at the interface. The terminal velocity of a small-diameter bubble in an isothermal environment is proportional to the gravitational acceleration (ref. 48); therefore, in reduced gravity (10^{-5}g) the bubbles will have a tendency to remain static. Also, low gravity is expected to favor bubble nucleation because of a reduced hydrostatic head (lower liquid pressure enhances bubble formation) and decreased free convection (ref. 11). (The concentrated dissolved gas ahead of the solid/liquid interface will not be mixed by convective flow.)

The interaction of bubbles with solidification interfaces has been studied experimentally by using carbon tetraboride (CBr_4) in normal and reduced gravity (ref. 11). Gas bubbles that formed in normal gravity often departed the liquid/solid interface, leaving the specimen generally free of large internal voids. In a reduced-

gravity environment a greater void density was observed in solidified samples of CBr_4 than had been observed in normal gravity. Studies such as these should be pursued further.

Other researchers have proposed using fins or encapsulating the phase-change material (PCM) within a porous structure (refs. 6 and 10). Such concepts should enhance heat transfer because the thermal conductivity of the porous system or fins is higher than the thermal conductivity of the PCM and would produce a favorable void distribution. However, structural integrity problems must be solved if these concepts are to become viable. Using channels located on the outer wall (ref. 13) has also been studied. In this system the PCM expands into channels during melting but withdraws from the channels during solidification owing to the capillary pressure. The container is not wetted by the PCM. This system appears useful, but it is important that the solid PCM does not withdraw too far from the outer wall. Too great a withdrawal could result in overheating the outer wall during melting of the PCM.

In space power applications it is desirable to have small randomly distributed voids throughout the PCM. During melting, the liquid, which normally has a larger volume than the solid, will expand into these void regions and thus ease any stress buildup on the container walls. This result suggests the use of a dissolved gas or perhaps a porous structure in the PCM. Also, it is desirable that the liquid PCM be in contact with the container surfaces to allow controlled heat flow to take place and prevent "hot spots" from occurring. This contact can be achieved by selecting a container in which the molten PCM will wet ($\theta < 90°$) and using a geometry in which $\theta + \alpha/2 < 90°$ is satisfied in the corners to enable the liquid to reach as much of the container surface area as possible prior to solidification. This effect was demonstrated in the present experiment for an asymmetric case (figs. 39(b) and (c)).

One possible design, assuming a cylindrical geometry, is a toroid with a "star"-shaped outer wall and fins positioned axially from the inner to the outer wall as shown in figure 42. The optimal *l/d* ratio for the Space Station *Freedom* toroidal canister was determined to be approximately 0.5 (ref. 49) to minimize the stress concentration at the base of the side wall arising from the expansion of the container due to heat input. In the proposed star-shaped design the selected *l/d* ratio was 1.0 because the fins would assist in transferring the heat to the inner tube. This design requires the container to be wetted by the molten PCM. The tips of the star-shaped outer shell would always contain some PCM because capillary forces cause the fluid to flow in a wedge, as shown in figure 11(a), instead of pushing it out as in Stähle's channel concept, as shown in figure 2, or allowing the void to form randomly as expected in the *Freedom* design, as shown in figure 43. The points of the star are slightly rounded to reduce the stress concentration, but Concus and Finn (ref. 30) have shown that the fluid will flow in a wedge even if the wedge has a small radius of curvature. In the representative concept shown in figure 42 the eight-point star design has a 90° wedge angle and, accounting for the radius of curvature in the wedge, the contact angle must be $\theta \leq 28°$. In order to increase the allowable contact angle, the wedge angle must decrease. The fins would meet the end walls at a 90° angle, forming a wedge; this angle would allow the PCM to flow between the inner and outer radii at the end walls. Each fin will act as a heat path, allowing the solid PCM to melt along the fin first and provide a liquid path to the void (or voids), similar to Tanaka's concept shown in figure 44 (ref. 50). This proposed geometry still needs further investigation in three areas: first, a structural analysis emphasizing the stress concentration at the rounded points; second, a computational heat transfer analysis of the canister to optimize the *l/d* ratio; and third, a material compatibility study between the PCM and container to solve any corrosion problems. Casting the container, perhaps by the lost-wax process, may be a viable fabrication technique assuming proper wall thicknesses are determined. Casting, as opposed to forming each segment and brazing them together, reduces the number of weld seams; only welding the end cap to the open-ended container would be required after it was filled with the PCM. Electron beam welding is a possible joining technique because it is clean and accurate. The star-shaped toroid can be considered as a collection of unit volumes each approximating a rhombic prism. Isothermal free-surface studies in reduced gravity have been conducted by several investigators (refs. 31 and 33) using this geometry. A drawing of a typical liquid/gas interface shape during reduced gravity in a rhombic prism with $\alpha/2 + \theta < 90°$ is illustrated in

figure 45 (ref. 31). This drawing is based on actual reduced-gravity results: Fluorinert (liquid) was tested in a Plexiglas prism. These reduced-gravity tests were conducted on a KC–135 aircraft while the aircraft was flown through a parabolic trajectory. This liquid/gas orientation in the rhombic prism provides an approximate initial condition of the molten PCM in each segment of the star-shaped toroid. The anticipated void position after solidification of the PCM in microgravity is shown in figure 46. In this design the voids are uniformly distributed within the canister because of the rhombic-like shape of each segment, but their position in the solid will also be influenced by the uniformity and rate of heat removal.

APPENDIX A
ASE FLIGHT CHECKLIST PROCEDURE

Crucible: _____ Flight date: _____
Data file: _____ No. of trajectories: _____

GROUND

1. Fill water tank to 100-percent fill level and run pump by means of data acquisition keypad.

PREFLIGHT

2. Set x-ray unit exposure time to 30 sec.
3. PBN crucible: Set x-ray intensity to 40 kV.

   TiB_2 crucible: Set x-ray intensity to 60 kV.

   Stainless steel crucible: Set x-ray intensity to 80 kV.
4. PBN crucible: Set camera F-stop to 5.6; focus to near ∞.

   TiB_2 crucible: Set camera F-stop to 8.0; focus to near ∞.

   Stainless steel crucible: Set camera F-stop to 5.6; focus to near ∞.
5. Clean mirror for video camera.
6. Provide two program disks and two DOS disks.
7. Provide two S–VHS tapes.
8. Provide extra battery for S–VHS recorder fully charged. Install other battery in recorder.
9. Provide extra computer key and x-ray unit key.
10. Provide two extra fuses.
11. Check that all electrical connectors and plugs are connected.
12. Check that all thermocouple mini-connectors are connected in proper numerical sequence.
13. Check that recorder S–VHS switch is on.
14. Enter time, date, and crucible number on titler.
15. Check that all occupants are wearing x-ray monitoring radiation badges.
16. Visually check lead shielding enclosure.
17. Perform mini-run: Turn on pump (quench) and x-ray unit to check for noise on monitor; preheat aluminum to 40 °C.

    a. Ramp rate (deg C/min) = 12
    b. Temp. diff. (deg C) = 2
    c. Soak temp. (°C) = 40
    d. Soak time (min) = 1
    e. Temp. diff. in soak (deg C) = 0
    f. Experiment ID code = 000

18. Preheat to liquid aluminum state (see "Turn data acquisition unit ON" and following):
    a. Ramp rate (deg C/min) = 12
    b. Temp. diff. (deg C) = 0
    c. Soak temp. (°C) = 672
    d. Soak time (min) = 2
    e. Temp. diff. in soak (deg C) = 0
    f. Experiment ID code = 000
19. Turn S–VHS recorder ON.
20. Press PLAY and RECORD.
21. Press x-ray deadman switch; hold for 30 sec (film liquid state and play back the tape).
22. Press STOP on S–VHS recorder; then press OFF.

AFTER AIRCRAFT POWER IS ON (prior to takeoff)

23. Turn experiment power ON (this turns titler and camera on).
24. Turn visicorder power ON (let pilots perform this step during zero-g).
25. Turn data acquisition unit ON.
26. Turn computer key to ON position.
27. Insert DOS disk in drive A.
28. After booting is complete, insert DOS disk in drive B.
29. Insert program disk in drive A.
30. Start computer program by means of keyboard. A:\>almicrog (heat furnace to 670 °C).
31. Press reset (black) button on PCU:
    Check resistance (3.3 ohms); check thermocouples for heater control (top, TC 1; bottom, TC 4); check heater gains (top, 4; bottom, 5).
32. Input test parameters by means of keyboard (if thermocouple malfunctions, reset parameters using Turbo-Pascal):
    a. Ramp rate (deg C/min) = 20
    b. Temp. diff. (deg C) = 2
    c. Soak temp. (°C) = 675
    d. Soak time (min) = 1
    e. Temp. diff. in soak (deg C) = 0
    f. Experiment ID code = _____
    (choices: 001, 002, 003, 004, 005, 006)
33. PBN crucible: Set F-stop on camera to 5.6; focus to near ∞; tighten camera mount set screw.
    TiB_2 crucible: Set F-stop on camera to 8; focus to near ∞; tighten camera mount set screw.
    Stainless steel crucible: Set F-stop on camera to 5.6; focus to near ∞; tighten camera mount set screw.
34. Turn x-ray unit key to ON position.
35. Set x-ray unit exposure time to 30 sec.
36. PBN crucible: Set X-ray unit intensity to 40 kV.

TiB_2 crucible: Set X-ray unit intensity to 60 kV.

Stainless steel crucible: Set x-ray unit intensity to 80 kV.

37. Check that battery is in recorder and fully charged.
38. Pull shades down near computer.
39. Recheck settings.

AFTER 40-SECOND CALL (prior to entering trajectory)

40. Turn S–VHS recorder ON.
41. Press PLAY and RECORD (S–VHS unit).
42. (Press visicorder ON; pilots perform this step.)

AFTER 20-SECOND CALL (prior to entering trajectory)

43. Press F on keyboard; (press A to abort if necessary).
    (Starts 60-sec preprogrammed quench for the stainless steel container system. Note: for the pyrolytic boron nitride system instruction 43 is done immediately after entering the trajectory because only a 20-sec quench is used.)

IMMEDIATELY PRIOR TO ENTERING TRAJECTORY

44. Press x-ray deadman switch and hold. (Activates x-ray unit for 25 to 30 sec.)

END OF TRAJECTORY

45. Release x-ray deadman switch.
46. Press STOP on S–VHS recorder; then press OFF (to save battery charge).
47. Write down observations. If more trajectories are scheduled, go to "40-SECOND CALL." (Program will perform three quenches.)
48. Press visicorder OFF.

AFTER ALL TRAJECTORIES ARE COMPLETED

49. Turn x-ray unit key to OFF position.
50. Turn S–VHS recorder OFF.
51. Turn computer key to OFF position.
52. Turn dc "tri-amp" (PCU) OFF.

53. Turn data acquisition unit OFF.
54. Turn visicorder power OFF.
55. Turn experiment power OFF.

APPENDIX B
ALUMINUM PROPERTIES
[From reference 51.]

Melting temperature T_{mp} = 660 °C

Latent heat of fusion L = 395.6 J/g

Liquid thermal conductivity k_l = 94.03 J/sec-m-K at 660 °C

Solid thermal conductivity k_s = 217.6 J/sec-m-K at 660 °C

Surface tension σ = 914 dynes/cm at 660 °C

Surface tension σ = 865 dynes/cm at 800 °C

Liquid density ρ_l = 2.368 g/cm^3 at 660 °C

Solid density ρ_s = 2.55 g/cm^3 at 660 °C

Dynamic viscosity μ = 0.01389 g/cm-sec at 662 °C

Dynamic viscosity μ = 0.01175 g/cm-sec at 768 °C

Liquid heat capacity $C_{p,l}$ = 1.086 J/g-K at 727 °C

Solid heat capacity $C_{p,s}$ = 1.185 J/g-K at 627 °C

APPENDIX C
SYMBOLS

a	thermal diffusivity, $k/\rho C_p$
Bo	Bond number, $\rho_l g w^2/\sigma$
Bo_{dyn}	dynamic Bond number, $\rho\beta g h^2/(\partial\sigma/\partial T)$
C	mean curvature of free surface
C_p	specific heat
d	diameter
g	gravitational constant
h	height
I	current
K	proportional gain
k	thermal conductivity
L	latent heat of fusion
l	length
Ma	Marangoni number, $-(\partial\sigma/\partial T)\Delta T w/\mu a$
P	pressure
Pwr	power
R	resistance
Ra	Rayleigh number, $g\beta\ \Delta T\ w^3/va$
r	radius
Ste	Stefan number, $C_p(T_{mp} - T_{ref})/L$
T	temperature
TC	thermocouple
t	time
V	voltage
v	velocity
w	characteristic length
$X(t)$	solidification distance
x	distance
α	dihedral angle
β	coefficient of thermal expansion, $-(1/\rho)(\partial\rho/\partial T)_p$
θ	contact angle

λ	phase growth constant
μ	dynamic viscosity
ν	kinematic viscosity, μ/ρ
ρ	density
σ	surface tension

Subscripts:

g	gas
i	integral
l	liquid
max	maximum
mp	melting point
q	quench
ref	reference point
s	solid
sk	soak
w	wall
0	ambient or zero point

REFERENCES

1. Kerslake, T.W.: Experiments With Phase Change Thermal Energy Storage Canisters for Space Station *Freedom*. IECEC'91: Proceedings of the 26th Intersociety Energy Conversion Engineering Conference, Vol. 1, American Nuclear Society, LaGrange Park, IL, 1991, pp. 248–261.

2. NASA Lewis Research Center 1989 Annual Report. NASA TM–102296, 1989, pp. 156, 157, 181.

3. Petrash, D.A.; Nussle, R.C.; and Otto, E.W.: Effect of Contact Angle and Tank Geometry on the Configuration of the Liquid-Vapor Interface During Weightlessness. NASA TN D–2075, 1963.

4. Symons, E.P.: Zero-Gravity Equilibrium Configuration of Liquid-Vapor Interface in Toroidal Tanks. NASA TN D–6076, 1970.

5. Namkoong, D.: Measured Performance of a 1089 K (1500 °F) Heat Storage Device for Sun-Shade Orbital Missions. NASA TN D–6665, 1972.

6. Sedgwick, L.M.; Nordwall, H.L.; Kaufmann, K.J.; and Johnson, S.D.: A Brayton Cycle Solar Dynamic Heat Receiver for Space. IECEC'89: Proceedings of the 24th Intersociety Energy Conversion Engineering Conference, Vol. 2, Institute of Electrical and Electronics Engineers, New York, 1989, pp. 905–909.

7. Sulfredge, C.D.; Chow, L.C.; and Taghavi, K.A.: Void Formation in Radial Solidification of Cylinders. J. Sol. Energy Eng., vol. 114, Feb. 1992, pp. 32–39.

8. Taghavi, K.; Chow, L.C.; and Solaiappan, O.: Void Formation in Unidirectional Solidification in 1g and 0g. Presented at the Workshop on the Commercialization of Space Fluid Management, Sponsored by NASA Marshall Space Flight Center, Huntsville, AL, Mar. 21–22, 1990.

9. Takahashi, Y.; Abe, Y.; Sakamoto, R.; Tanaka, K.; and Kamimoto, M.: High Temperature Fluoride Composites for Latent Thermal Storage in Advanced Space Solar Dynamic Power System. IECEC'89: Proceedings of the 24th Intersociety Energy Conversion Engineering Conference, Vol. 2, Institute of Electrical and Electronics Engineers, New York, 1989, pp. 959–963.

10. Tanaka, K.; Abe, Y.; Kanari, K.; Nomura, O.; and Kamimoto, M.: Advanced Concepts for Latent Thermal Energy Storage for Solar Dynamic Receivers. Space Power, vol. 8, no. 4, 1989, pp. 425–434.

11. Papazain, J.M.; and Wilcox, W.R.: Bubble Behavior During Solidification in Low Gravity—Spar 1 and Spar 3 Flights. NASA CR–161159, 1979.

12. Klein, H.; Nahle, R.; and Wanders, D.: Metal-Like Solidification of a Multiphase Dispersion in Low Gravity During a Space Shuttle Flight. Z. Flugw. Welt., vol. 9, Jan.–Feb. 1985, pp. 14–20.

13. Stähle, H.J.; and Lindner, F.: Heat Storage Module. European Space Power Conference, ESA SP–294, J. Landeau, ed., European Space Agency, Paris, France, 1989.

14. Skarda, J.R.: Thermal Modeling With Solid/Liquid Phase Change of the Thermal Energy Storage Experiment. NASA TM–103770, 1991.

15. Yang, J.Y.; and El-Genk, M.S.: Shrinkage Void Formation and Its Effect on Freeze and Thaw Processes of Lithium and Lithium-Fluoride for Space Applications. IECEC'91: Proceedings of the 26th Intersociety Energy Conversion Engineering Conference, Vol. 1, American Nuclear Society, LaGrange, IL, 1991, pp. 462–466.

16. Darling, D.; Namkoong, D.; and Skarda, J.R.: Modeling Void Growth and Movement With Phase Change in Thermal Energy Storage Canisters. AIAA Paper 93–2832, 1993.

17. Flemings, M.C.: Solidification Processing. Ch. 1, 5, and 6, McGraw-Hill, New York, 1974.

18. Reynolds, W.C.; Saad, M.A.; and Satterlee, H.M.: Capillary Hydrostatics and Hydrodynamics at Low g. Report LG–3. National Science Foundation, Grant No. NSFG–20090, Sept. 1964.

19. Gupta, A.K.; Saxena, B.K.; Tiwari, S.N.; and Malhotra, S.L.: Review: Pore Formation in Cast Metals and Alloys. J. Mater. Sci., vol. 27, 1992, pp. 853–862.

20. Chalmers, B.: Principles of Solidification. Wiley, New York, 1964, pp. 192, 228.

21. Arpaci, V.S.: Conduction Heat Transfer. Ch. 2, Addison-Wesley, Menlo Park, CA, 1966.

22. Cole, R.; Papazian, J.M.; and Wilcox, W.R.: Bubble Departure Radii at Solidification Interfaces. Int. J. Heat Mass Transfer, vol. 23, 1980, pp. 219–224.

23. Carslaw, H.S.; and Jaeger, J.C.: Conduction of Heat in Solids. Clarendon Press, Oxford, England, 1959, pp. 286–292.

24. Chiaramonte, F.P.; and Rosenthal, B.N.: Wettability of Pyrolytic Boron Nitride by Aluminum. J. Am. Ceram. Soc., vol. 74, no. 3, Mar. 1991, pp. 658–661.

25. Xue, X.M.; Wang, J.T.; and Quan, M.X.: Wettability and Spreading Kinetics of Liquid Aluminum on Boron Nitride. J. Mater. Sci., vol. 26, Dec. 1991, pp. 6391–6395.

26. Xue, X.M.; Wang, J.T.; and Zhao, F.M.: Penetration and Adhesion Behavior of Boron Nitride by Liquid Aluminum. J. Mater. Sci. Lett., vol. 11, 1992, pp. 199–201.

27. John, H.; and Hausner, H.: Wetting of Aluminum Oxide by Liquid Aluminum. Int. J. High Technol. Ceram., vol. 2, 1986, pp. 733–778.

28. Brennan, J.J.; and Pask, J.A.: Effect of Nature of Surfaces on Wetting of Sapphire by Liquid Aluminum. J. Am. Ceram. Soc., vol. 51, no. 10, 1968, pp. 569–573.

29. Laurent, V.; Chatain, D.; and Eustathopoulos, N.: Wettability of SiC by Aluminum and Al-Si Alloys. J. Mater. Sci., vol. 22, no. 1, 1987, pp. 244–250.

30. Concus, P.; and Finn, R.: Dichotomous Behavior of Capillary Surfaces in Zero Gravity. Micrograv. Sci. Technol., vol. 3, Sept. 1990, pp. 87–92.

31. Langbein, D.; Grossbach, R.; and Heide, W.: Parabolic Flight Experiments on Fluid Surfaces and Wetting. Appl. Micrograv. Technol., vol. 2, Feb. 1990, pp. 198–211.

32. Adamson, A.W.: Physical Chemistry of Surfaces. Second ed., John Wiley & Sons, New York, 1967, pp. 9–12.

33. Weislogel, M.M.; and Ross, H.D.: Surface Reorientation and Settling in Cylinders Upon Step Reduction in Gravity. Appl. Micrograv. Technol., vol. 3, May 1990, pp. 24–32.

34. Lekan, J.: Microgravity Research in NASA Ground-Based Facilities. AIAA Paper 89–0236, 1989.

35. Chiaramonte, F.P.; Foerster, G.; Gotti, D.J.; Neumann, E.S.; Johnston, J.C.; and De Witt, K.J.: Initial Study of Void Formation During Aluminum Solidification in Reduced Gravity. J. Spacecraft Rockets, vol. 29, no. 5, Sept.–Oct., 1992, pp. 704–708.

36. Millis, M.G.: Acceleration Display System for Aircraft Zero-Gravity Research. NASA TM–87358, 1987.

37. Boyer, E.D.; Rieke, W.J.; and Grodsinsky, C.M.: Microgravity Research on the NASA Lewis Learjet Test Facility. AIAA Paper 93–0573, 1993.

38. Quinn, R.A.; and Sigl, C.C., eds.: Radiography in Modern Industry. 4th ed., Eastman Kodak Co., Cat. No. 145–5408, Rochester, New York, 1980, Ch. 14.

39. Chiaramonte, F.P.; and Sudsina, M.W.: Joining Ceramics by Brazing. NASA Tech Briefs, vol. 16, no. 10, Oct. 1992, p. 97.

40. Carruthers, J.R.: Thermal Convection in Horizontal Crystal Growth. J. Crystal Growth, vol. 2, no. 1, 1968, pp. 1–8.

41. Kim, D.H.; and Brown, R.A.: Transient Simulations of Convection and Solute Segregation of GaAs Growth in Gradient Freeze Furnace. J. Crystal Growth, vol. 109, no. 1, 1991, pp. 66–74.

42. Arnold, W.A.; Jacqmin, D.A.; Gaug , R.L.; and Chait, A.: Three-Dimensional Flow Transport Modes in Directional Solidification During Space Processing. J. Spacecraft Rockets, vol. 28, no. 2, Mar.–Apr. 1991, pp. 238–243.

43. Holland, L.R.: Crucible Surface, Thermal Refraction, Boundaries and Interface Shape in Melt Growth. J. Crystal Growth, vol. 96, no. 3, July 1989, pp. 577–583.

44. Schwabe, D.: Surface-Tension-Driven Flow in Crystal Growth Melts. Superhard Materials, Convection, and Optical Devices, (series "Crystals," Vol. II), R.B. Heimann, ed., Springer, New York, 1988, pp. 75–112.

45. Rhee, S.K.: Wetting of Ceramics by Liquid Aluminum. J. Am. Ceram. Soc., vol. 53, no. 7, 1970, pp. 386–389.

46. Montgomery, L.: Method for Metallizing a Boron Nitride Containing Body. U.S. Patent 3,515,574, June 2, 1970.

47. Weislogel, M.W.: Capillary Surface Reorientation During Brief Periods of Reduced Gravity: Effects of Surface Coatings. Presented at the 7th International Conference of Partitioning in Aqueous Two-Phase Systems, New Orleans, LA, June 1991.

48. Haggard, J.B., Jr.; and Masica, W.J., Jr.: Motion of Single Bubbles Under Low Gravitational Conditions. NASA TN D–5462, 1969.

49. Kerslake, T.W.: Parametric Studies of Phase Change Thermal Energy Storage Canisters for Space Station *Freedom*. NASA TM–105350, 1992.

50. Tanaka, K.; Abe, Y.; Takahashi, Y.; Kamimoto, M.; and Tanatsugu, N.: Latent Thermal Storage for Space Solar Dynamic Power System. IECEC'88: Proceedings of the 23rd Intersociety Energy Conversion Engineering Conference, Vol. 3, American Society of Mechanical Engineers, New York, 1988, pp. 63–68.

51. Van Horn, K.R., ed.: Aluminum. Vol. 1: Properties, Physical Metallurgy and Phase Diagrams. American Society for Metals, Metals Park, OH, 1967, pp. 1–30.

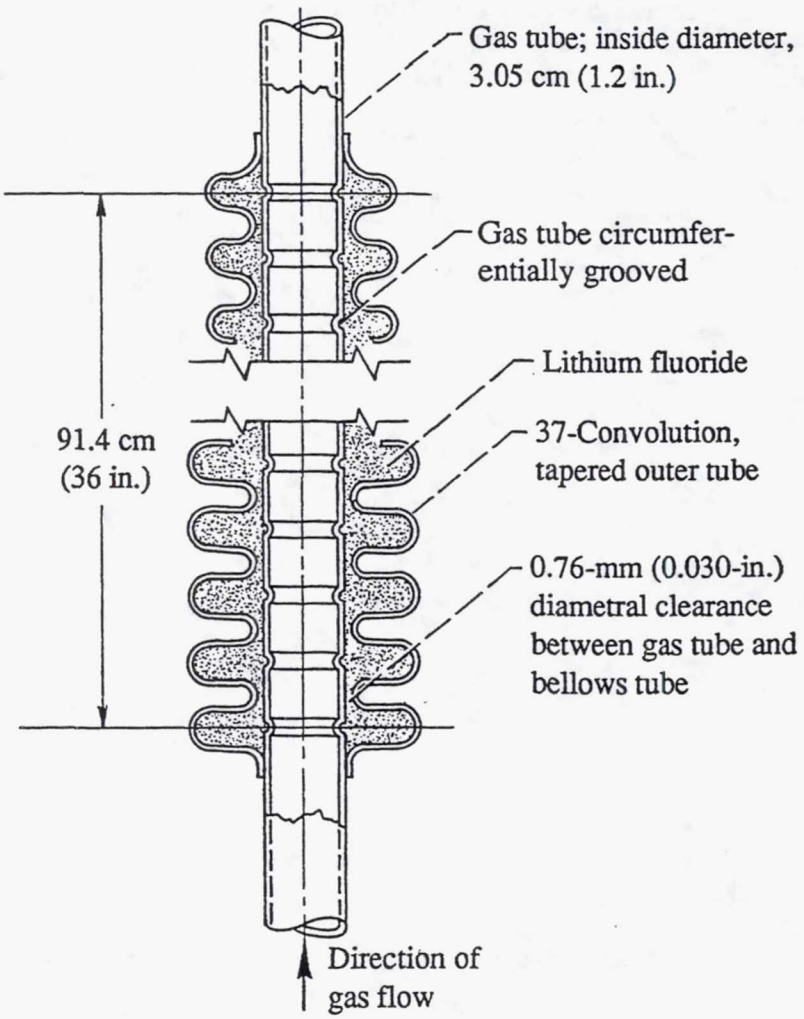

Figure 1.—Heat transfer/heat storage solar receiver tube; convoluted design. From reference 5.

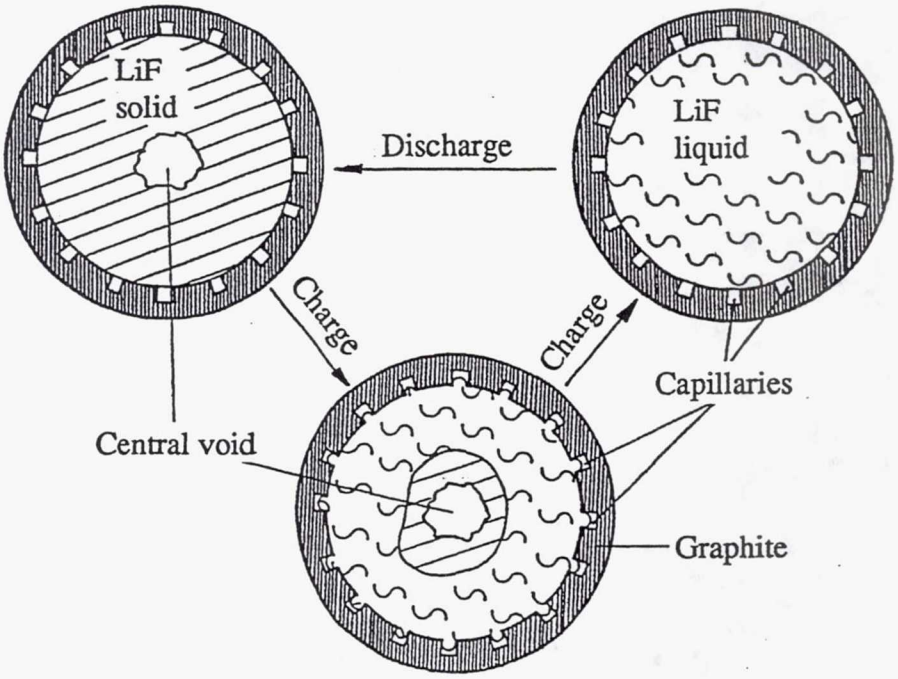

Figure 2.—Heat storage canister with capillary channels showing expected void position in reduced gravity. From reference 13.

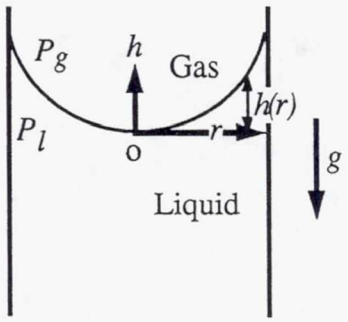

Figure 3.—Liquid/gas interface.

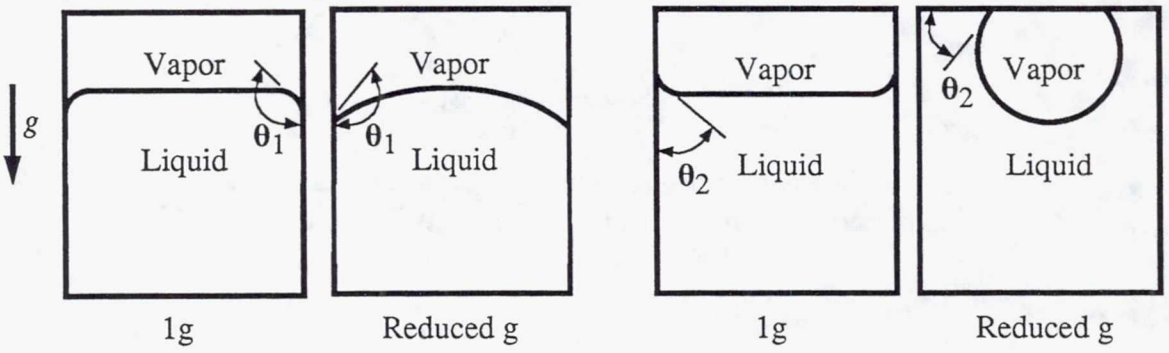

(a) $\theta_1 > 90°$ (nonwetting). (b) $\theta_2 < 90°$ (wetting).

Figure 4.—Interface configurations at normal and reduced gravity for nonwetting and wetting fluids. From reference 3.

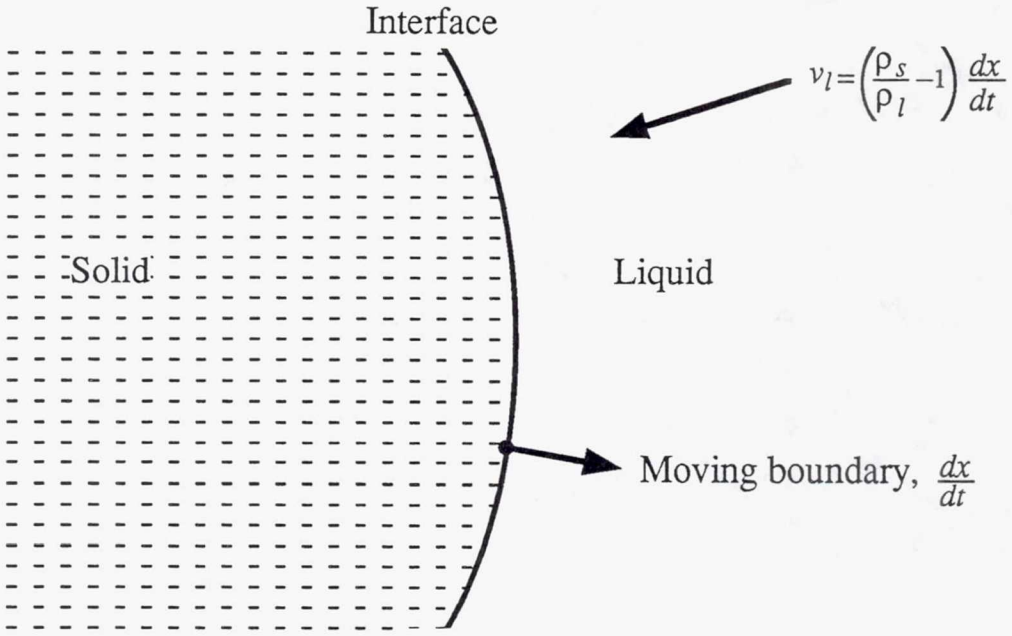

Figure 5.—Induced liquid velocity toward solid/liquid interface due to solidification shrinkage. From reference 21.

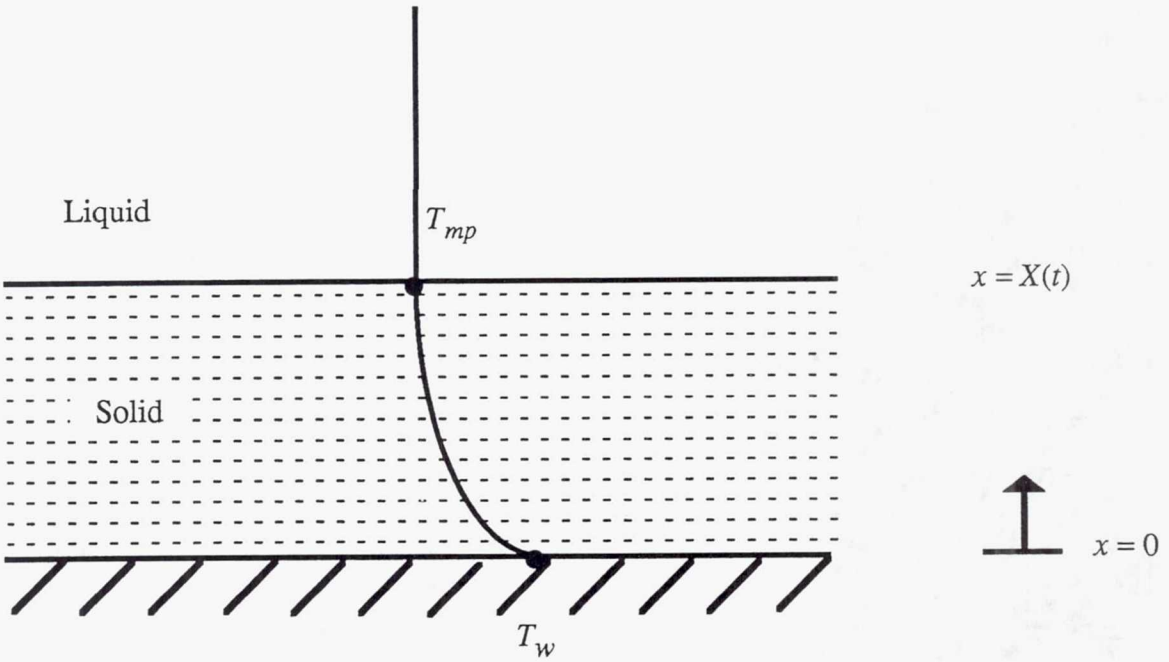

Figure 6.—Solidification at plane wall.

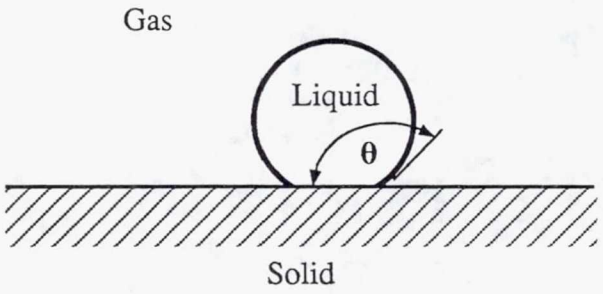

Figure 7.—Contact angle **θ** of liquid drop resting on solid substrate.

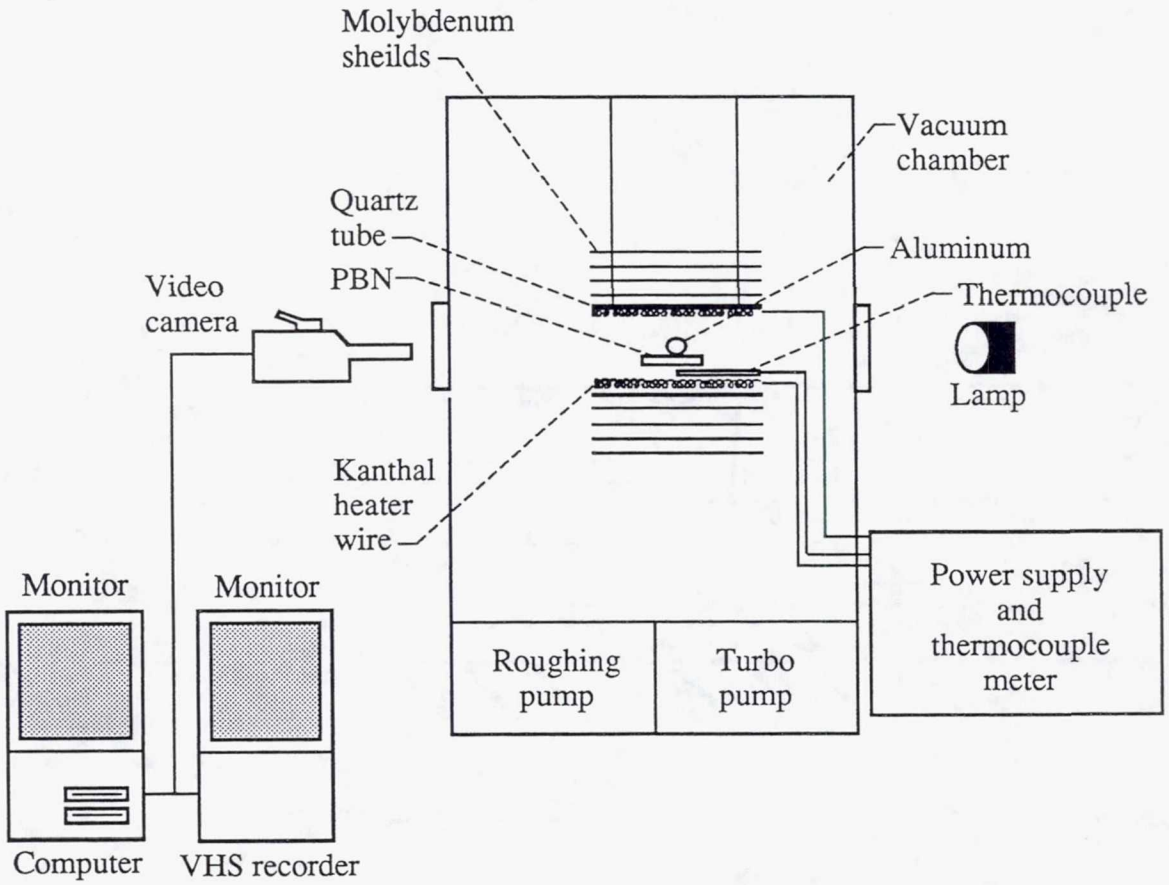

Figure 8.—Schematic diagram of sessile drop apparatus.

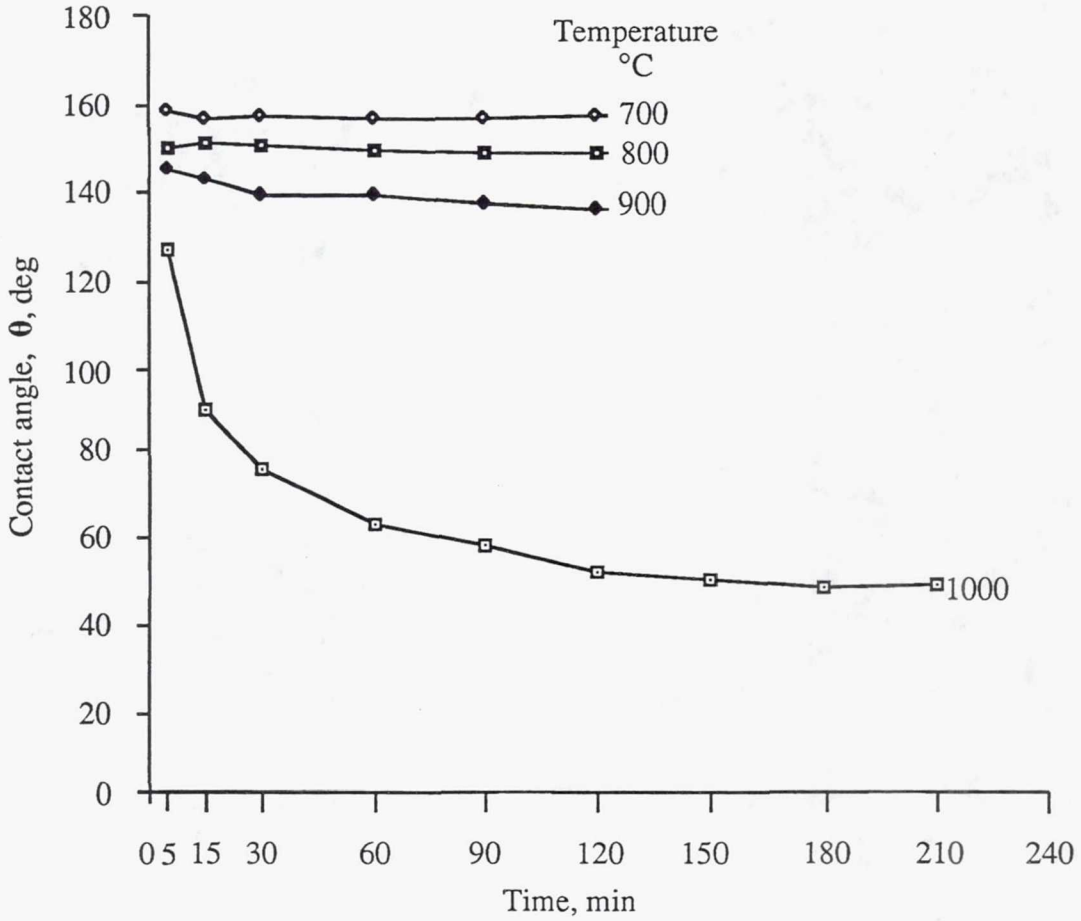

Figure 9.—Time dependence of contact angle for molten aluminum on pyrolytic boron nitride at various temperatures in vacuum of approximately 660 μPa.

(a) 700 °C.

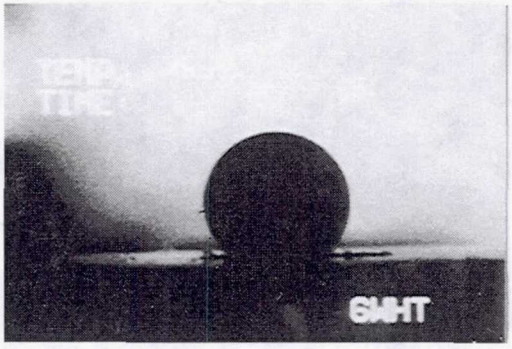

(b) 800 °C.

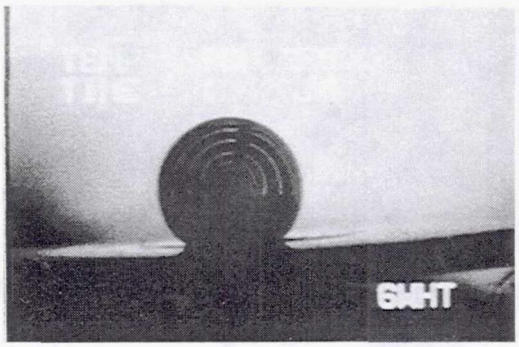

(c) 900 °C.

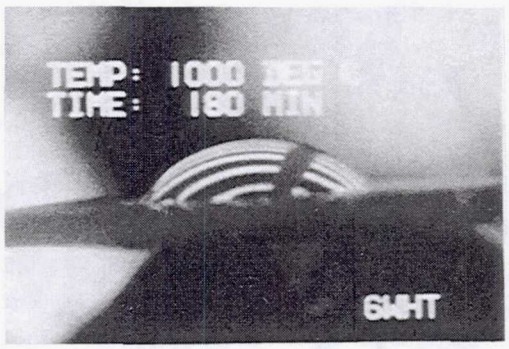

(d) 1000 °C.

Figure 10.—Sessile drops of liquid aluminum on pyrolytic boron nitride at various temperatures after contact angle has stabilized in vacuum of approximately 660 μPa. (The white circular lines in the 900 and 1000 °C cases are reflections of the glowing heating wire on the aluminum drop.)

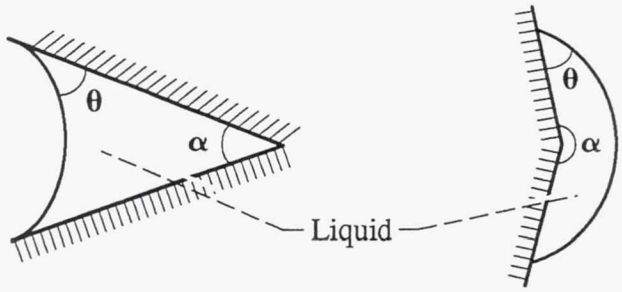

(a) Fluid will flow. (b) Fluid will not flow.

Figure 11.—Fluid menisci in solid wedge. From reference 31.

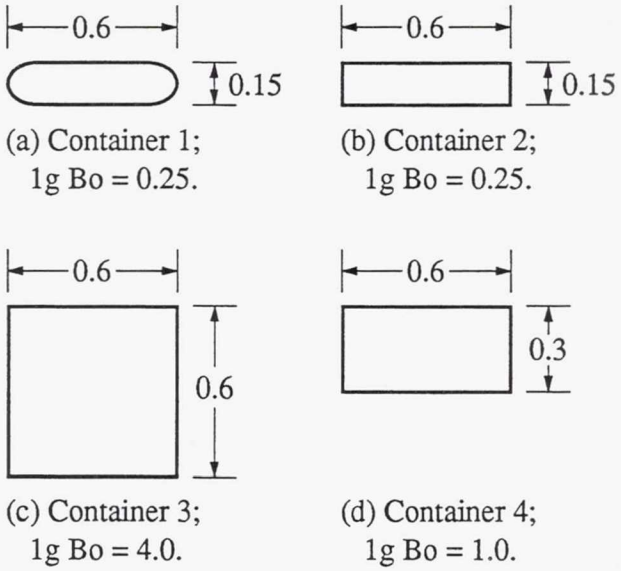

(a) Container 1; 1g Bo = 0.25.

(b) Container 2; 1g Bo = 0.25.

(c) Container 3; 1g Bo = 4.0.

(d) Container 4; 1g Bo = 1.0.

Figure 12.—Schematic drawing of Plexiglas containers, top view. (All dimensions are in centimeters.)

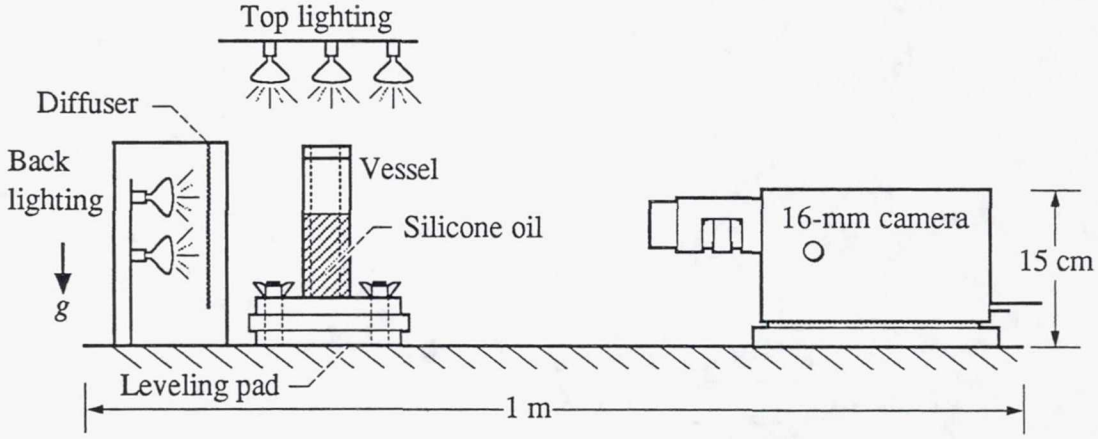

Figure 13.—Schematic of apparatus for capillary surfaces in corners experiment. From reference 33.

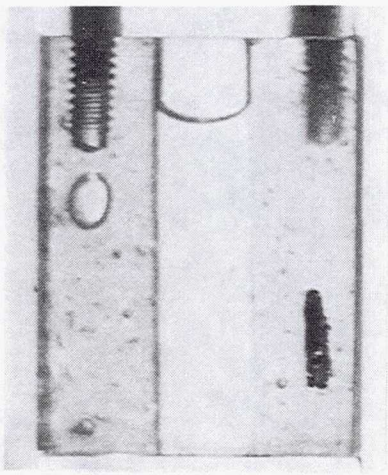

(a) 1g; 75-percent fill.

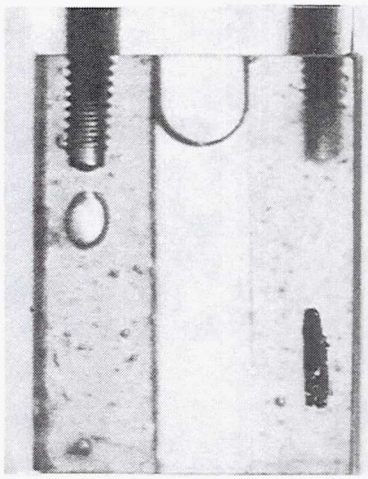

(b) 10^{-5}g; 75-percent fill.

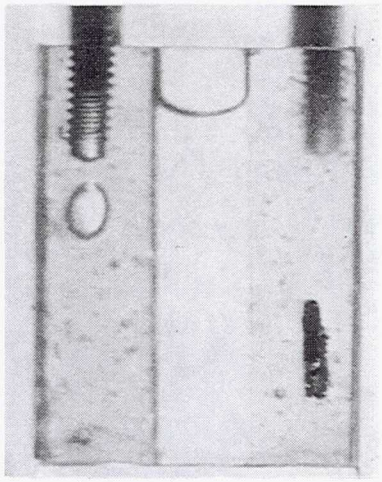

(c) 1g; 90-percent fill.

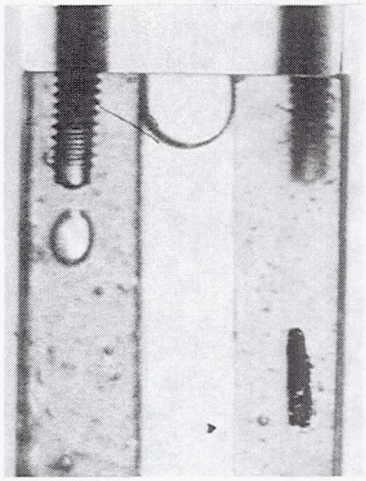

(d) 10^{-5}g; 90-percent fill.

Figure 14.—Normal- and reduced-gravity interfacial surfaces from photographic data using silicone oil in rounded, "bathtub" Plexiglas container 1. Bo = 0.25 in 1g. (The small bubble in the left side of each figure is air trapped in the epoxy used to join the Plexiglas.)

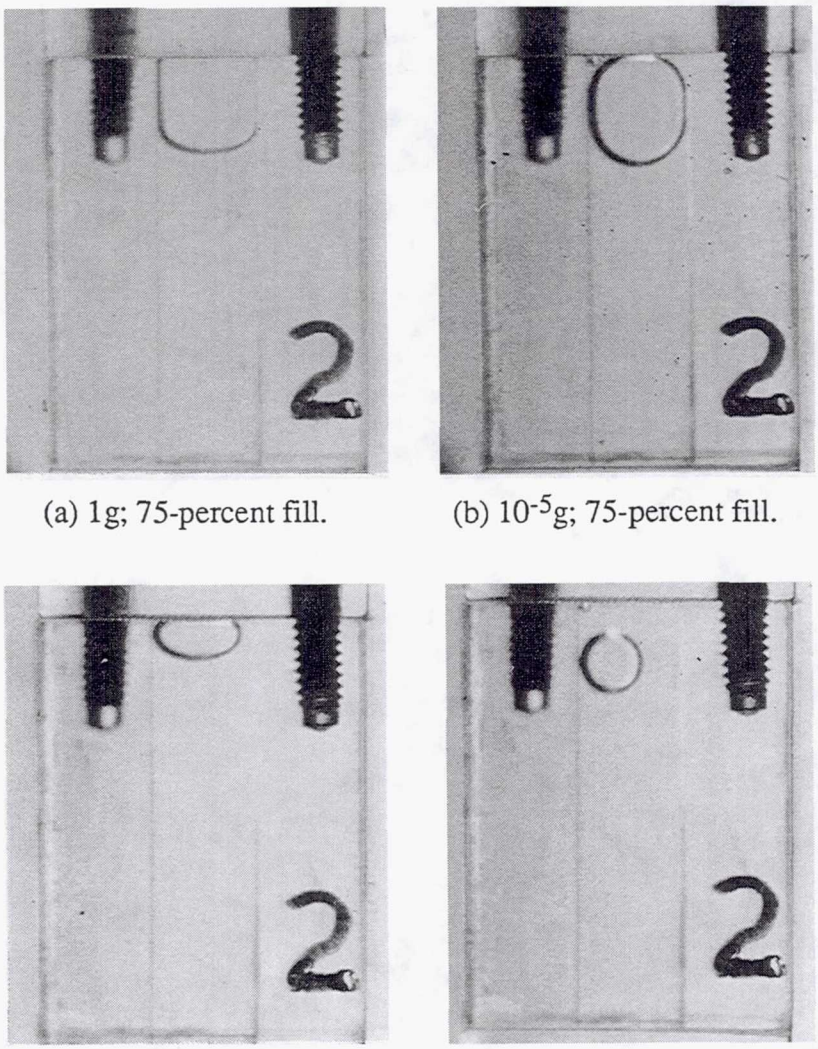

(a) 1g; 75-percent fill.

(b) 10^{-5}g; 75-percent fill.

(c) 1g; 90-percent fill.

(d) 10^{-5}g; 90-percent fill.

Figure 15.—Normal- and reduced-gravity interfacial surfaces from photographic data using silicone oil in rectangular Plexiglas container 2. Bo = 0.25 in 1g.

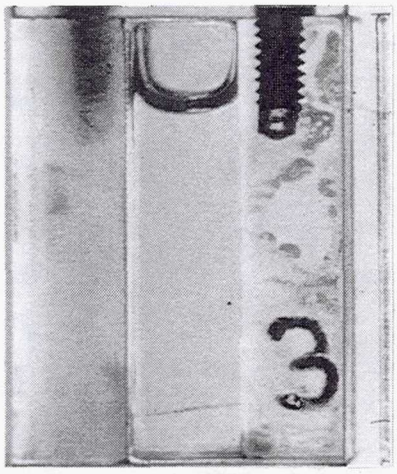

(a) 1g; 75-percent fill.

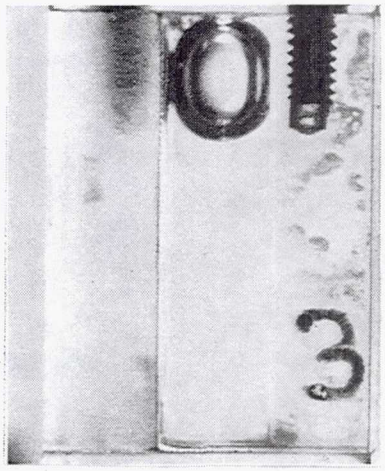

(b) 10^{-5}g; 75-percent fill.

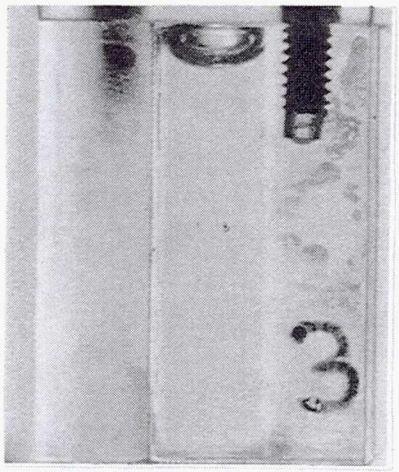

(c) 1g; 90-percent fill.

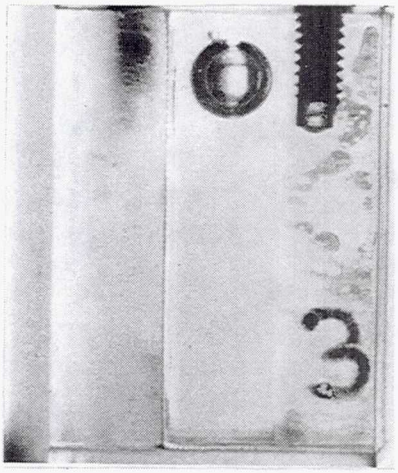

(d) 10^{-5}g; 90-percent fill.

Figure 16.—Normal- and reduced-gravity interfacial surfaces from photographic data using silicone oil in rectangular Plexiglas container 3. Bo = 4.0 in 1g.

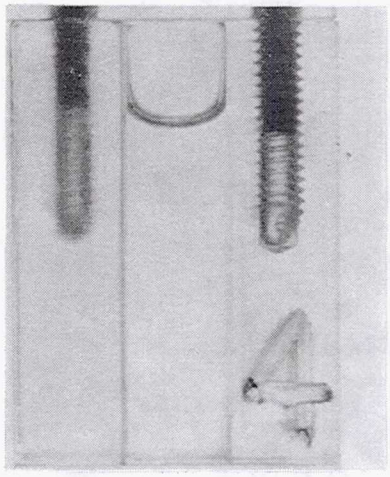

(a) 1g; 75-percent fill.

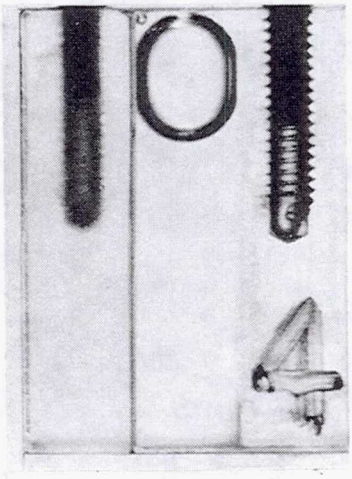

(b) 10^{-5}g; 75-percent fill.

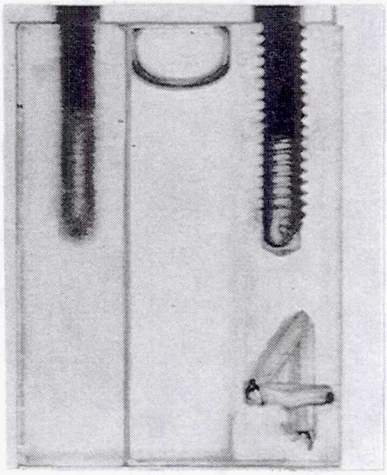

(c) 1g; 90-percent fill.

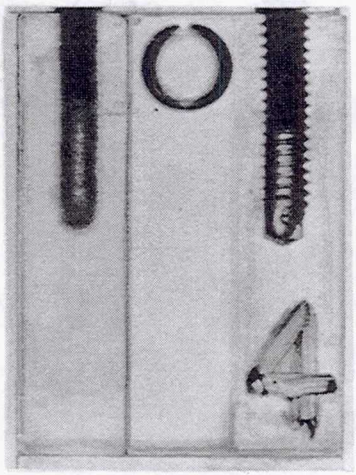

(d) 10^{-5}g; 90-percent fill.

Figure 17.—Normal- and reduced-gravity interfacial surfaces from photographic data using silicone oil in rectangular Plexiglas container 4. Bo = 1.0 in 1g.

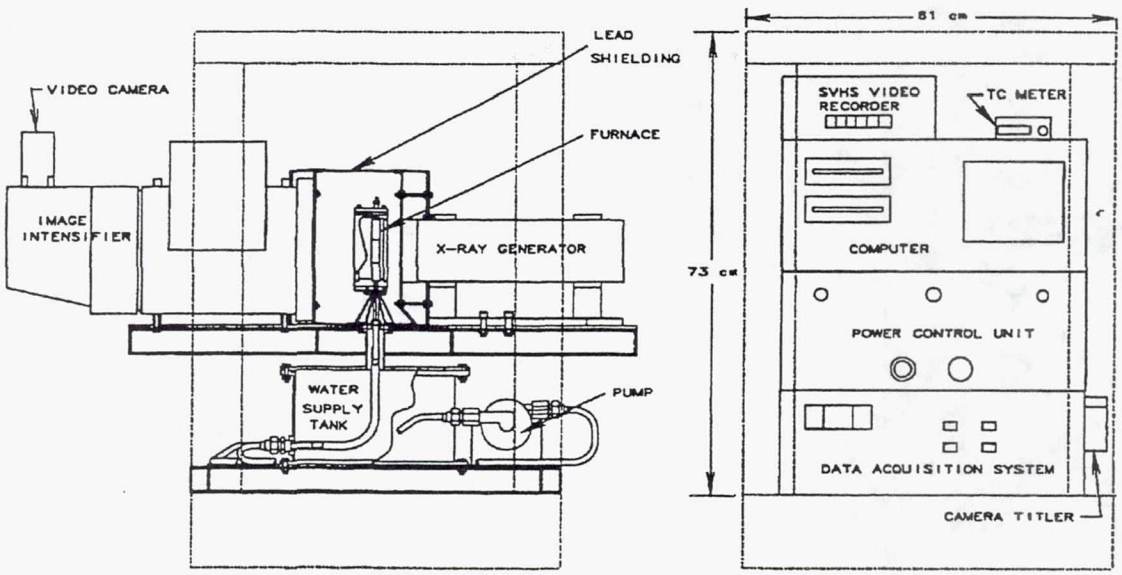

(a) Drawing of flight hardware.

(b) Photograph of Francis Chiaramonte with flight hardware (Learjet in background).

Figure 18.—Quench furnace with x-ray system for reduced-gravity experiments on NASA Lewis Learjet.

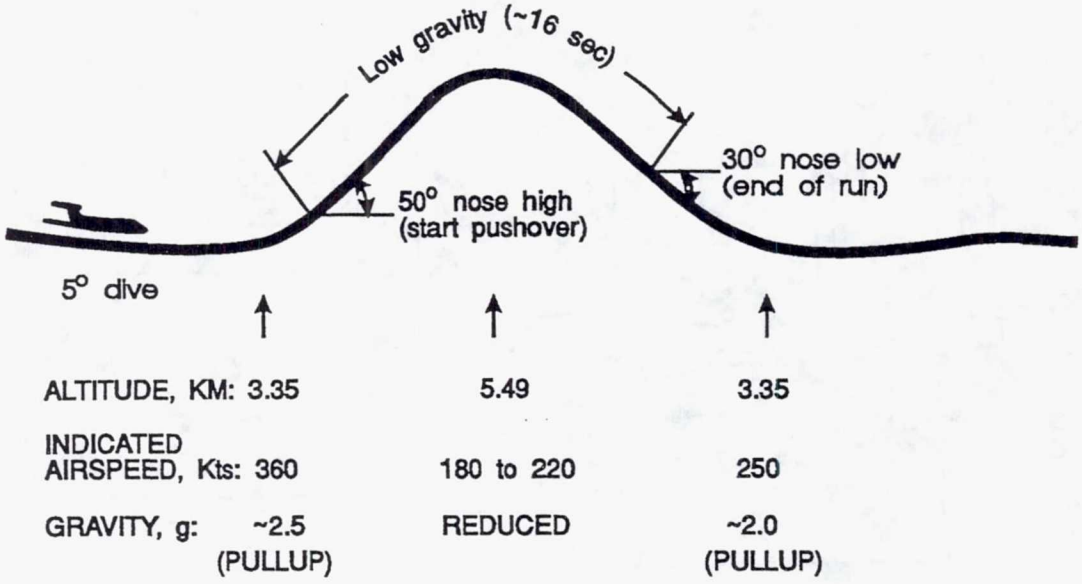

Figure 19.—Typical reduced-gravity trajectory (±0.02g).

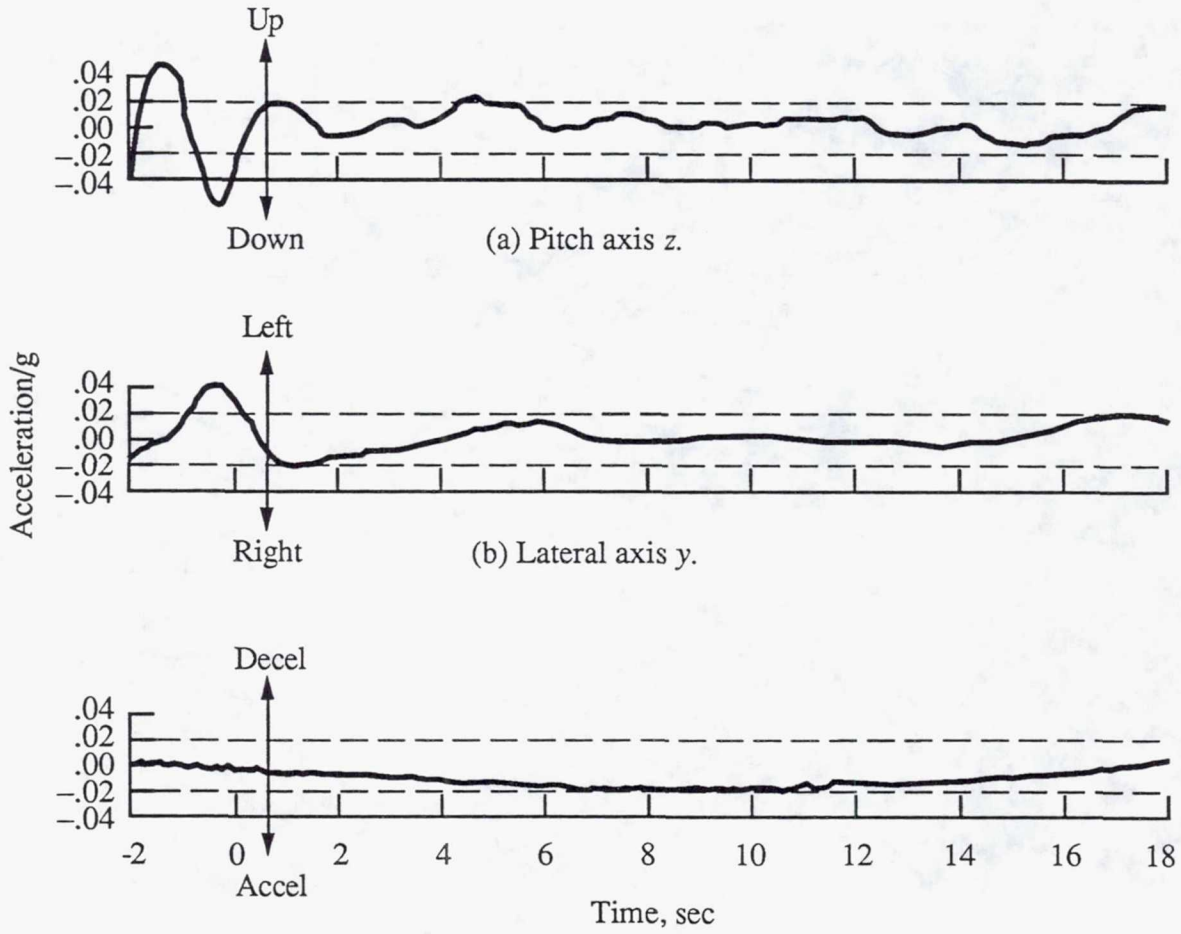

Figure 20.—NASA Lewis Learjet acceleration data during reduced-gravity trajectory in x, y, and z axes. Flight date: July 16, 1991.

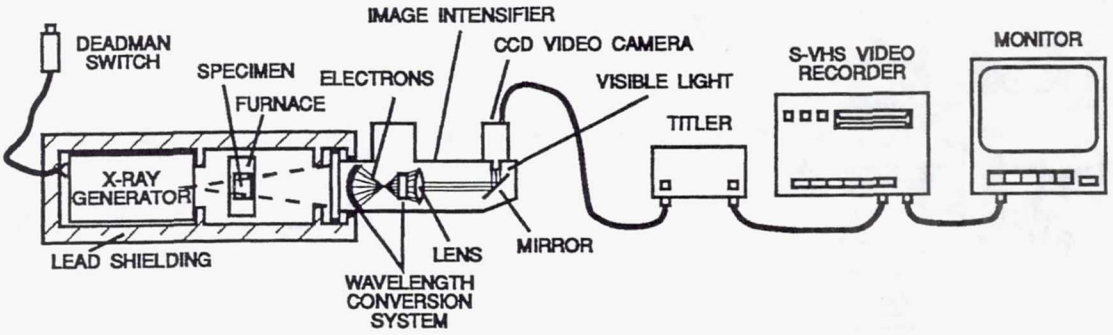

Figure 21.—Real-time radiographic viewing system.

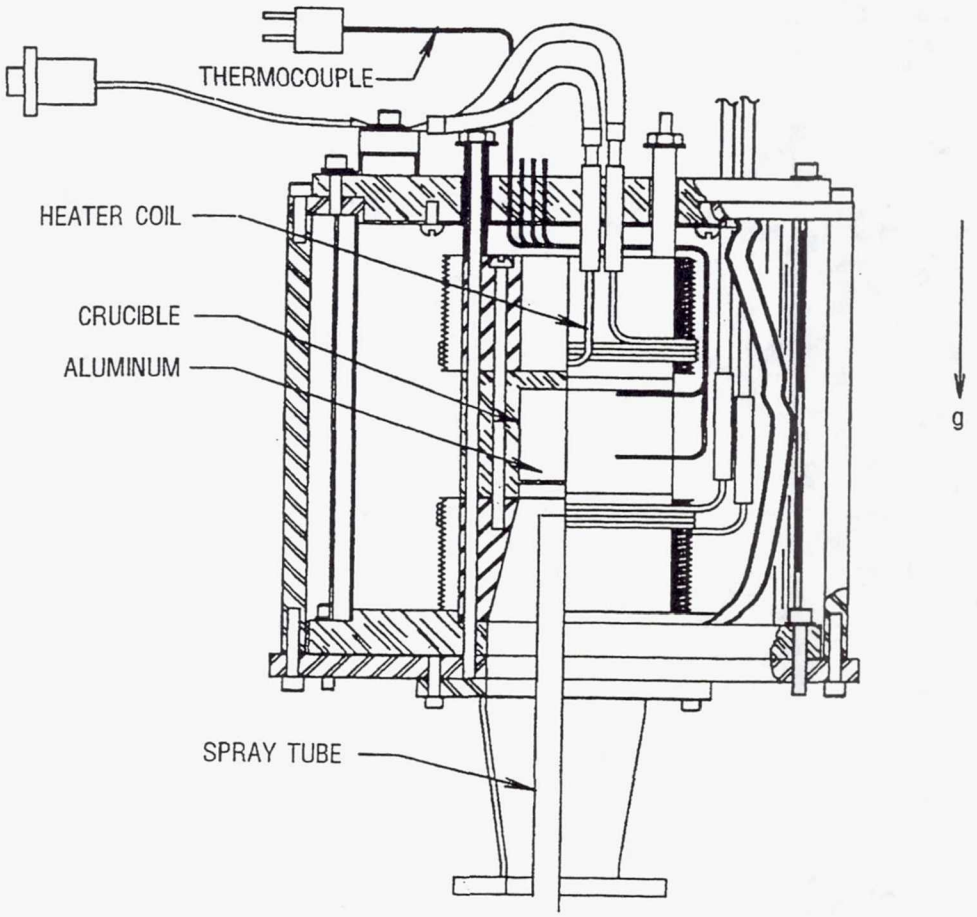

Figure 22.—End chill directional solidification furnace.

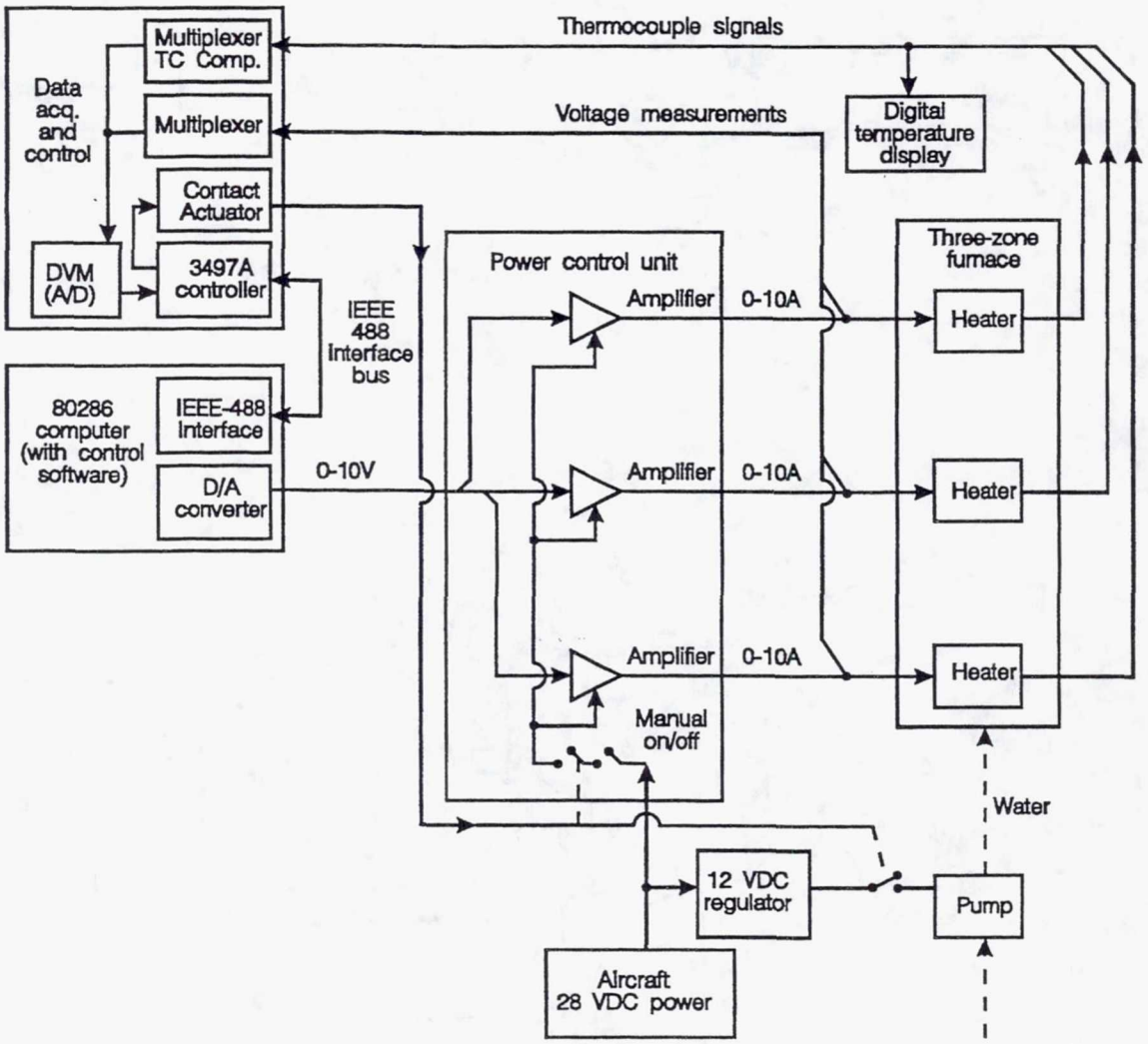

Figure 23.—Functional block diagram of furnace control system.

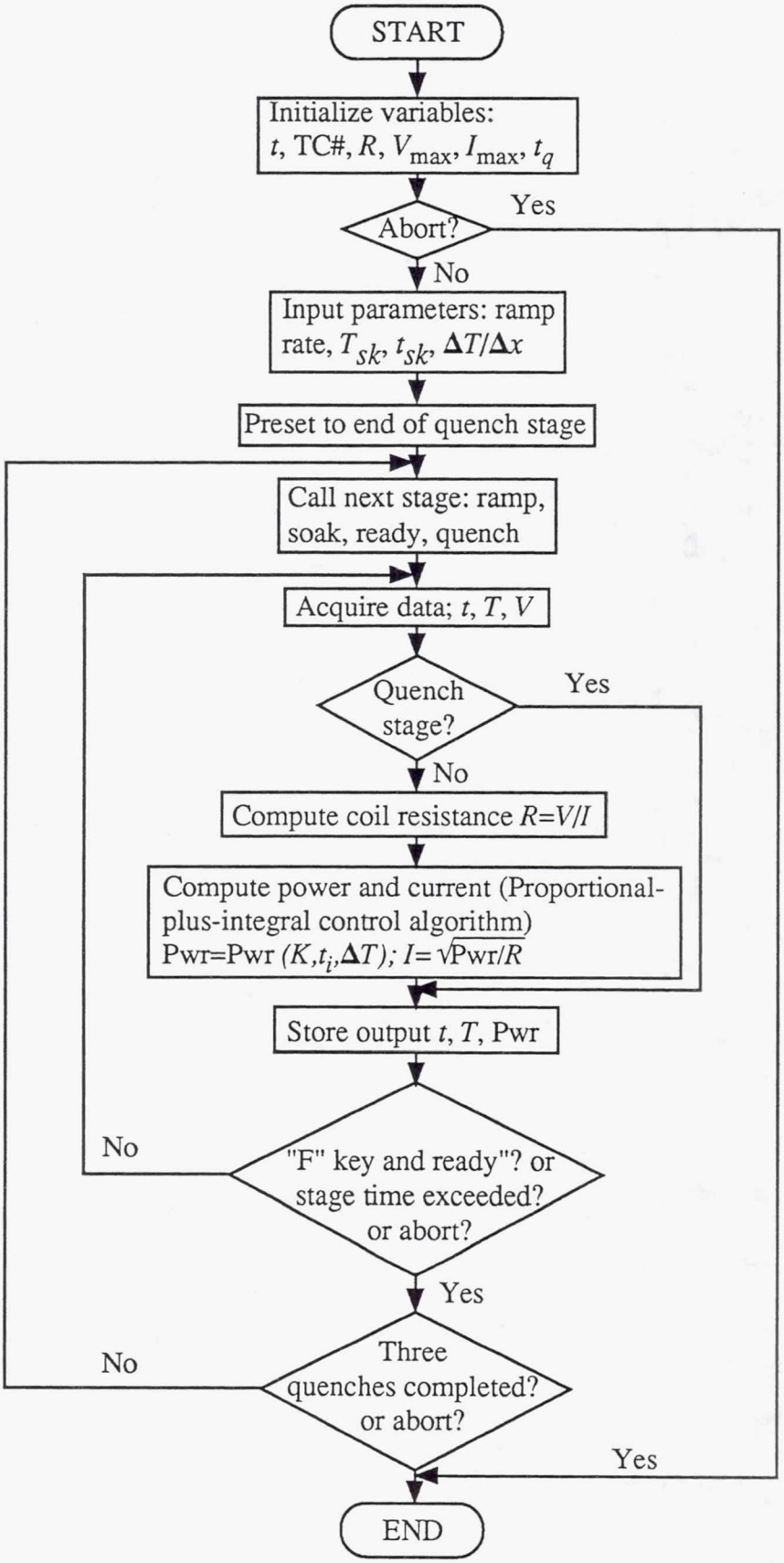

Figure 24.—Flowchart for experiment software.

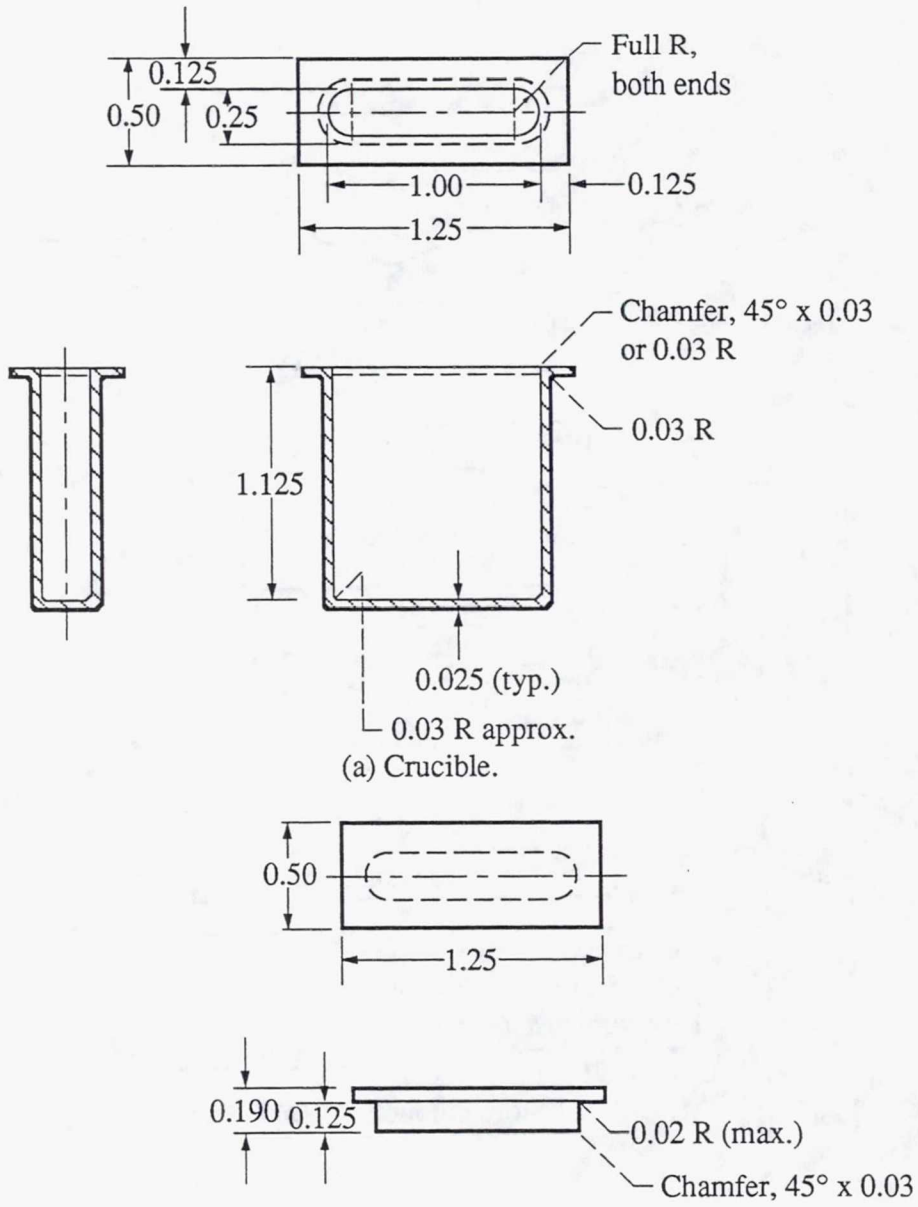

Figure 25.—Rounded pyrolytic boron nitride container.
(All dimensions are in inches.)

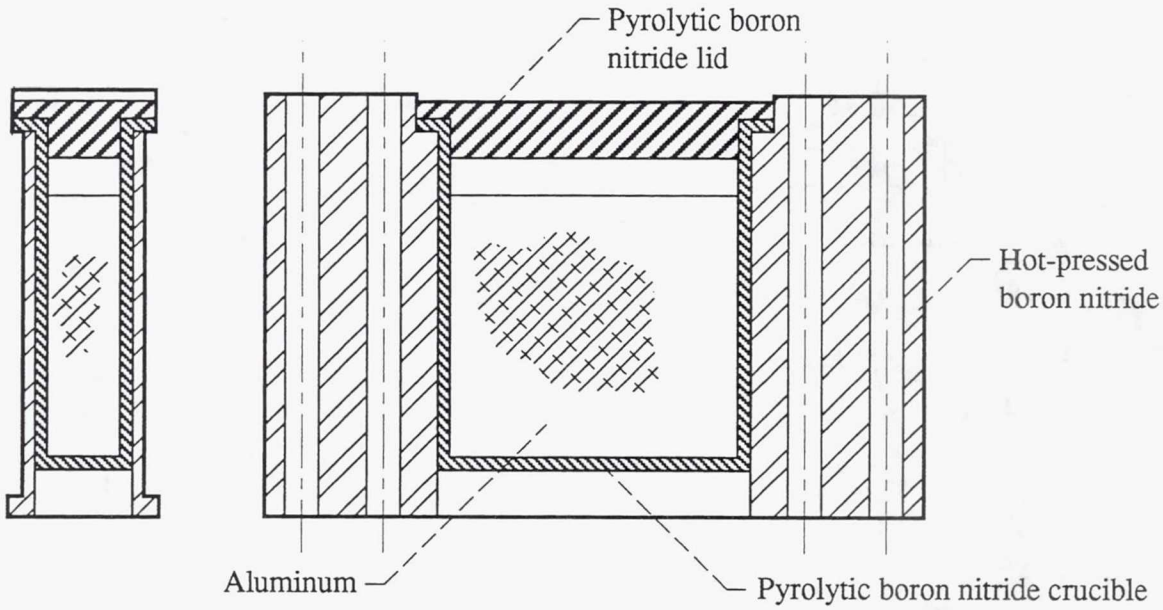

Figure 26.—Rounded pyrolytic boron nitride container assembly.

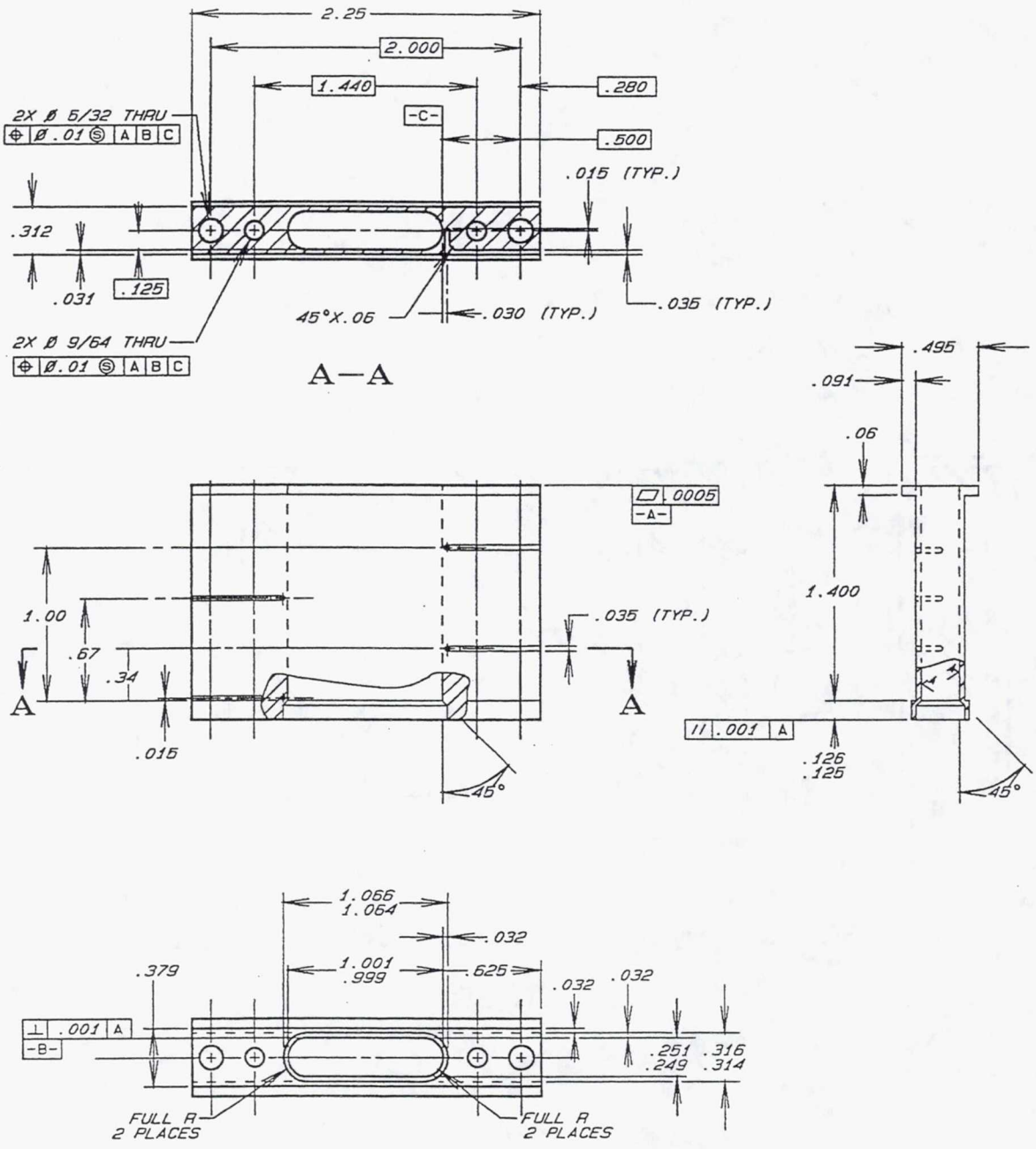

(a) Crucible.

Figure 27.—Titanium diboride(TiB_2) container. (All dimensions are in inches.)

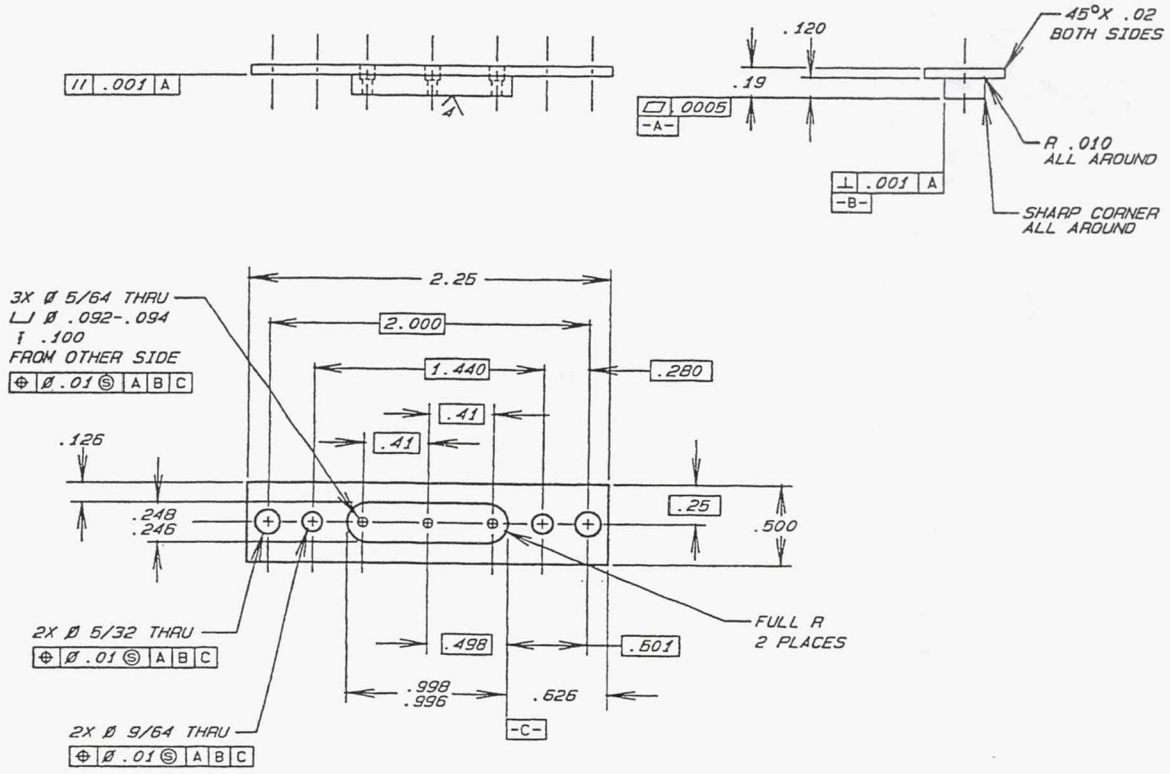

(b) Lid.

Figure 27.—Continued.

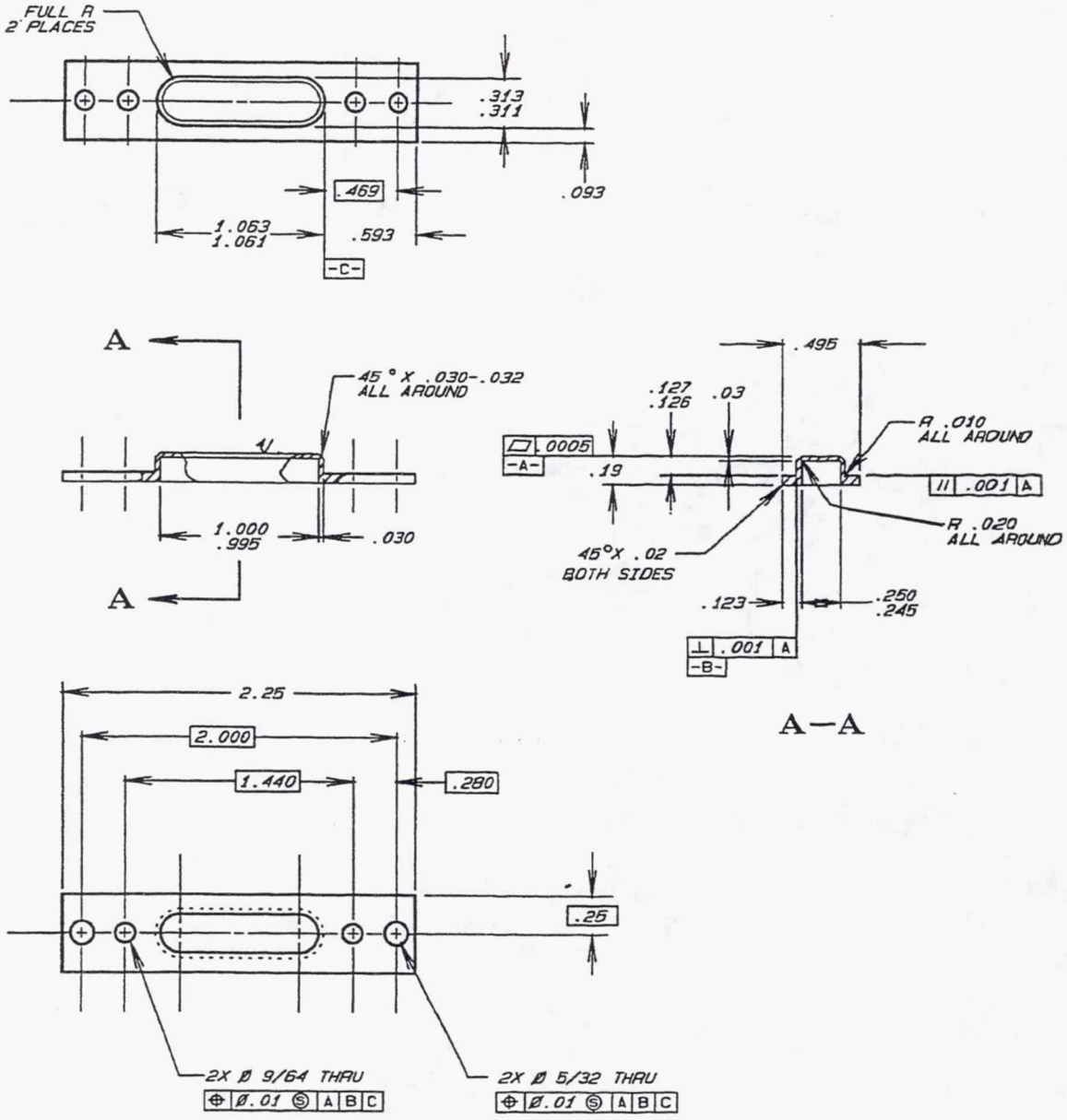

(c) Bottom adapter.

Figure 27.—Concluded.

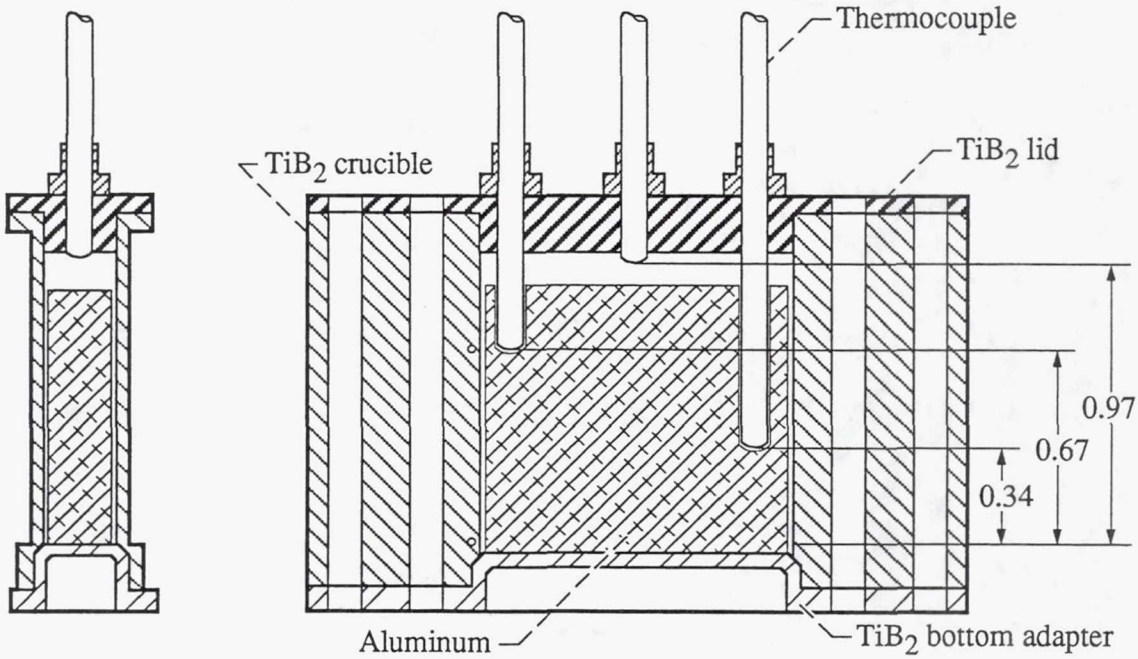

Figure 28.—Titanium diboride (TiB_2) container assembly. (All dimensions are in inches.)

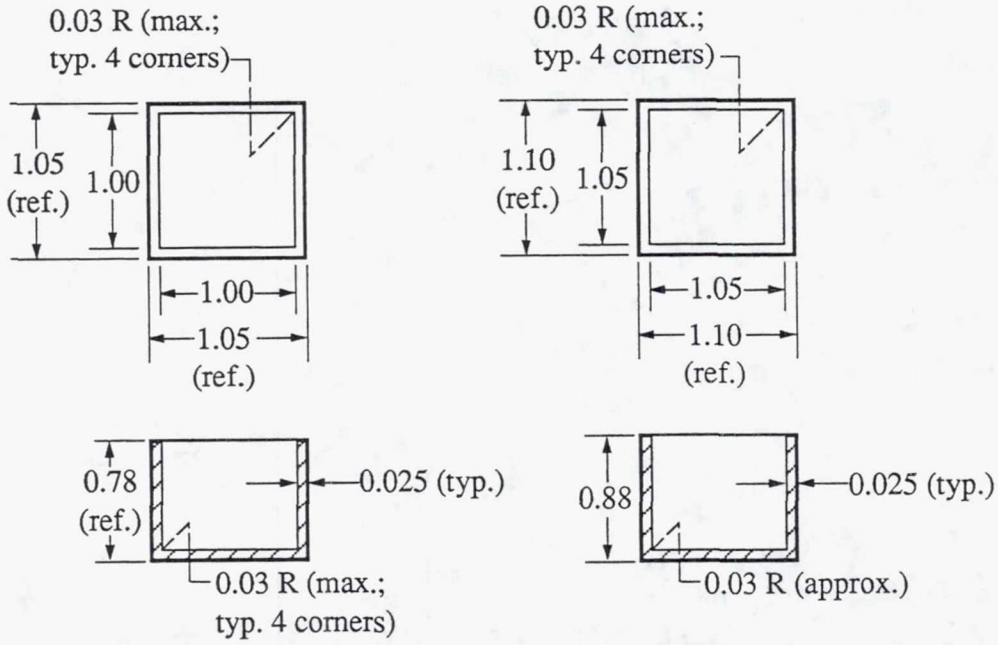

(a) Inner crucible.

(b) Outer crucible.

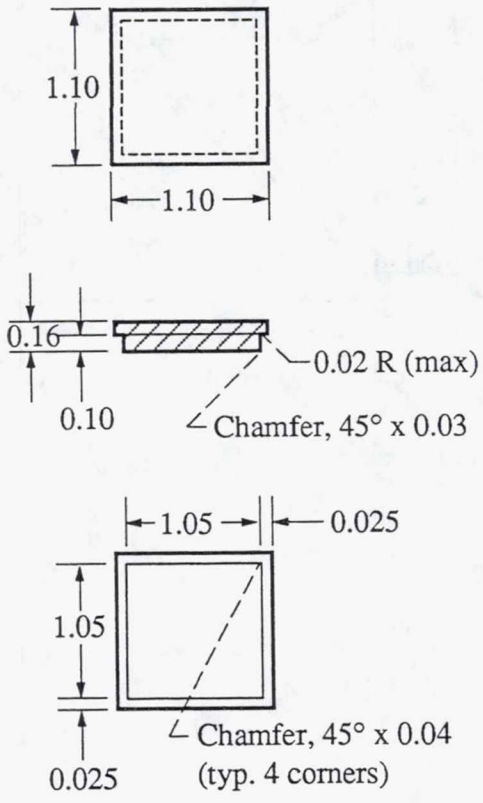

(c) Lid.

Figure 29.—Rectangular pyrolytic boron nitride container drawing. (All dimensions are in inches.)

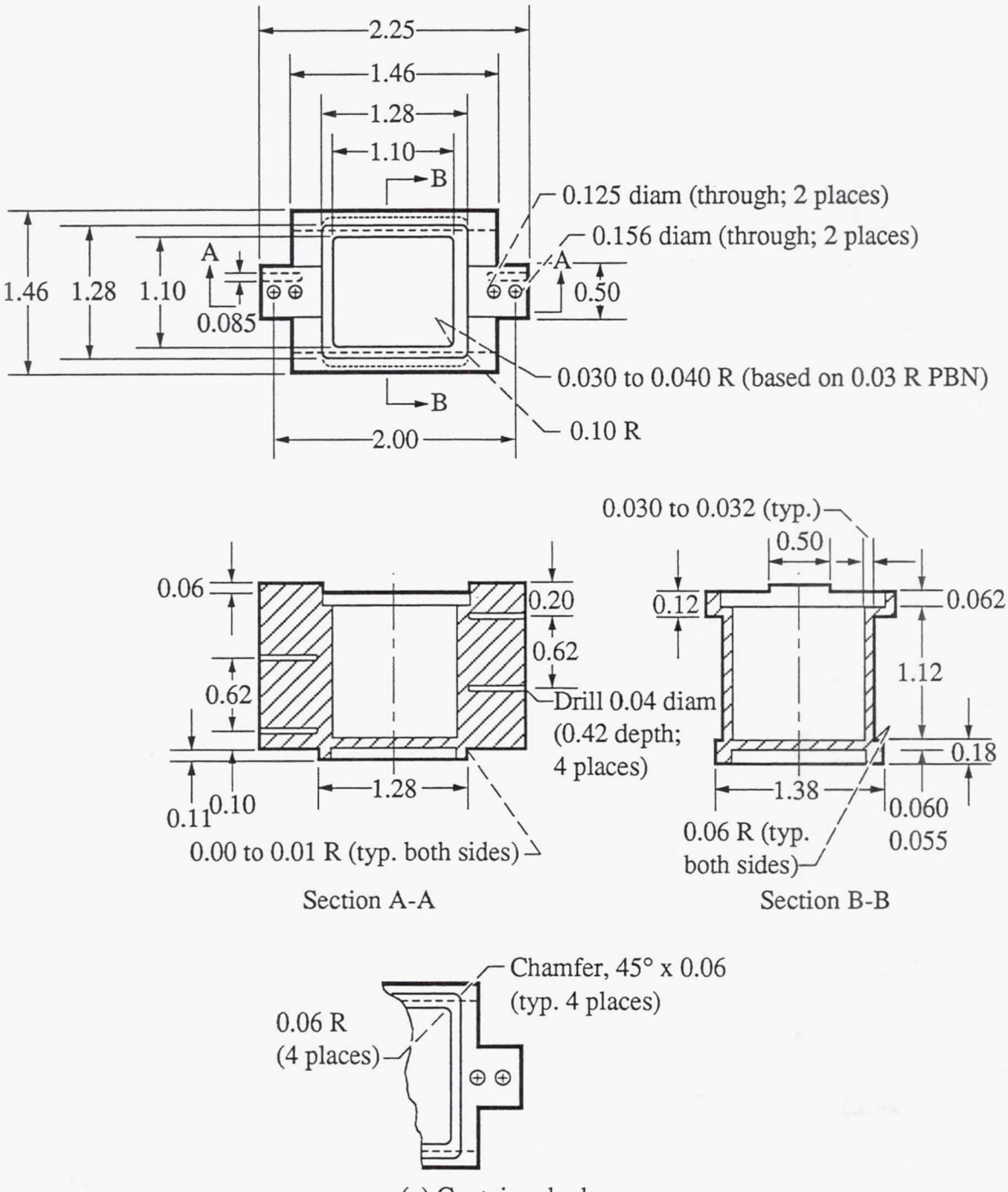

(a) Container body.

Figure 30.—Stainless steel container. (All dimensions are in inches.)

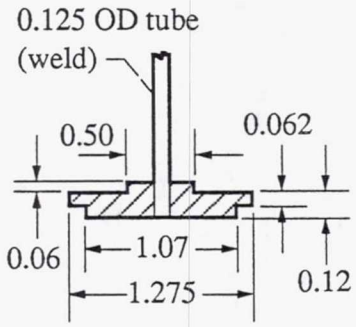

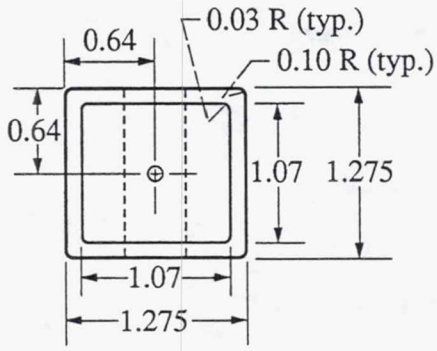

(b) Lid.

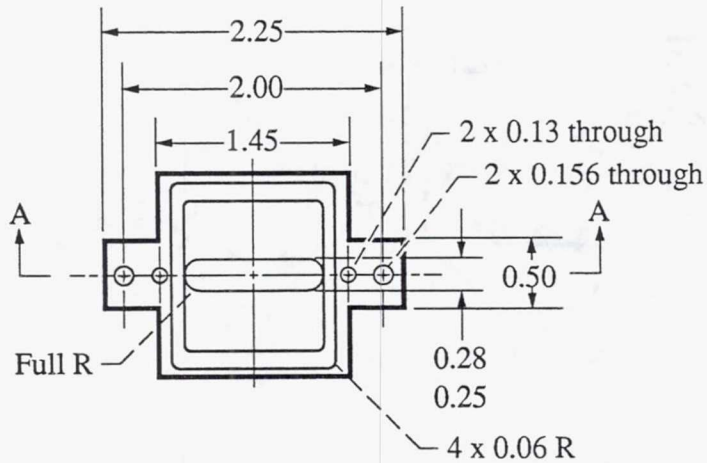

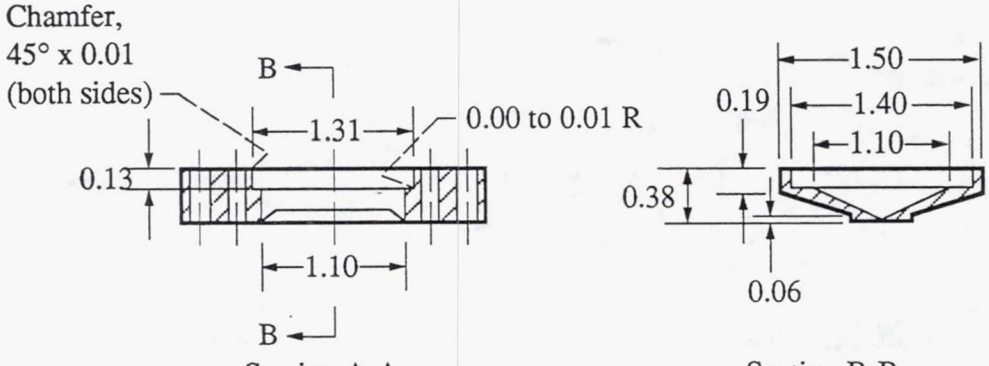

(c) Bottom adapter.

Figure 30.—Concluded.

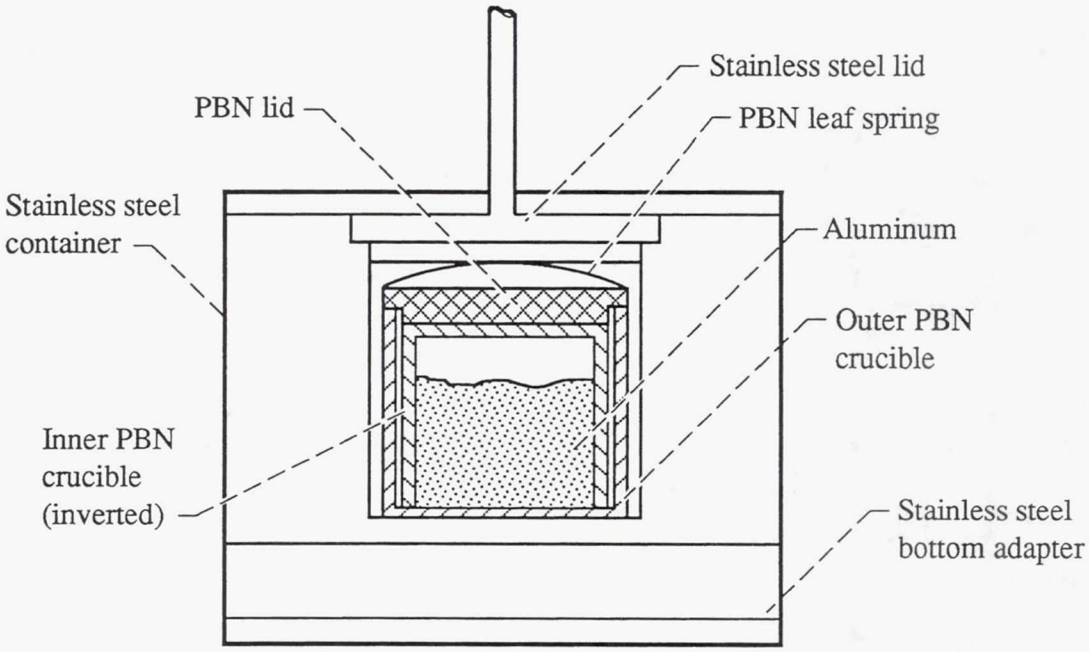

Figure 31.—Assembly drawing of aluminum-pyrolytic boron nitride-stainless steel system.

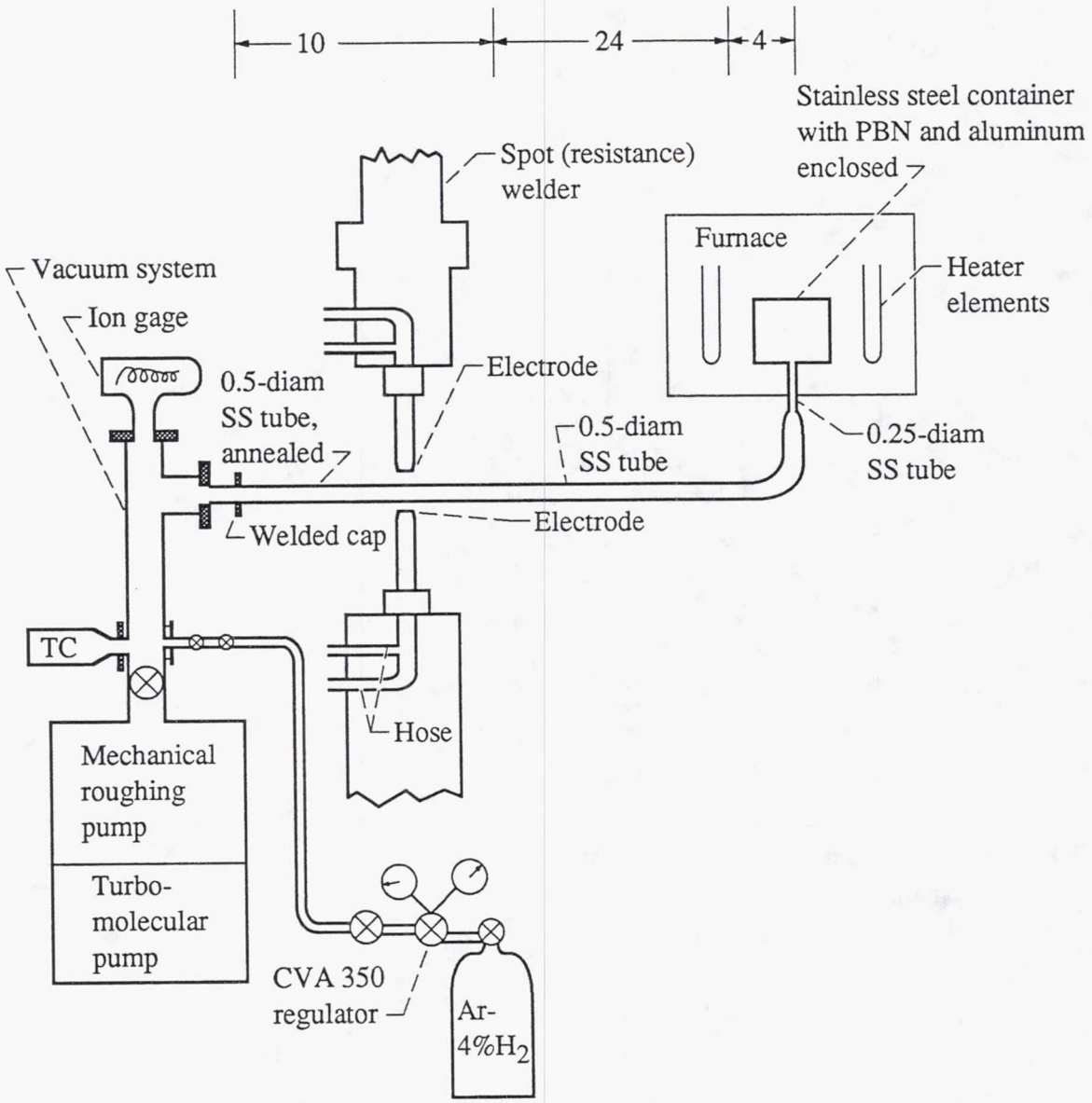

Figure 32.—Schematic drawing of stainless steel (SS) container preparation. (All dimensions are in inches.)

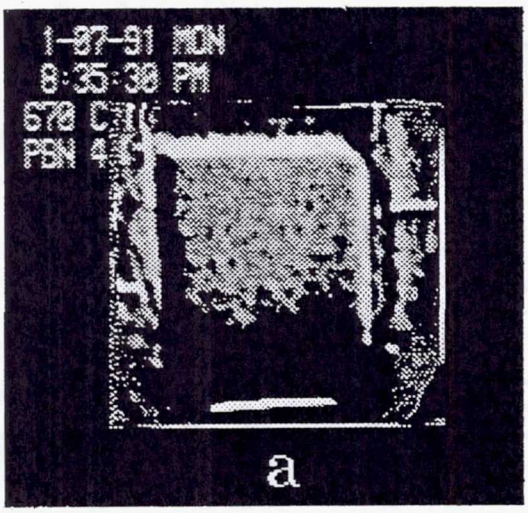

(a) 4 sec.

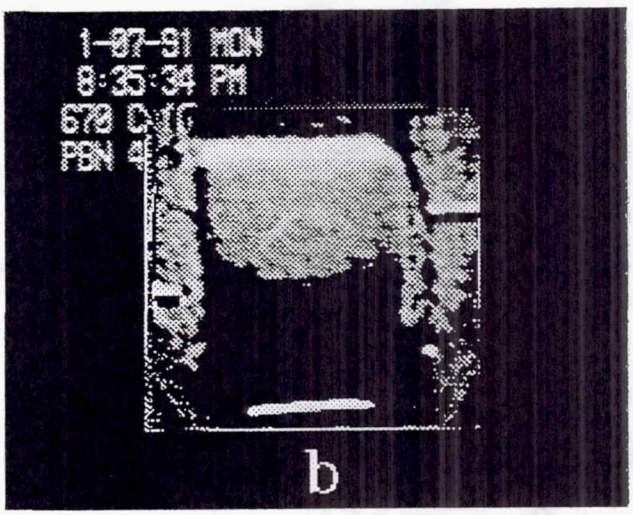

(b) 8 sec.

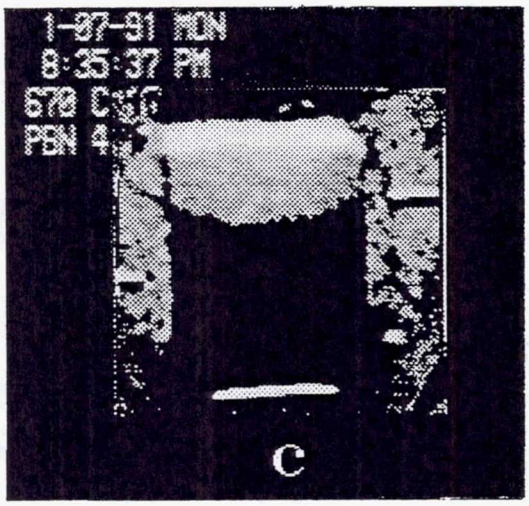

(c) 11 sec.

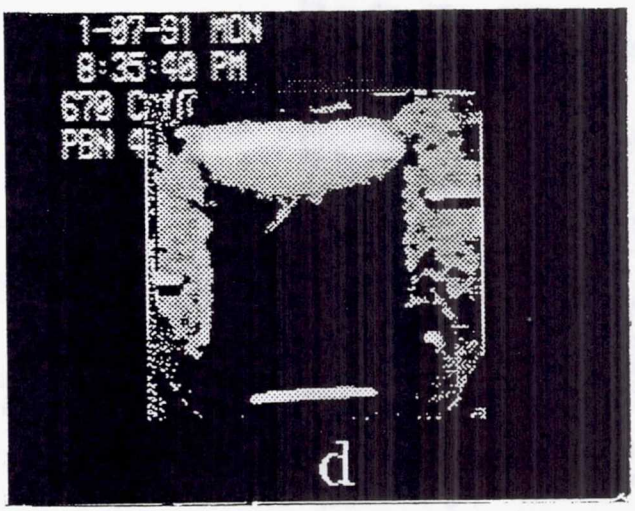

(d) 14 sec.

Figure 33.—Tracking solid/liquid interface of 2.4 cm x 2.4 cm x 0.6 cm aluminum sample in PBN container by image processing. (The dark region is solid, the light region is liquid. These images show the sample at various times after the quench was initiated.)

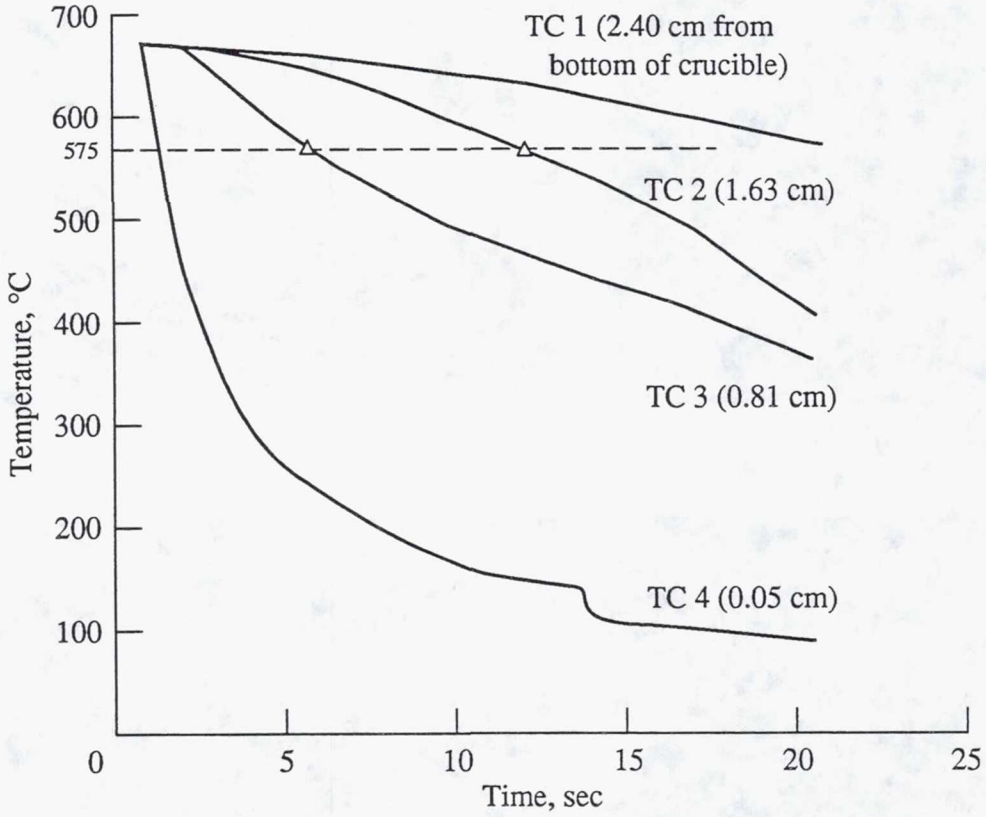

Figure 34.—PBN wall temperatures 0.23 cm from aluminum boundary at four vertical positions from bottom. (Triangles indicate solidification; test conducted on Jan. 7, 1991.)

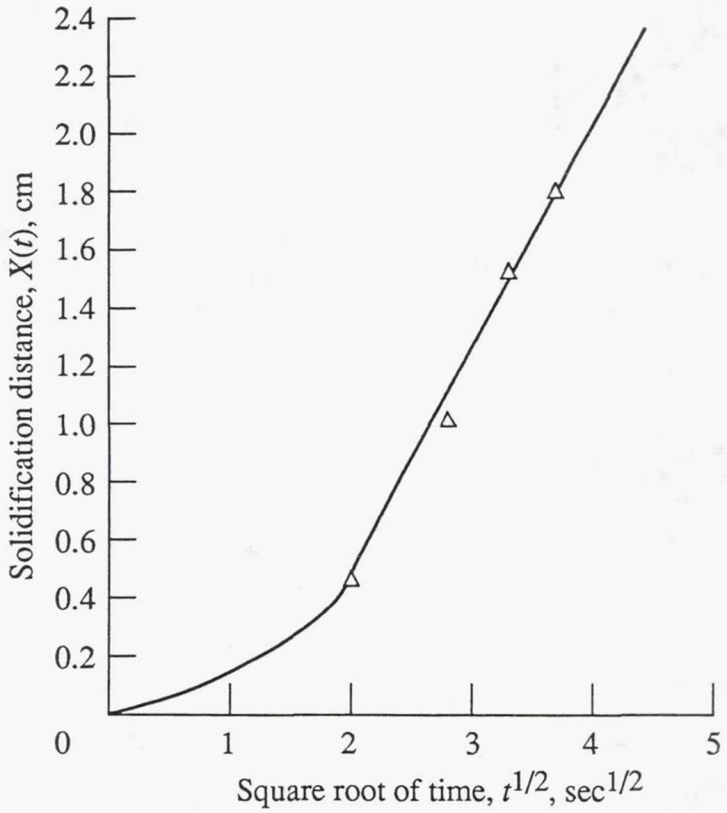

Figure 35—Directional solidification of pure aluminum in PBN crucible. (Test conducted on Jan. 7, 1991.)

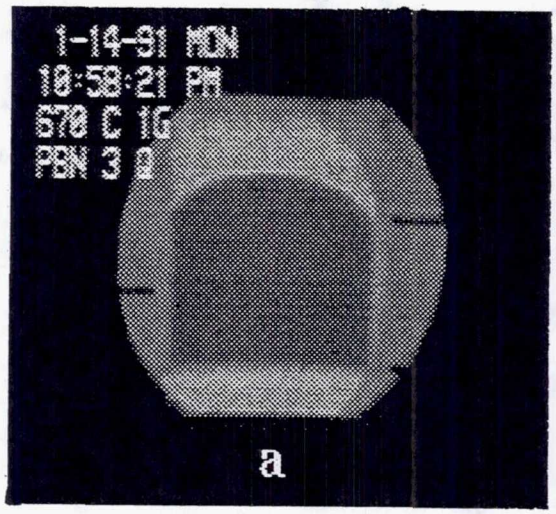

(a) Liquid; 1g; prior to quench.

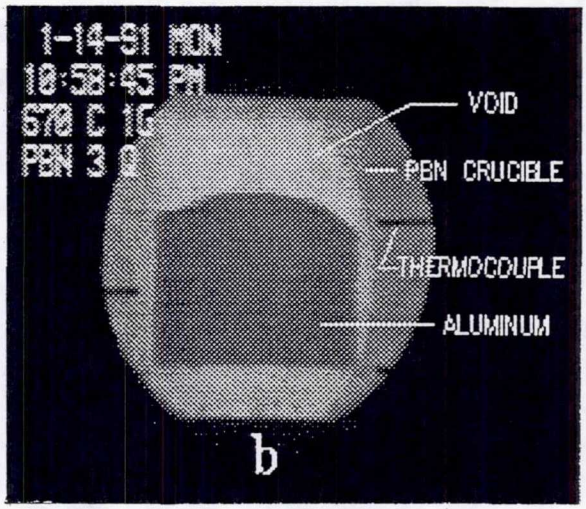

(b) Solid; 1g; just after quench.

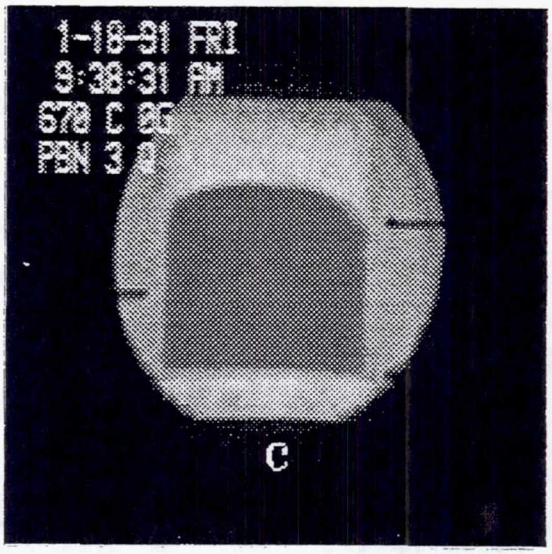

(c) Liquid; ±0.02g; prior to quench.

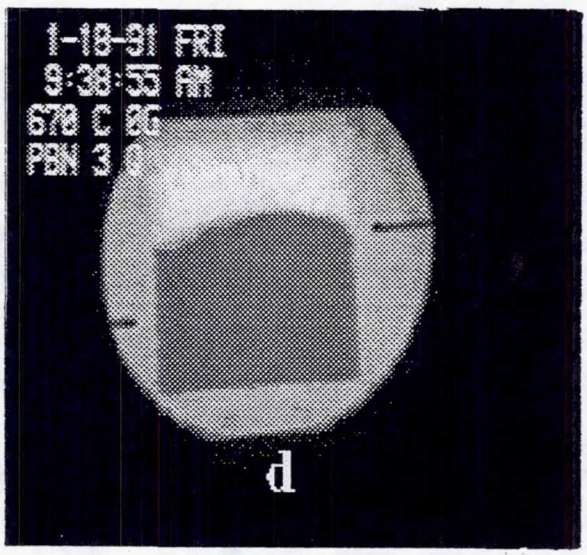

(d) Solid; ±0.02g; just after quench.

Figure 36.—Void formation during aluminum solidification in PBN container in normal and reduced gravity for 70-percent-liquid-fill, nonwetting case.

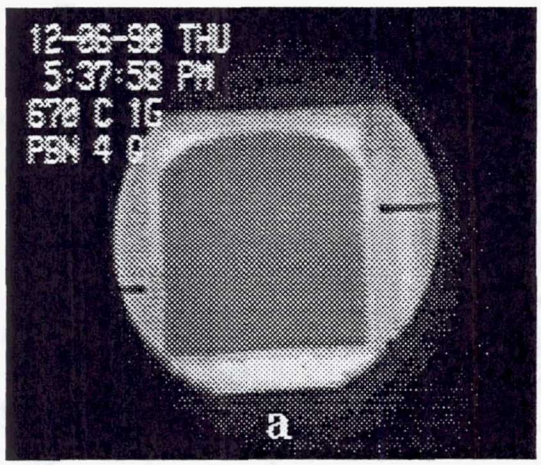

(a) Liquid; 1g; prior to quench.

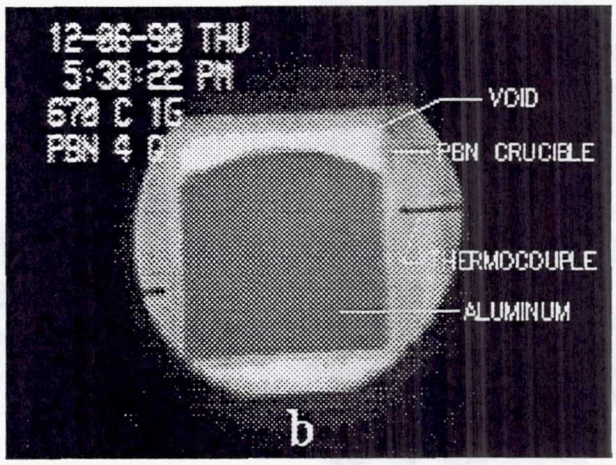

(b) Solid; 1g; just after quench.

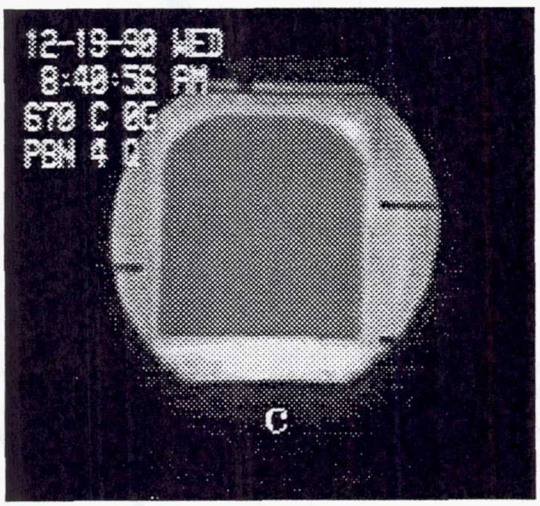

(c) Liquid; ±0.02g; prior to quench.

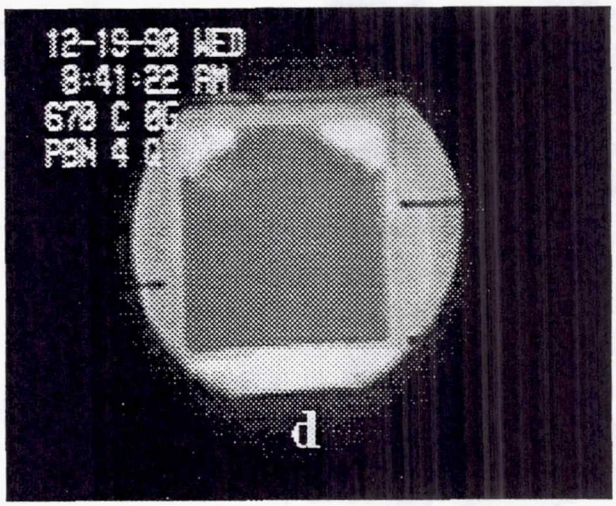

(d) Solid; ±0.02g; just after quench.

Figure 37.—Void formation during aluminum solidification in PBN container in normal and reduced gravity for 95-percent-liquid-fill, partial wetting case.

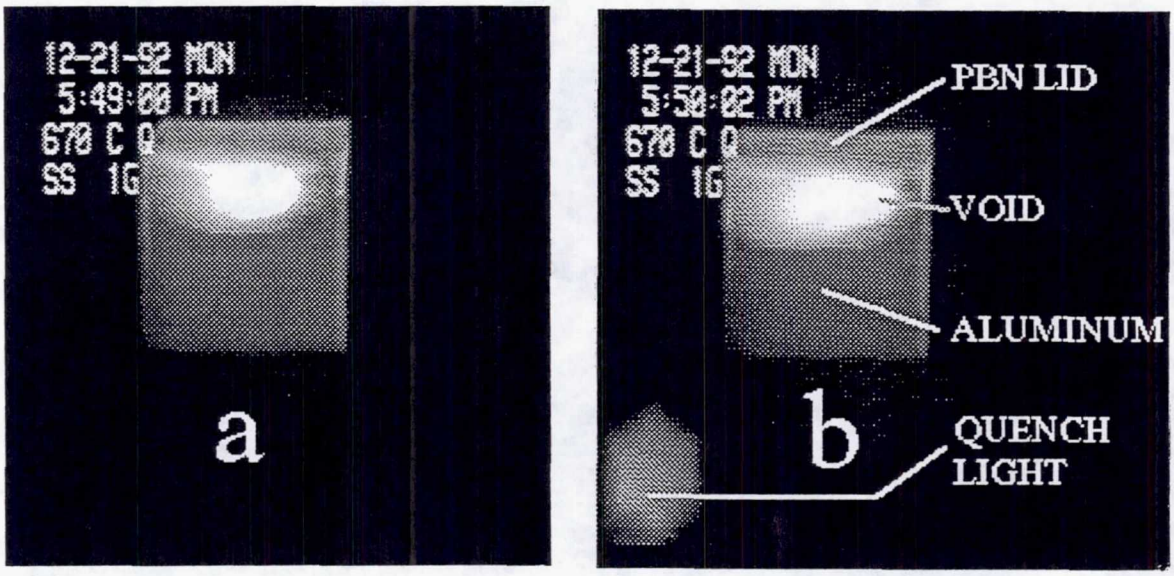

(a) Liquid; prior to quench.

(b) Solid; just after quench.

Figure 38.—Void formation during aluminum solidification in stainless steel system and at normal gravity for 66-percent-liquid-fill, wetting case.

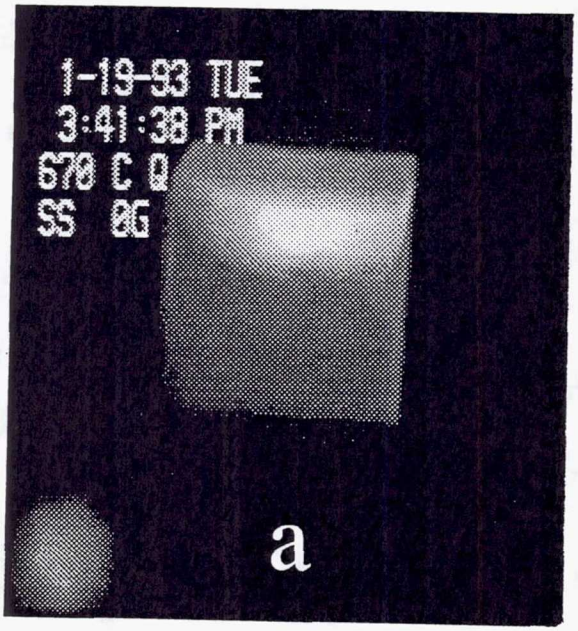

(a) Liquid; $2\frac{1}{2}$g; quench initiated.

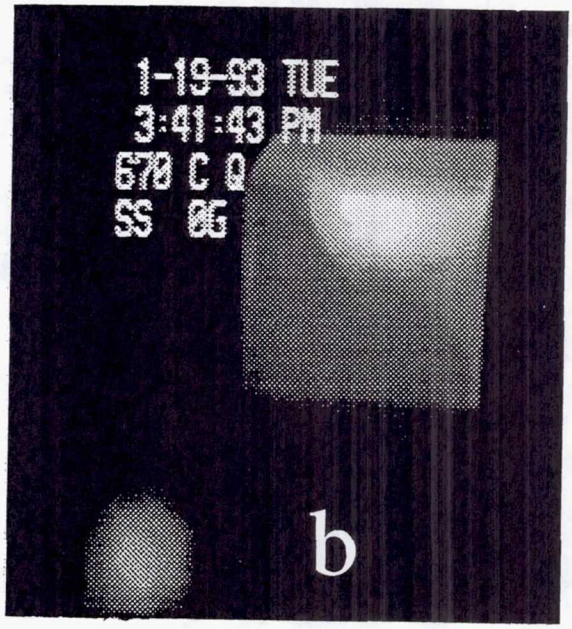

(b) Liquid; ±0.02g; quench in progress.

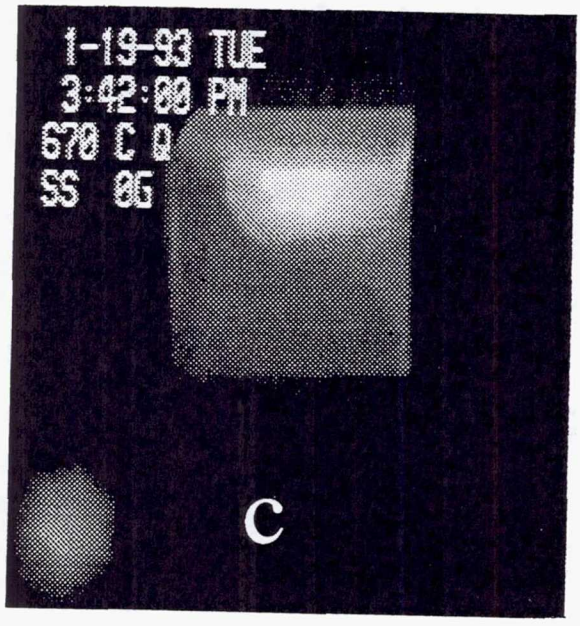

(c) Liquid; ±0.02g; quench in progress.

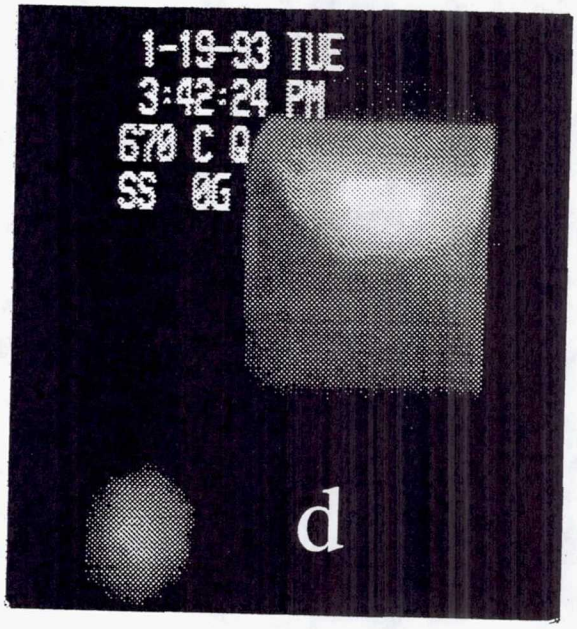

(d) Solid; 2g.

Figure 39.—Aluminum solidification with void formation in stainless steel system while experiment is flown through parabolic trajectory; partial wetting case.

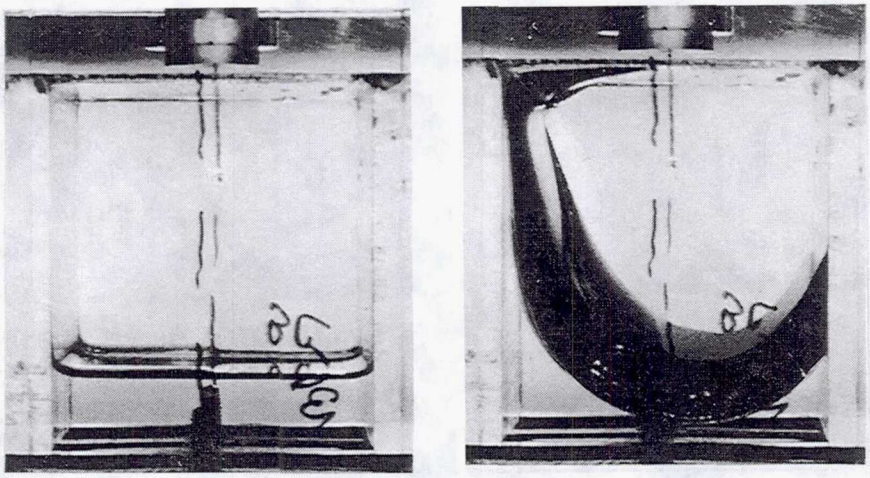

(a) Normal gravity. (b) Reduced gravity.

Figure 40.—Liquid/vapor interface configurations at normal and reduced gravity levels with surface coating applied to right half of container. (Silicone oil in a cube-shaped Plexiglas container was tested with $\theta = 0°$ on the left side and $\theta = 59°$ on the right side.) From reference 47.

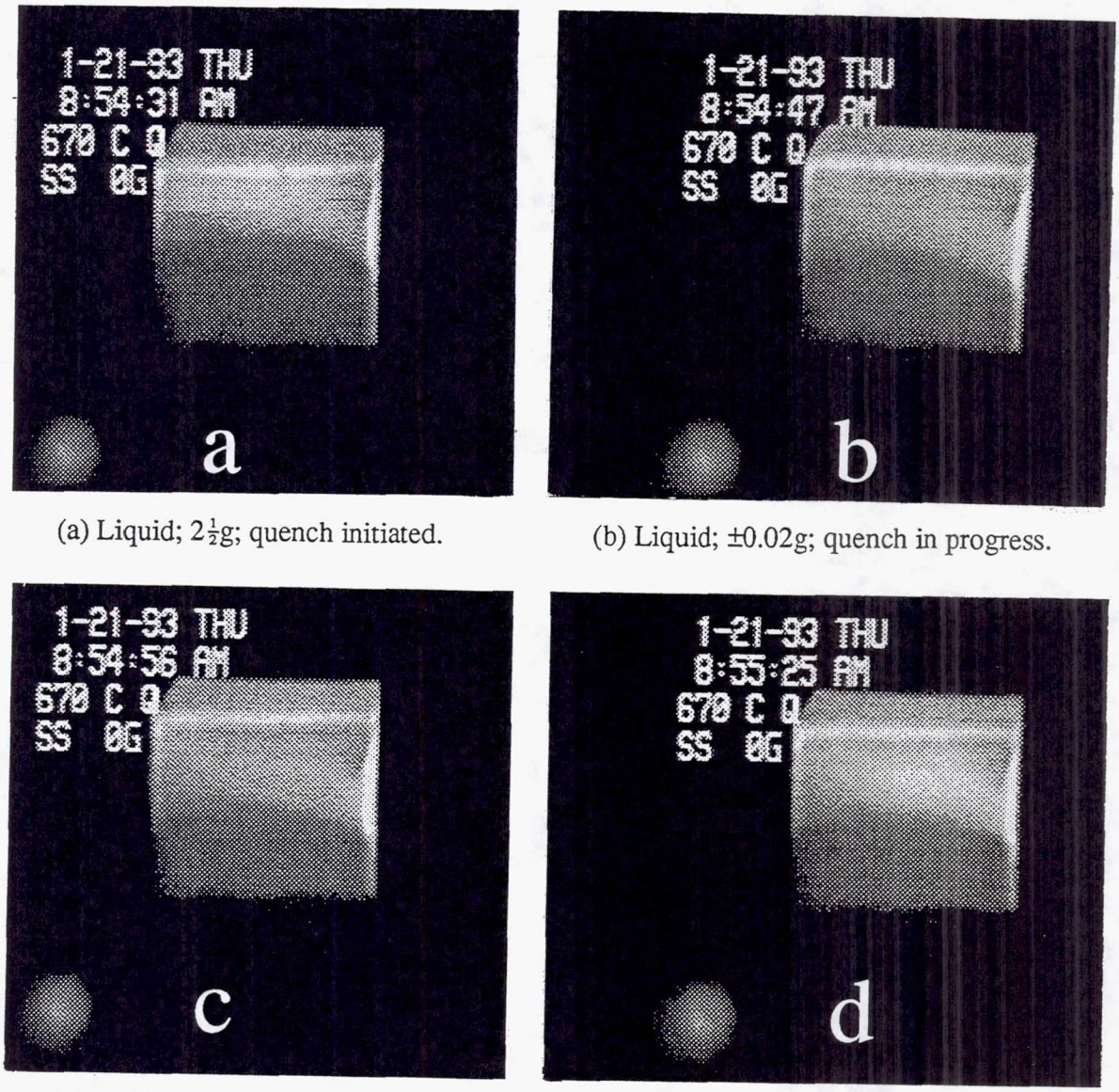

(a) Liquid; $2\frac{1}{2}$g; quench initiated.

(b) Liquid; ±0.02g; quench in progress.

(c) Liquid; ±0.02g; quench in progress.

(d) Solid; 2g.

Figure 41.—Aluminum solidification with void formation in stainless steel system while experiment is flown through parabolic trajectory; nonwetting case.

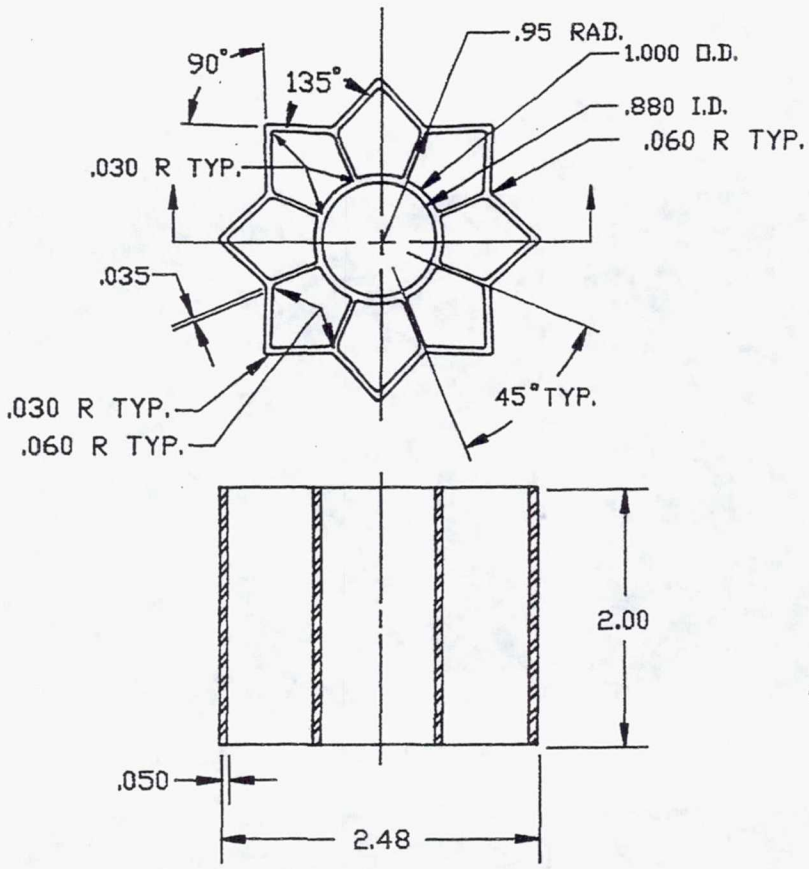

(a) Container body.

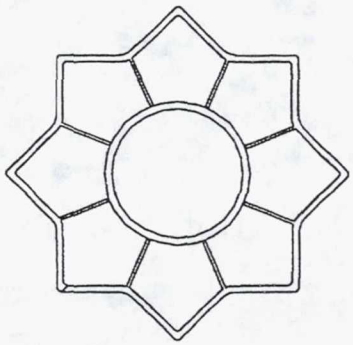

(c) Plan view.

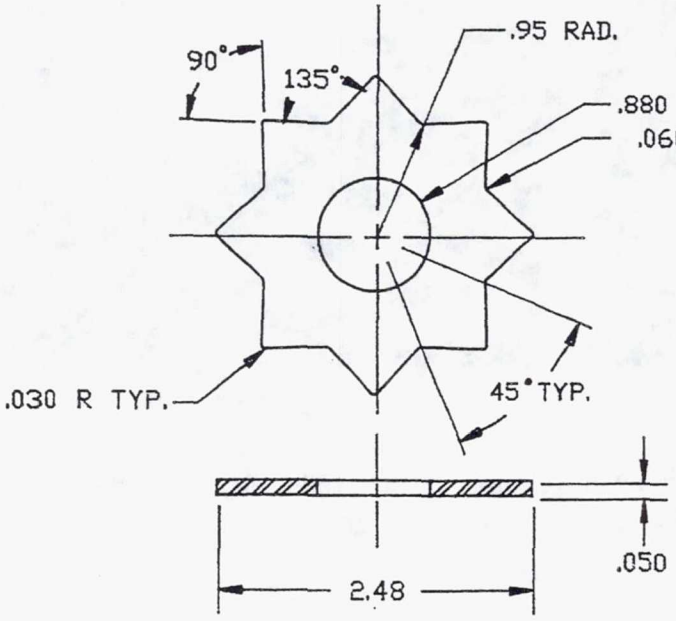

(b) End cap.

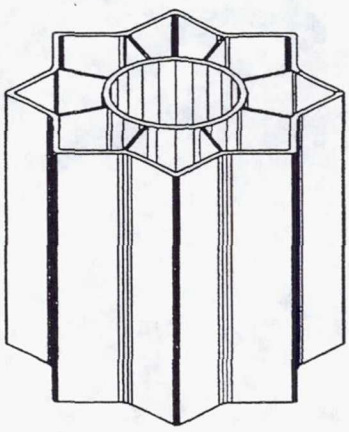

(d) Isometric projection.

Figure 42.—Star-shaped toroid canister for heat storage. (All dimensions are in inches.)

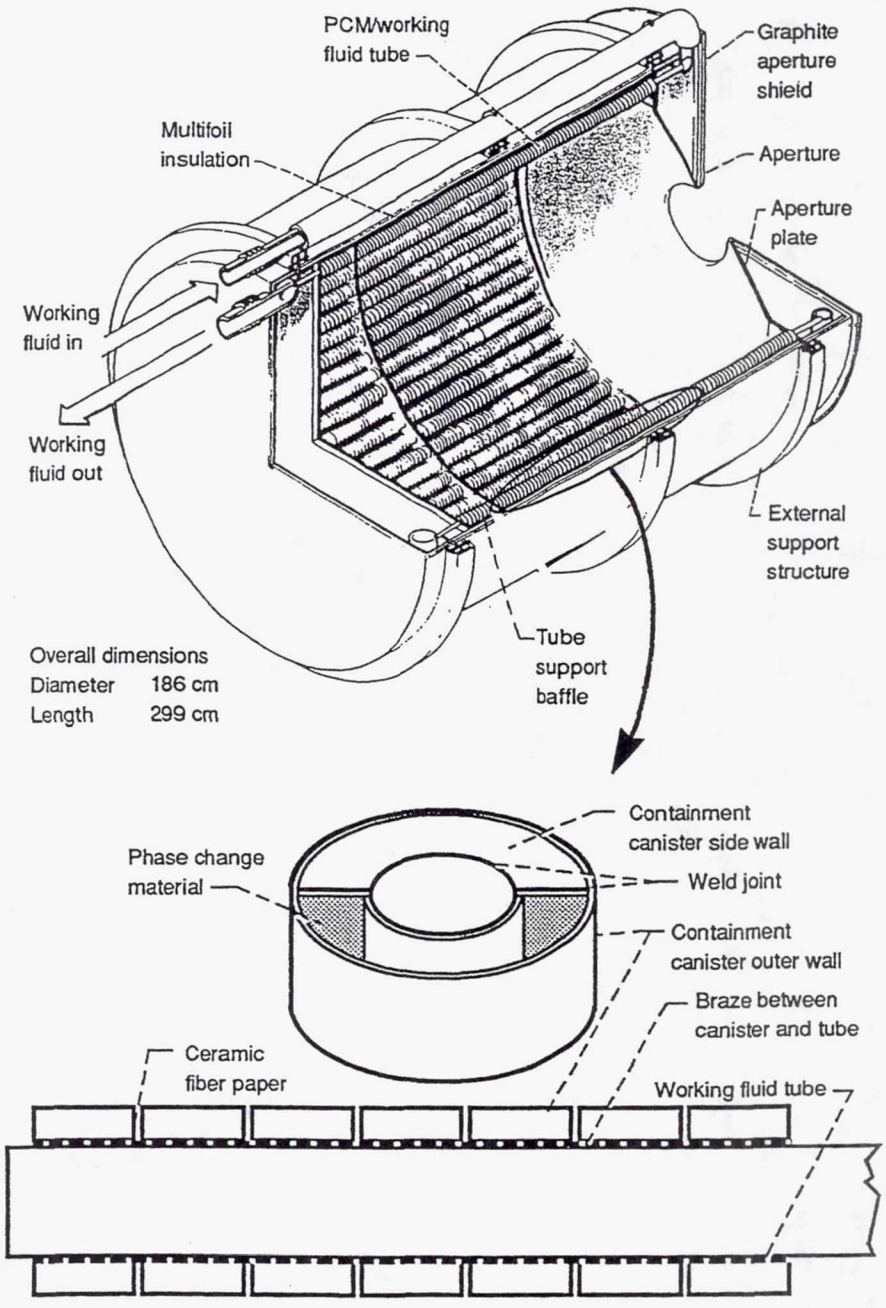

Figure 43.—Proposed Space Station *Freedom* heat receiver concept. From reference 1.

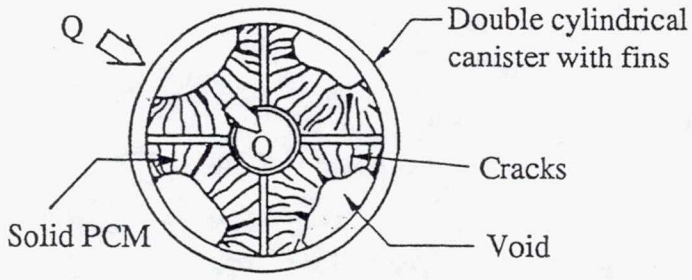

Figure 44.—Possible reduced-gravity void distribution in cylindrical container with fins. From reference 50.

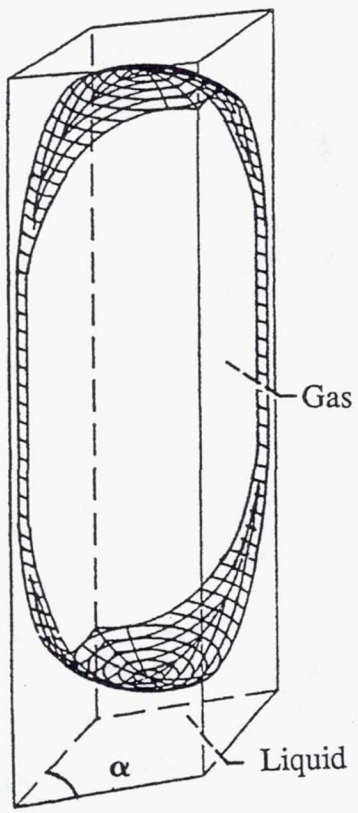

$\alpha/2 + \theta < 90°$

$\alpha/2 < \theta$

Figure 45.—Reduced-gravity, free-surface shape in rhombic prism. From reference 31.

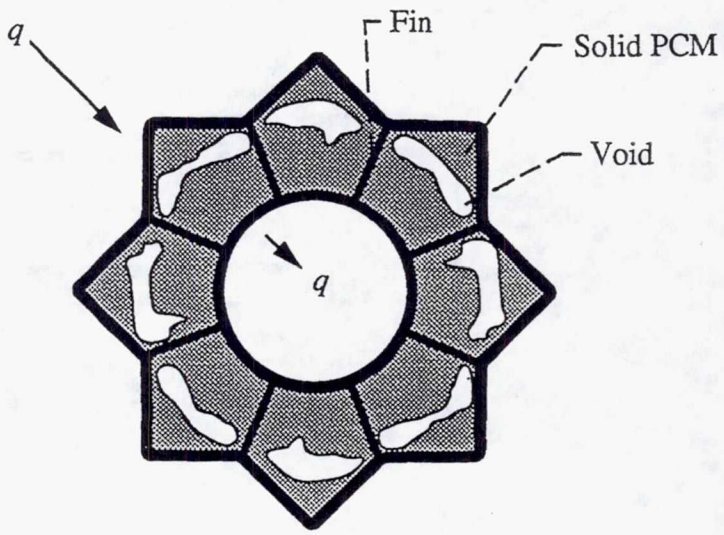

Figure 46.—Star-shaped toroid canister with anticipated void formation in reduced gravity.

REPORT DOCUMENTATION PAGE

Form Approved
OMB No. 0704-0188

1. AGENCY USE ONLY (*Leave blank*)	2. REPORT DATE	3. REPORT TYPE AND DATES COVERED
	October 1993	Technical Memorandum

4. TITLE AND SUBTITLE

Experimental Study of Void Formation During Aluminum Solidification in Reduced Gravity

5. FUNDING NUMBERS

WU-674-24-05

6. AUTHOR(S)

Francis Paul Chiaramonte III

7. PERFORMING ORGANIZATION NAME(S) AND ADDRESS(ES)

National Aeronautics and Space Administration
Lewis Research Center
Cleveland, Ohio 44135-3191

8. PERFORMING ORGANIZATION REPORT NUMBER

E-7520-1

9. SPONSORING/MONITORING AGENCY NAME(S) AND ADDRESS(ES)

National Aeronautics and Space Administration
Washington, D.C. 20546-0001

10. SPONSORING/MONITORING AGENCY REPORT NUMBER

NASA TM-106190

11. SUPPLEMENTARY NOTES

This report was submitted as a dissertation in partial fulfillment of the requirements for Doctor of Philosophy in Engineering Science to the University of Toledo, Toledo, Ohio, in June 1993. Responsible person, Francis Paul Chiaramonte III, (216) 433-8040.

12a. DISTRIBUTION/AVAILABILITY STATEMENT

Unclassified - Unlimited
Subject Categories 26 and 34

12b. DISTRIBUTION CODE

13. ABSTRACT ***(Maximum 200 words)***

Void formation due to volumetric shrinkage and liquid/vapor reorientation during aluminum solidification was observed in real time by using a radiographic viewing system in normal and reduced gravity. An end-chill directional solidification furnace with water quench was designed and constructed to solidify aluminum samples during the approximately 16 sec of reduced gravity (±0.02g) achieved by flying an aircraft through a parabolic trajectory. In the first series of tests the aluminum was contained in a vacuum-sealed, pyrolytic boron nitride crucible. An ullage space was present during each test. Void formation was recorded for two cases: a nonwetting system, and a wetting system where wetting occurred between the aluminum and the crucible lid. The void formation in the nonwetting case was similar in normal and reduced gravity, with a single vapor cavity forming at the top of the crucible. In the wetting case during reduced gravity surface tension caused two voids to form in the top corners of the crucible, but during normal gravity only one large void formed across the top. In the second series of tests the aluminum was contained in a pyrolytic boron nitride crucible that was placed in a stainless steel container and sealed in an environment of argon plus 4 percent hydrogen. An ullage space was present during each test. Void formation was recorded for two cases: a nonwetting system, and a wetting system where wetting occurred between the aluminum and one side wall and the lid. The void formation in the nonwetting case was similar in normal and reduced gravity, with a single vapor cavity forming at the top of the crucible, although the meniscus became more convex in reduced gravity. In the wetting case the aluminum did not climb up the corners in 1g, and one large symmetric void resulted at the top when the aluminum had solidified. In the wetting case during reduced gravity the molten aluminum was drawn up the wetted wall and partially across the lid by a capillary underpressure; however, on the nonwetting wall the aluminum moved down. One void resulted along the nonwetting side of the container continuing to the top on the same side.

14. SUBJECT TERMS

Voids; Reduced gravity; Aluminum; Real time x-ray system; Solidification; Space power

15. NUMBER OF PAGES

78

16. PRICE CODE

A05

17. SECURITY CLASSIFICATION OF REPORT	18. SECURITY CLASSIFICATION OF THIS PAGE	19. SECURITY CLASSIFICATION OF ABSTRACT	20. LIMITATION OF ABSTRACT
Unclassified	Unclassified	Unclassified	

National Aeronautics and
Space Administration

Lewis Research Center
Cleveland, OH 44135-3191